

AD-A255 004



ATION PAGE

Form Approved  
OMB No. 0704-0188

(2)

On average, 1 hour per response, including the time for reviewing instructions, searching existing data sources, gathering the collection of information. Send comments regarding this burden estimate or any other aspect of this form to Washington Headquarters Services, Directorate for Information Operations and Reports, 1215 Jefferson Avenue, Washington, DC 20540, and to the Office of Management and Budget, Paperwork Reduction Project (0704-0188), Washington, DC 20503.

1. AGENCY USE ONLY (Leave blank)		2. REPORT DATE 7/16/92	3. REPORT TYPE AND DATES COVERED Final Report (8/1/89-8/31/92)	
4. TITLE AND SUBTITLE Air Force Engineering Research Initiation Grants			5. FUNDING NUMBERS AFOSR-89-0464 2302/C1	
6. AUTHOR(S) Charles E. Freeman				
7. PERFORMING ORGANIZATION NAME(S) AND ADDRESS(ES) Engineering Foundation 345 E 47th St New York, NY 10017			8. PERFORMING ORGANIZATION REPORT NUMBER AFOSR-TR-2-0464	
9. SPONSORING/MONITORING AGENCY NAME(S) AND ADDRESS(ES) AFOSR/NA Bolling AFB, DC 20332-6448			10. SPONSORING/MONITORING AGENCY REPORT NUMBER AFOSR/NA 89-0464	
11. SUPPLEMENTARY NOTES		DISTRIBUTION STATEMENT A Approved for public release Distribution Unlimited		
12a. DISTRIBUTION/AVAILABILITY STATEMENT Approved for public release. distribution is unlimited			12b. DISTRIBUTION CODE	
13. ABSTRACT (Maximum 200 words)  WORK UNIT This <del>grant</del> covers the Air Force Research Initiation Grant (AFERIG) Program for the Academic Year 1990-1991. It was announced in the Fall of 1990 for up to 25 AFERIGs carrying a stipend of \$20,000. The Engineering Foundation's five Founder Societies received a total of 262 proposals. Fifty-six of these were selected for referral to AFOSR. AFOSR selected 25 with 10 alternates. <i>this report contains abstracts and papers for each of the 25 grants.</i>  <div style="text-align: right;">           92-22651              395591 13089         </div>				
14. SUBJECT TERMS Engineering Research, "Young Investigators"			15. NUMBER OF PAGES 127	
			16. PRICE CODE	
17. SECURITY CLASSIFICATION OF REPORT Unclassified	18. SECURITY CLASSIFICATION OF THIS PAGE Unclassified	19. SECURITY CLASSIFICATION OF ABSTRACT Unclassified	20. LIMITATION OF ABSTRACT unlimited	

FINAL TECHNICAL REPORT - Grant No. AFOSR-89-0464  
Rev.1

AIR FORCE ENGINEERING RESEARCH INITIATION GRANTS (1990-1991)

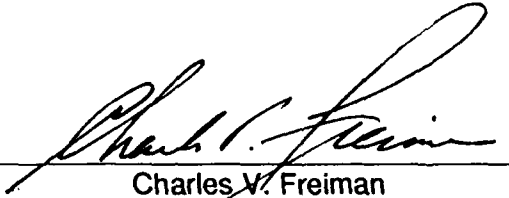
Submitted by:

Engineering Foundation  
United Engineering Trustees, Inc.  
345 East 47th Street  
New York, NY 10017

Submitted to:

Air Force Office of Scientific Research  
Bolling Air Force Base  
Washington, DC 20332-6448

ATTN: Lt. C. Gorton



Charles V. Freiman  
Director, Engineering Foundation

Submittal Date:

July 15, 1992

## CONTENTS

SECTION 1: SUMMARY	1
SECTION 2: 1990-1991 AWARDS	2-4
SECTION 3: ABSTRACTS OF MATERIALS SUBMITTED BY PRINCIPAL INVESTIGATORS FOR THE FINAL TECHNICAL REPORT	5-127

DTIC QUALITY INSPECTED 8

**BEST  
AVAILABLE COPY**

Accession For	
NTIS GRA&I	<input checked="checked" type="checkbox"/>
DTIC TAB	<input type="checkbox"/>
Unannounced	<input type="checkbox"/>
Justification	
By	
Distribution/	
Availability Codes	
Dist	Avail and/or Special
A-1	

## SECTION 1 - SUMMARY

This grant covers the Air Force Research Initiation Grant (AFERIG) Program for the Academic Year 1990-1991. It was announced in the Fall of 1990 for up to 25 AFERIGs carrying a stipend of \$20,000. The Engineering Foundation's five Founder Societies received a total of 262 proposals. Fifty-six of these were selected for referral to AFOSR. AFOSR selected 25 with 10 alternates. Eight of the 25 also received various NSF grants and were replaced by alternates. The final list of awardees is found in Section 2. All awardees have submitted reports for this final technical report. Abstracts of these studies are included in Section 3.

SECTION 2 - 1990-1991 AWARDS

- RI-B-90-01 "Ultrasonic-Based Measurement of Residual Stress Induced by Large Deformation Processes"  
Professor Jahan Rasty  
Department of Mechanical Engineering  
Texas Tech University
- RI-B-90-02 "The Effects of Grain Size on Cyclic Deformation and Fatigue Damage Accumulation"  
Professor David J. Morrison  
Department of Mechanical and Aeronautical Engineering  
Clarkson University
- RI-B-90-03 "Phase Transformations and Microstructure Development in Two-Phase TiAl + Ti3Al Intermetallic Alloys"  
Professor Vijay Vasudevan  
Department of Materials Science and Engineering  
University of Cincinnati
- RI-B-90-04 "Elimination of Abnormally Large Grains in Hot-Worked Billets of High-Temperature Nickel-Base Alloys"  
Professor Steven W. Thompson  
Department of Metallurgical and Materials Engineering  
Colorado School of Mines
- RI-B-90-05 "Experimental Investigation of Attenuation Characteristics of Subsurface Materials"  
Professor Young Jin Mok  
Department of Civil Engineering  
Kansas State University
- RI-B-90-06 "Quantitative Stereology of Concrete Microcracking"  
Professor Kim D. Basham  
Department of Civil and Architectural Engineering  
University of Wyoming
- RI-B-90-07 "Compression Strength of Composite Laminates"  
Professor Dimitris Lagoudas  
Department of Civil Engineering  
Rennselaer Polytechnic Institute
- RI-B-90-08 "Friction Mechanism of Granular Material Along an Interface"  
Professor Samuel G. Paikowsky  
Department of Civil Engineering  
University of Lowell
- RI-B-90-09 "A System for the Measurement of a Component Concentration in Two-Phase (Air-Water) Flows in Rectangular Channels"  
Professor Jerzy K. Keska  
Department of Mechanical Engineering  
University of Nebraska-Lincoln

- RI-B-90-10 "Effects of Reinforcement Geometry on Inelastic Deformation in Metal-Matrix Composites"  
Professor David G. Taggart  
Department of Mechanical and Applied Mechanics  
The University of Rhode Island
- RI-B-90-11 "Wake-Body Interactions and the Formation of Vortex Shedding Behind Bluff Bodies"  
Professor Paul J. Strykowski  
Department of Mechanical Engineering  
University of Minnesota
- RI-B-90-12 "Investigation of Mechanical Response During Phase Transitions in Polymers"  
Professor Mehrdad Negahban  
Department of Engineering Mechanics  
University of Nebraska-Lincoln
- RI-B-90-13 "In-Situ Fatigue Experiments in the High-Voltage Transmission Electron Microscope"  
Professor M. E. Kassner  
Department of Mechanical Engineering  
Oregon State University
- RI-B-90-14 "The Structure of Wakes Behind Various Bluff and Non-bluff Bodies"  
Professor Barsam Marasli  
Department of Mechanical Engineering  
The University of Maryland
- RI-B-90-15 "Experimental Determination of Multiple Nonlinear Kinematic Hardening Rules for Cyclic Viscoplasticity Models"  
Professor John Moosbrugger  
Department of Mechanical and Industrial Engineering  
Clarkson University
- RI-B-90-16 "Optimization of the Manufacturing Process of a Titanium Aluminide Metal Matrix Composite Using a Viscoplastic Constitutive Theory"  
Professor James A. Sherwood  
Department of Mechanical Engineering and Physical Sciences  
University of New Hampshire
- RI-B-90-17 "Stress Corrosion Cracking of a Superplastic Aluminum-Lithium Alloy"  
Professor M. N. Srinivasan  
Department of Mechanical Engineering  
Texas A&M University
- RI-B-90-18 "Effect of Fiber-Matrix Interface Conditions on the Effective Properties of Fiber Reinforced Composites"  
Professor Gregory Gillette  
Department of Civil Engineering  
The Catholic University of America
- RI-B-90-19 "Novel Microstrip Antenna Configurations for Enhanced Performance"  
Professor James T. Aberle  
Department of Electrical Engineering  
Arizona State University

- RI-B-90-20 "Simulation of Amorphous Silicon Hydride Devices"  
Professor Finley R. Shapiro  
Department of Electrical and Computer Engineering  
Drexel University
- RI-B-90-21 "Continuous-Time Adaptive Signal Processing Techniques"  
Professor Frank Cornett  
Department of Electrical Engineering  
Tennessee Technological University
- RI-B-90-22 "A Distributed Algorithm for Fault Simulation of Digital Designs  
Based on Circuit Partitioning"  
Professor Sumit Ghosh  
Division of Engineering  
Brown University
- RI-B-90-23 "Parallel Processing for Computer Vision Systems"  
Professor Alok N. Choudhary  
Department of Electrical and Computer Engineering  
Syracuse University
- RI-B-90-24 "Critical Analysis of Partially Open Cylindrical Reflector Antennas"  
Professor Atef Elsherbeni  
Department of Electrical Engineering  
University of Mississippi
- RI-B-90-25 "Search-Free Acquisition of Pseudonoise Codes"  
Professor Kurt Kosbar  
Department of Electrical Engineering  
University of Missouri-Rolla

**SECTION 3 - ABSTRACTS OF MATERIALS SUBMITTED BY PRINCIPAL INVESTIGATORS  
FOR THE FINAL TECHNICAL REPORT.**



RI-B-90-01

**Ultrasonic-Based Measurement of Residual Stress Induced by Large  
Deformation Processes**

Professor Jahan Rasty  
Department of Mechanical Engineering  
Texas Tech University

## ABSTRACT

Evaluation of the residual stress in a material is one of the fundamental tasks of a mechanical engineer. Conventional methods of stress determination include hole drilling, sectioning, and X-ray scanning. A major drawback of these methods is that they are either destructive or restricted to surface measurement only. Efficient utilization of high-tech alloys in complex metal forming processes requires development of simple techniques for determining the state of residual stress. The application of ultrasonic waves to material testing and characterization is a promising approach that does not have the aforementioned drawbacks. Specifically, ultrasonic technique has the advantage of being nonhazardous, nondestructive, versatile, and applicable to through thickness measurements.

The objective of this research was to further develop the acoustoelasticity theory for the application to the residual stress analysis. In the first phase of this work, a comprehensive literature search was conducted to determine the state of technology in this field. Although a considerable amount of research has been done in this area, most of it was scattered. This research presented a unified treatment of the acoustoelasticity theory for application to residual stress analysis. Furthermore, a modification to the small plastic deformation theory was proposed for application to large plastic deformation as encountered in manufacturing processes. An ultrasonic experimental setup was developed for residual stress analysis utilizing the pulse-echo-overlap technique. Further experiments were outlined for determining the validity of the proposed theory.

RI-B-90-02

**The Effects of Grain Size on Cyclic Deformation and Fatigue  
Damage Accumulation**

Professor David J. Morrison  
Department of Mechanical and Aeronautical Engineering  
Clarkson University

## *Executive Summary*

This report describes work accomplished during a one year Air Force Engineering Foundation Grant, RI-B-90-02, to study the effects of grain size on cyclic deformation and fatigue damage accumulation. Significant results have been obtained in the project. Accomplishments include the development of a computer program that automatically calculates key parameters describing cyclic stress-strain behavior and fundamental mechanisms of cyclic plasticity, a correlation between hysteresis loop shape behavior and the evolution of surface fatigue damage, image analysis experiments of surface damage evolution, crystallographic texture experiments, and a correlation between strain localization phenomena and fatigue crack initiation.

The results of the studies indicate that cyclic strain localization phenomena can be accurately measured by evaluating subtle changes in the shapes of the cyclic stress-strain hysteresis loops. Cyclic strain localization was found to be much more pronounced at low plastic strain amplitudes where persistent slip bands (psbs) form. Furthermore, the strain localization is more pronounced as the grain size of the material increases. These observations of strain localization phenomena have significant engineering significance. Specifically, at low plastic strain amplitudes, an increase in grain size has a detrimental effect on fatigue life. At high plastic strain amplitudes, where plastic strain is not localized, grain size has very little effect on fatigue life. These research findings have resulted in one journal publication and another manuscript in preparation for publication. A reprint of the journal article has been included in Appendix III.

RI-B-90-03

**Phase Transformations and Microstructure Development in Two-Phase  
TiAl + Ti3Al Intermetallic Alloys**

Professor Vijay Vasudevan  
Department of Materials Science and Engineering  
University of Cincinnati

# COMPOSITION DEPENDENCE OF THE MASSIVE TRANSFORMATION FROM $\alpha$ TO $\gamma$ IN QUENCHED TiAl ALLOYS

Ping Wang and Vijay K. Vasudevan

Dept. of Materials Science and Engineering, University of Cincinnati, ML 12, Cincinnati, OH 45221

(Received May 5, 1992)

## Introduction

Alloys based on the intermetallic compound TiAl have been of much interest in recent years as lightweight, structural materials for elevated temperature aerospace applications (1). The most promising alloys are based on the Ti-48 Al composition (compositions in the text refer to at.%) with ternary or quaternary additions and with the two-phase Ti<sub>3</sub>Al+TiAl ( $\alpha_2$ + $\gamma$ ) lamellar microstructure (2-5). Several studies concerned with phase equilibria and transformations in Ti- $\geq$ 40 Al alloys have been reported (6-10). In low Al alloys, the lamellar structure has been suggested to be produced by the reaction  $\alpha \rightarrow \alpha_2 \rightarrow \alpha_2 + \gamma$ , involving initial formation of stacking faults (11). More recently, it has been suggested that this mechanism is operative till ~42 Al, whereas at higher concentrations the  $\gamma$  lamellae are formed directly from the  $\alpha$  and subsequently the  $\alpha$  orders to  $\alpha_2$  to produce the same morphology of lamellae as observed at lower concentrations (4,12). Very recently, in two studies it has been shown that cooling rate has a major effect on the transformation of the  $\alpha$  phase. In the first, alloys containing 47-48 Al were studied (13), and it was observed that the  $\gamma$  forms from the  $\alpha$  in three morphologies depending on cooling rate. At low cooling rates, the lamellar morphology prevails, at intermediate rates a Widmanstätten morphology appears and at very high cooling rates a massive transformation dominates. The occurrence of the latter in a quenched Ti-48 Al alloy has also been confirmed very recently (12). In the second, where a Ti-48Al-2Mn-2Nb alloy was studied (14), very similar effects of cooling rate on the microstructure were reported, and the occurrence of the massive reaction at high cooling rates was confirmed (15). The purpose of this paper is to report on the composition dependence of transformations in Ti-(43-50) Al alloys water quenched from the fully  $\alpha$  region. In particular, evidence for a massive transformation from  $\alpha$  to  $\gamma$  in alloys with 46.54 to 50 Al is presented.

## Experimental

The compositions of the alloys studied are shown in Table 1. The Ti-43, 46 and 50 Al alloys were prepared by arc-melting commercial purity Ti and 99.999% pure Al. The 48 Al alloy was obtained as ingots in the cast+HIP (1200°C, 2h, 105 MPa) condition from commercial sources. The 43, 46 and 50 Al alloys were homogenized at 1100°C for 50 h followed by slow cooling. Cut samples from the alloys were coated with a high temperature glass ceramic (Corning Glass 7913) for protection from the atmosphere and heated to the completely  $\alpha$  region, namely, 1325, 1360, 1400°C and 1435-1450°C for the 43, 46, 48 and 50 Al alloys, respectively. After holding for various times from 15 minutes to 1 h, the samples were cooled at different rates, namely, furnace cool (FC), air cool (AC), oil quench (OQ), water quench (WQ) and iced brine quench (IBQ). Analysis of the oxygen and nitrogen contents after these various heat treatments showed that any pick-up of oxygen and nitrogen was restricted to the outer surface of the samples, whereas the interiors were unaffected (Table 1 and ref. (13)). Analysis of the Al contents after heat treatment showed that a small loss, typically  $\leq$ 0.25 at.%, had occurred in the alloys.

TABLE 1

Chemical Compositions of Alloys Studied

Aimed Composition (at.%)	Actual Composition			
	Ti (at.%)	Al (at.%)	O (wt.%)	N (wt.%)
Ti-43Al	Bal	43.19	0.062	0.008
Ti-46Al	Bal	46.54	0.051	0.005
Ti-46Al HT*	Bal	46.36	0.052	0.005
Ti-48Al	Bal	47.86	0.049	0.006
Ti-48Al HT*	Bal	47.98	0.036	0.004
Ti-50Al	Bal	49.40	0.088	0.014

\*Post heat treatment analysis after removal of ~2mm of outer surface of sample

The microstructures of the alloys were observed optically and also in a JEOL JXA-840 scanning electron microscope (SEM) utilizing back scattered electrons (BSE) for obtaining atomic number contrast. Fully quantitative electron microprobe analysis of the compositions of phases was conducted in the same SEM. Thin foils for transmission electron microscopy (TEM) were prepared from the samples using conditions described previously (13). The foils were observed in a Philips CM20 TEM operated at 200 kV, utilizing bright field (BF), dark field (DF) and selected area diffraction (SAD) imaging modes.

## Results

In this paper, only the results of microstructures of WQ samples are reported. Thus, optical micrographs of samples of the various alloys WQ from the completely  $\alpha$  region are shown in the micrographs in Figs. 1a-d. The optical micrograph of the WQ Ti-43.19 Al alloy appears featureless, Fig. 1a, and TEM examination showed that the microstructure was composed fully of  $\alpha_2$  domains. A prominent feature seen in the micrograph of the Ti-46.54 Al alloy, Fig. 1b, is the presence of dark, deeply etched, patchy regions in a light, featureless matrix. These regions appear to have nucleated largely at the prior  $\alpha$  grain boundaries and then spread rapidly into the grains in a spheroidal and massive fashion. On occasion, these dark regions were also found within grains, at some distance from the grain boundaries. Closer inspection of the latter sometimes reveals the existence of a fine striated structure emanating from the grain boundaries and terminating at locations where the dark regions commence. The interface between the dark and light regions varies from smooth to jagged from one region to another. The exact nature of the interface, i.e., incoherent or semi-coherent, has not been determined yet. Examination of the 47.86 and 49.40 Al alloys, Figs. 1c-d, revealed that practically the entire microstructure of the samples was dominated by the dark, mottled regions seen in the 46.54 Al alloy. A feathery morphology was also present often. It should be noted, however, that at the higher Al contents, particularly 49.40 Al, it was difficult to suppress the formation of the "equilibrium" lamellar morphology, which was often present at the grain boundaries and impinging on the dark regions within the grains.

TEM observations establish that the light, featureless regions seen in the optical micrograph of the WQ 46.54 Al alloy consist of  $\alpha_2$  domains, Fig. 2a, whereas the dark regions are  $\gamma$ , as shown in Fig. 2b by the BF micrograph and inset [110]  $\gamma$  SAD pattern. TEM observations of the 47.86 and 49.40 Al alloys, revealed that practically the entire microstructure was dominated by  $\gamma$ , although a few, sparsely distributed regions of lamellar  $\alpha_2 + \gamma$  were observed. An example is shown in Fig. 3 for the 47.86 Al alloy. The massive  $\gamma$  phase in all of these WQ alloys, especially the 46.54 Al, is typically characterized by a complex substructure consisting of antiphase boundaries (APB's), stacking faults, microtwins and dislocations (Figs. 2b and 3). The presence of APB's might suggest the occurrence of an intermediate disordered f.c.c. or f.c.t. structure prior to the formation of  $\gamma$ . Electron diffraction analysis of many  $\gamma$  grains showed the occurrence of all six variants. Aside from f.c.c.-twin related variants, numerous contacting variants in perpendicular twin relation, i.e., mutually perpendicular c-axes, are observed. These observations suggest that a direct transformation from  $\alpha$  to  $\gamma$  had occurred, perhaps in a massive fashion.

BSE images of the WQ 46.54 Al sample (Fig. 4a) are similar to those reported previously in the 47.20 Al alloy (13) and show regions of both darker contrast corresponding to  $\gamma$  and slightly lighter contrast corresponding to  $\alpha_2$ . Although the observation of contrast differences between the two phases indicates a difference in chemical composition, a microprobe scan analysis of the  $\alpha_2$  and  $\gamma$  regions extending through the interface, over a distance of  $\sim 600 \mu\text{m}$  at  $\sim 10 \mu\text{m}$  intervals, Fig. 4b, reveals that the compositions of the two phases are practically identical. Furthermore, no consistent trend in the compositions of the two phases is seen that might explain the differences in contrast seen in the BSE images. The possible reasons for the origin of the contrast differences have been discussed elsewhere (13). Observations of the 47.86 Al, and 49.40 Al alloys using BSE imaging did not reveal any contrast, i.e., were uniformly dark and no interfaces (between any  $\alpha_2$  and  $\gamma$ ) could be discerned. Microprobe scan analysis of these, Figs. 5a-b, respectively, shows that the compositions are practically invariant and near that of the bulk alloy compositions. These observations, together with the TEM results, provide strong evidence for a massive transformation from  $\alpha$  to  $\gamma$  at high cooling rates.

## Discussion

As mentioned earlier, in a previous study (13) the effect of cooling rate (and therefore, undercooling) on the transformation from  $\alpha$  to  $\gamma$  in a cast and homogenized Ti-47.20 Al alloy and a cast and extruded Ti-47.86 Al alloy were reported. In that study it was found that at low cooling rates the  $\gamma$  phase forms in a lamellar morphology, at intermediate rates a Widmanstätten morphology appears and at very high rates a massive morphology is prevalent. In the present study, the effect of Al content in binary alloys has been examined and the results show that the massive reaction from  $\alpha$  to  $\gamma$  occurs at high cooling rates from 46.54 to 50 Al. The massive transformation has been extensively studied in the past and examples of this transformation can be found in many systems (16-19). Essentially, a massive transformation takes place by diffusional nucleation and growth and involves a change in crystal structure without a change in composition, and in principle, can be observed in any system where the pertinent phase fields overlap in composition (16,17). Moreover, it is possible for a massive reaction to be considered as occurring in the metastable two-phase field, such as that below a invariant reaction temperature (eg., eutectoid temperature) (17). Both the TEM observations showing the structural change and the microprobe analysis establishing composition invariance attest to the occurrence of the massive reaction from  $\alpha$  to  $\gamma$  at high cooling rates. The nucleation of the massive  $\gamma$  is seen to occur mostly at the grain boundaries

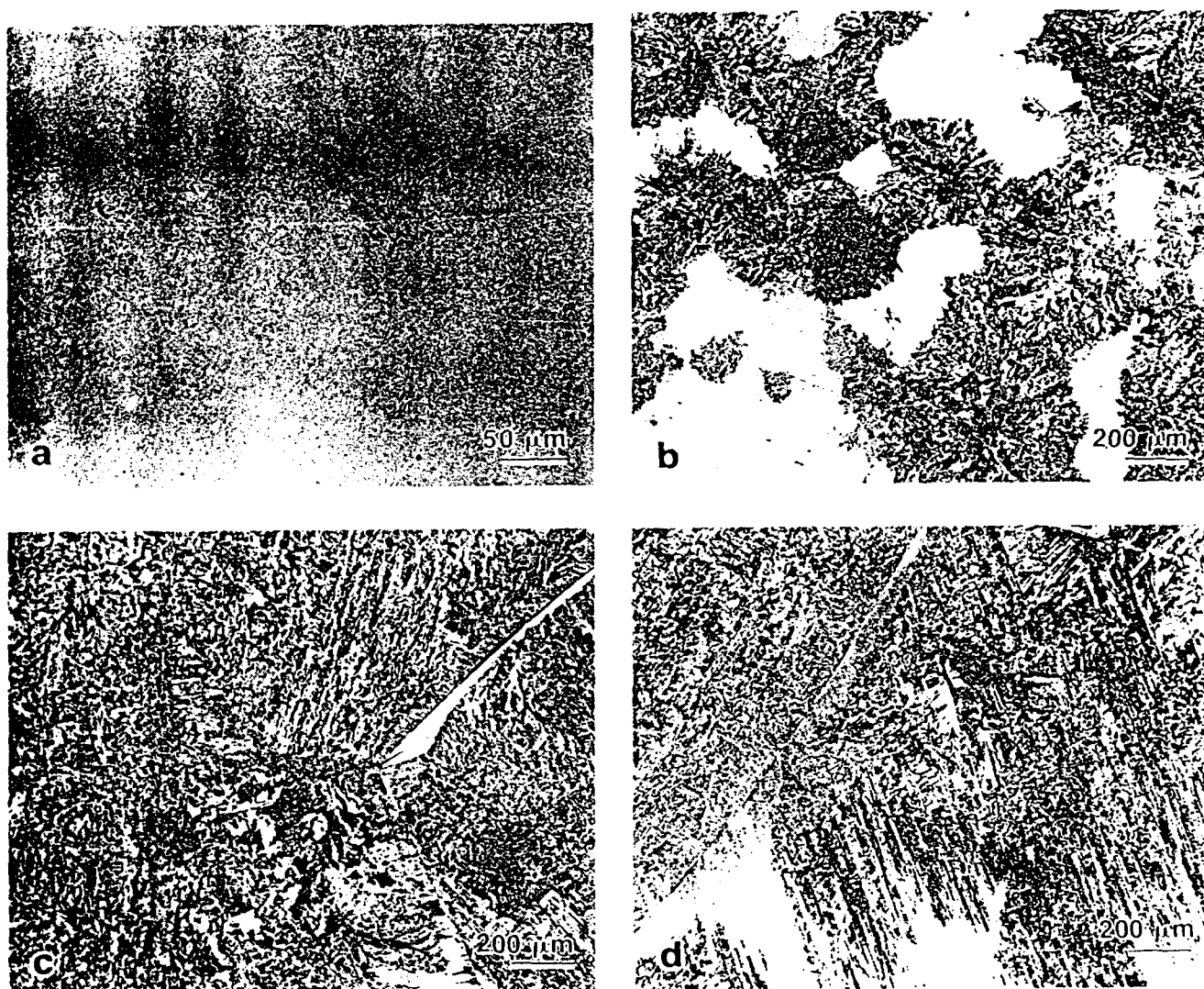


FIG. 1. Optical microstructures of TiAl alloys WQ from the fully  $\alpha$  region: (a) Ti-43.19 Al, (b) Ti-46.54 Al, (c) Ti-47.86 Al, and (d) Ti-49.40 Al.

of the prior  $\alpha$ , as is seen usually in most massive reactions (16–19). Furthermore, the present observations of the massive reaction for Al contents from 50 to 46.54 Al indicates that significant penetration into the equilibrium  $\alpha/\gamma$  or metastable equilibrium  $\alpha/\gamma$  region occurs. However, although all results have not been presented herein, alloys containing 43–45 Al WQ from the  $\alpha$  region transformed completely to  $\alpha_2$  and showed no evidence of the massive transformation.

In order to explain the observed composition dependence of the massive reaction, accurate knowledge of equilibrium and metastable equilibrium phase boundaries and temperature of nucleation of the massive  $\gamma$  are required. Thus, the relevant portion of currently accepted Ti–Al phase diagram from the work of McCullough et al. (9), modified slightly by Jones and Kaufmann (12), is shown in Fig. 6. The estimated positions of the metastable  $\alpha/\alpha_2$ ,  $\gamma/\alpha_2$ ,  $\alpha/\alpha_2$  phase boundaries and the  $\alpha/\gamma$  and  $\alpha/\alpha_2$   $T_m$  lines are also shown. It can be seen that for alloy Al contents approximately >49 at %, the compositions of the  $\alpha$  and  $\gamma$  phases overlap above the eutectoid temperature (1128 °C), whereas at lower concentrations the overlap occurs below the eutectoid temperature in the metastable  $\alpha/\gamma$  phase field. It is generally believed that the  $T_m$  line represents the limit for the massive reaction and the distance between the  $T_m$  line and the temperature of start of the reaction represents the undercooling and therefore the driving force for the massive transformation (16,17). Hillert (20) has, however, argued that the massive transformation requires undercooling below the  $T_m$  line to reach the  $\gamma$  phase or metastable equilibrium  $\gamma$  phase, and that the  $T_m$  line can be an upper limit only. The latter boundary, the  $\alpha/\alpha_2$  boundary, will be encountered particularly for compositions less than about 45 Al, and cause the transformation from  $\alpha$  to  $\alpha_2$  directly rather than from  $\alpha$  to  $\gamma$ . Following this line of reasoning, and



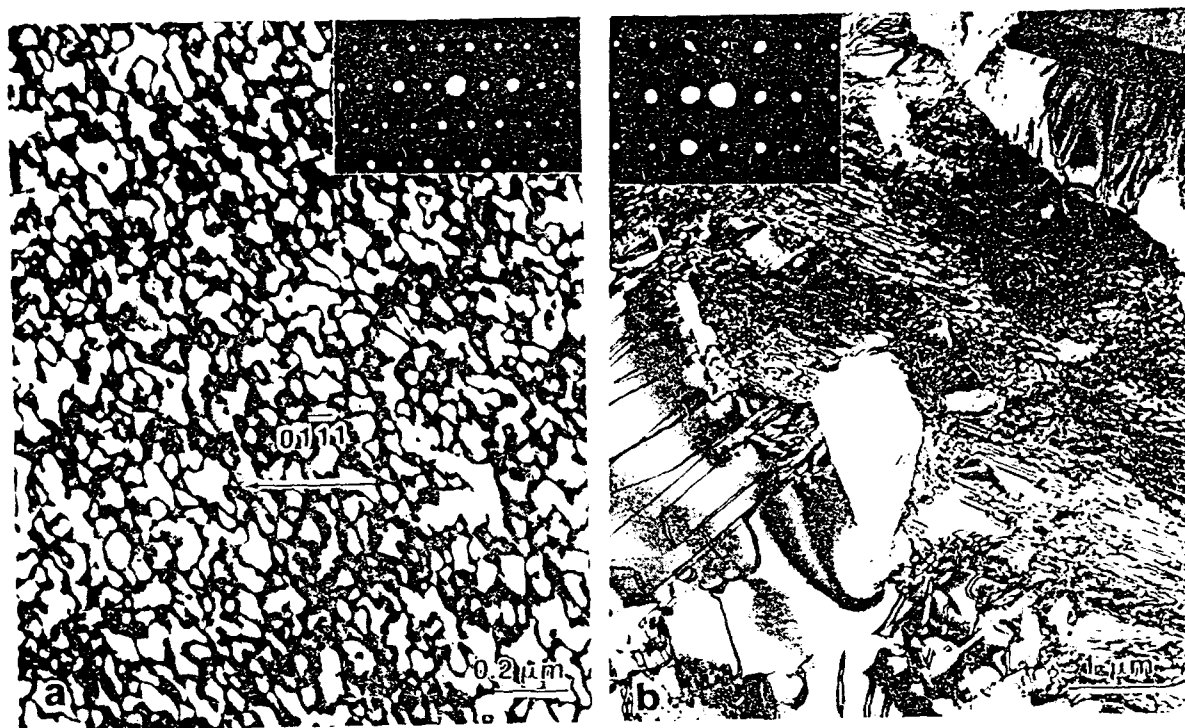


FIG. 2. TEM micrographs of Ti-46.54 Al alloy WQ after holding for 40 minutes at 1360°C. (a) DF micrograph and inset [1213] SAD pattern of light regions in Fig. 1b showing  $\alpha_2$ ; (b) BF micrograph and inset [110] SAD pattern of dark regions in Fig. 1b showing massive  $\gamma$ .

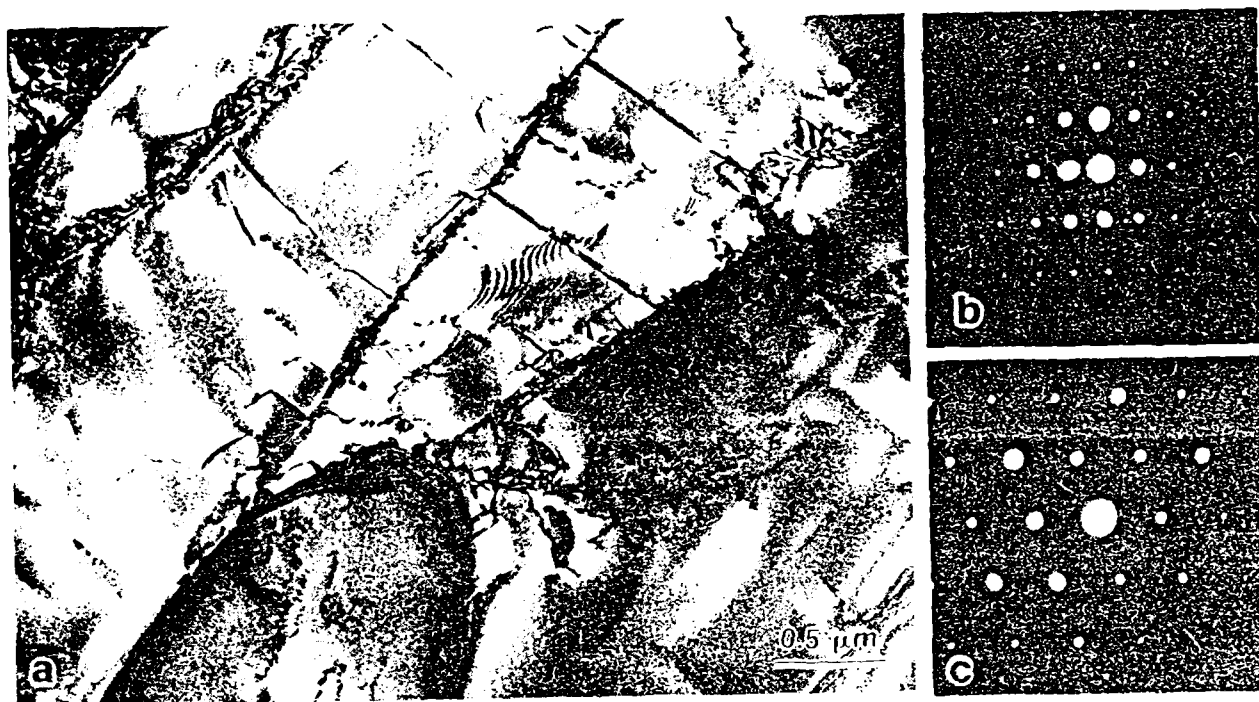


FIG. 3. (a) BF-TEM micrograph, (b) [110], and (c) [101] SAD patterns showing massively transformed  $\gamma$  in the Ti-47.86 Al alloy WQ from 1400°C after holding for 0.5 hour.

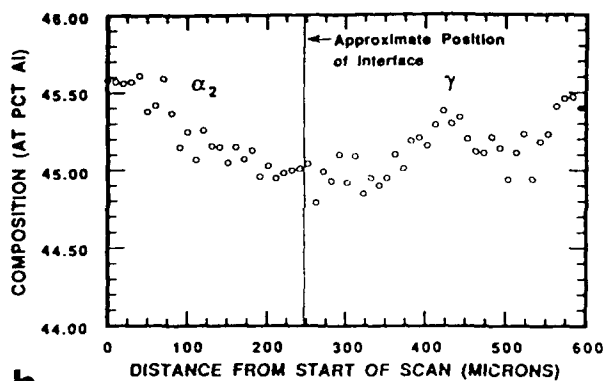
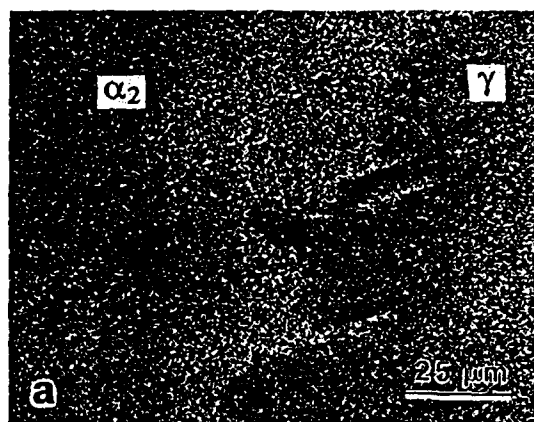


FIG. 4. (a) BSE micrograph and (b) microprobe scan analysis of Ti-46.54 Al alloy WQ from the fully  $\alpha$  region.

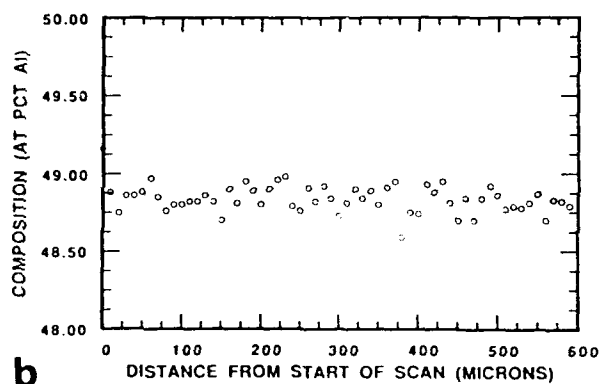
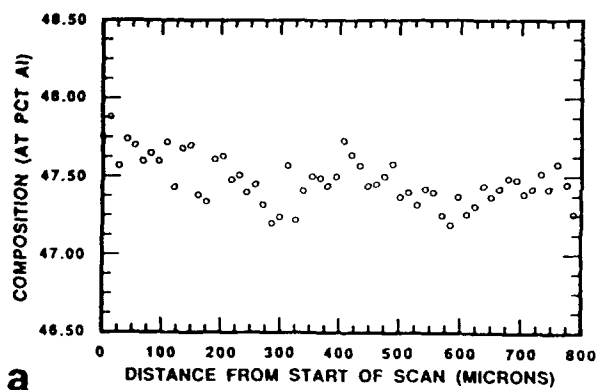


FIG. 5. Microprobe scan analysis of (a) Ti-47.86Al and (b) Ti-49.40 alloys WQ from the fully  $\alpha$  region.

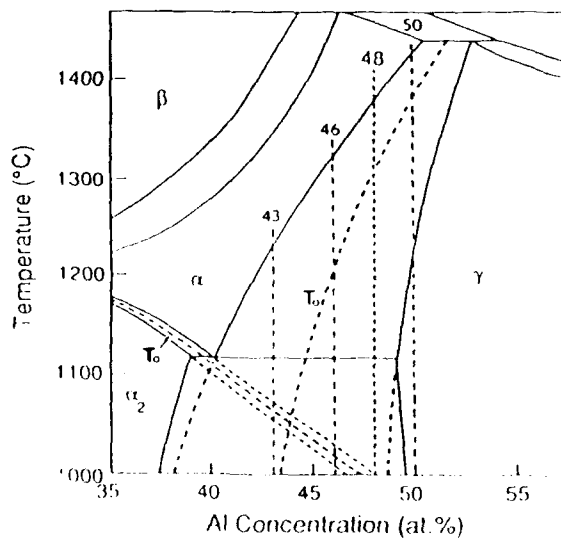


FIG. 6. Partial phase diagram of the Ti-Al system (from ref. (12)).

assuming for the sake of simplicity that the  $\alpha$  to  $\alpha_2$  transformation temperature does not change markedly with cooling rate, the temperature range,  $\Delta T$ , available for nucleation and growth of the massive reaction from  $\alpha$  to  $\gamma$  can be estimated from the difference between  $T_0 \alpha/\gamma$  and  $T_0 \alpha/\alpha_2$ . Thus, the values of  $\Delta T$ , which increase rapidly with Al content, are estimated to be approximately 125, 200, 265 and 335°C for the 45, 46, 47 and 48 Al alloys, respectively. For compositions below ~44 Al, the  $\alpha/\alpha_2$  boundary is encountered prior to the  $\alpha/\gamma T_0$  line and so rapid quenching results only in the formation of  $\alpha_2$ . The absence of the massive reaction between 46 and ~44 Al is most likely related to either the difficulty in nucleating  $\gamma$  at these compositions or that the available  $\Delta T$  does not provide an adequate driving force for its nucleation (before the  $\alpha$  to  $\alpha_2$  transformation intervenes).

Another interesting aspect seen is that the microstructures of the 46.54 and 47.20 Al (13) alloys consists of  $\alpha_2$  and massive  $\gamma$ , i.e., the massive transformation does not appear to proceed to completion. In comparison the 47.86 Al alloy initially in the cast + HIP condition (present study) as well as in the extruded condition (13) appears to transform almost completely to massive  $\gamma$ . It was thought in the previous study that this difference in behavior maybe due to a grain size effect, i.e., the 47.20 Al alloy had a prior grain size >500  $\mu\text{m}$  compared with 40 to 100  $\mu\text{m}$  in the extruded 47.86 Al alloy and as a consequence there were fewer sites for nucleation of the massive  $\gamma$ . Once nucleated these grow until the  $\alpha/\alpha_2$  boundary is encountered below 1125°C and the  $\alpha \rightarrow \alpha_2$  transformation intervenes and arrests further progression of the massive reaction. For the reasons discussed in the preceding paragraph, it is clear that the difference in alloy compositions could also be responsible for this effect, i.e., the available  $\Delta T$  (and therefore time) for nucleation and growth of the massive reaction before the intervention of the  $\alpha$  to  $\alpha_2$  transformation decreases markedly with a decrease in the Al content. The relative contributions of these two effects needs investigation. Finally, it is clear that before the temperature dependence of the massive reaction can be ascertained positively, experimental determination of the temperature of start of the reaction is required. These aspects, together with the nature of the parent-massive interface, orientation relationships, and the nucleation and growth mechanisms of the different morphologies of  $\gamma$  are the subject of ongoing research.

### Conclusions

In summary, the microstructures of Ti-(43-50) Al alloys water quenched from the fully  $\alpha$  phase region have been studied. In particular, evidence for the occurrence of a massive reaction from  $\alpha$  to  $\gamma$  in alloys with Al contents in the range of 46.54 to 50 at.% has been presented and rationalized in terms of phase diagram considerations.

### Acknowledgements

Support for this research from the Engineering Foundation, the Alcoa Foundation and the State of Ohio Edison Materials Technology Center is deeply appreciated. The authors are thankful to the Air Force Materials Laboratory, WPAFB, Dayton for use of the SEM facilities and to Mr. Cameron Begg for his help with the SEM/microprobe work.

### References

1. H. A. Lipsitt, Mat. Res. Soc. Symp. Proc., **39**, 351 (1985).
2. M. J. Blackburn and M. P. Smith, United States Patent, No. 4,294,615 (1981).
3. S. C. Huang and E. L. Hall, Mat. Res. Soc. Symp. Proc., **133**, 373 (1989).
4. Y. W. Kim, Mat. Res. Soc. Symp. Proc., **213**, 777 (1991).
5. D. S. Shih, S. C. Huang, G. K. Scarr, H. Jang and J. C. Chesnutt: In: Microstructure/ Property Relations in Titanium Alloys and Titanium Aluminides, Y. W. Kim and R. R. Boyer (eds.), p. 135, TMS-AIME, Warrendale, PA (1991).
6. S. A. Jones, R. D. Shull, A. J. McAlister and M. J. Kaufmann, Scripta Metall., **22**, 1235 (1988).
7. J. J. Valencia, C. McCullough, C. G. Levi and R. Mehrabian, Scripta Metall., **21**, 1341 (1987).
8. J. A. Graves, L. A. Bendersky, F. S. Biancaneello, J. H. Perepezko and W. J. Boettinger, Mater. Sci. Engr., **98**, 265 (1988).
9. C. McCullough, J. J. Valencia, C. G. Levi and R. Mehrabian, Acta Metall., **37**, 1321 (1989).
10. E. L. Hall and S. C. Huang, Acta Metall., **38**, 539 (1990).
11. M. J. Blackburn, In: The Science, Technology and Application of Titanium Alloys, R. I. Jaffee and N. E. Promisel (eds.), **2**, p. 633, Plenum Press, NY (1970).
12. S. A. Jones and M. J. Kaufmann, Submitted to Acta Metall. et Mater. (1991).
13. P. Wang, G. B. Viswanathan and V. K. Vasudevan, Metall. Trans., **23A**, 790 (1992).
14. P. McQuay, D. M. Dimiduk, and S. L. Semiatin, Scripta Metall. et Mater., **25**, 1689 (1991).
15. P. McQuay and V. K. Vasudevan, University of Cincinnati, Cincinnati, OH, unpublished research (1991).
16. T. B. Massalski, In: Phase Transformations, p. 433, ASM, Metals Park, OH (1970).
17. J. H. Perepezko, Metall. Trans., **15A**, 437 (1984).
18. D. A. Karlyn, J. W. Cahn and M. Cohen, Trans. AIME, **245**, 197 (1969).
19. M. R. Plichta, H. I. Aaronson and J. H. Perepezko, Acta Metall., **26**, 1293 (1978).
20. M. Hillert, Metall. Trans., **15A**, 411 (1984).

## Observation of a Massive Transformation from $\alpha$ to $\gamma$ in Quenched Ti-48 At. Pct Al Alloys

PING WANG, G.B. VISWANATHAN,  
and VIJAY K. VASUDEVAN

Owing to their unique combination of attractive properties, such as lightness, superior strength, creep and oxidation resistance, alloys based on the intermetallic compound TiAl have been of much interest in recent years as structural materials for elevated temperature aerospace applications.<sup>[1]</sup> The alloys developed to date that show the most promise with regard to room-temperature ductility and elevated temperature strength are based on the Ti-48Al composition (compositions in the text refer to atomic percent), with additions of elements such as V, Cr, Nb, Mn, *etc.*, singly or in combination.<sup>[2-6]</sup> All of these alloys are two-phase, with a microstructure composed of either fully lamellar grains of Ti<sub>3</sub>Al + TiAl ( $\alpha_2$  +  $\gamma$ ) or duplex primary  $\gamma$  plus lamellar grains, depending on processing and heat treatment.<sup>[4]</sup> The properties of these alloys are quite sensitive to microstructure and, therefore, to heat treatment; duplex structures show higher tensile ductilities, for example, up to 2.2 pct in binary Ti-48Al<sup>[3,4]</sup> and up to 4 pct in ternary or quaternary alloys,<sup>[2-6]</sup> whereas fully lamellar structures have poor ductility.<sup>[4-7]</sup>

The lamellar ( $\alpha_2$  +  $\gamma$ ) structure was first studied by Blackburn,<sup>[8]</sup> who reported the formation of alternate lamellae of  $\gamma$  and  $\alpha_2$  with an orientation relationship involving  $\{111\} \gamma // \{0001\} \alpha_2$  and  $\langle 011 \rangle \gamma // \langle \bar{1}\bar{1}20 \rangle \alpha_2$  and suggested that the  $\gamma$  may form by a stacking fault mechanism. More recently, several studies of phase equilibria and transformations in two-phase Ti<sub>3</sub>Al + TiAl alloys have appeared.<sup>[9-17]</sup> Of particular significance are the results of these investigations showing decidedly that the ( $\beta$  +  $\gamma$ ) two-phase field shown in previous Ti-Al phase diagrams<sup>[18]</sup> does not exist and, instead, the ( $\alpha$  +  $\gamma$ ) phase field extends up to the peritectic temperature; *i.e.*, the  $\alpha$  region exists up to 1450 °C and 50 at. pct Al. Recently,

---

PING WANG, G.B. VISWANATHAN, Graduate Research Assistants, and VIJAY K. VASUDEVAN, Assistant Professor, are with the Department of Materials Science and Engineering, University of Cincinnati, Cincinnati, OH 45221.

Manuscript submitted April 17, 1991

METALLURGICAL TRANSACTIONS A

data of Antony<sup>[5]</sup> to account for all of the observed interplanar spacings and hence the recharacterization of the silicide in that alloy.

The calculated interplanar spacings for the silicides  $S_1$ ,  $S_2$ , and  $S'$  are compared with the values determined experimentally (X-ray data of Antony<sup>[5]</sup>) in Table I. Now when the measured interplanar spacings for  $S'$  silicide<sup>[5]</sup> are compared with the calculated values, it may be noted that the experimentally observed interplanar spacing of 0.350 nm is considerably different from the corresponding calculated value of 0.335 nm. Further, the interplanar spacings 0.303 and 0.201 nm are not accounted for by either  $S'$  silicide or  $\alpha$ -titanium. However, it may be noted that the interplanar spacings 0.350, 0.303, and 0.201 nm, which do not agree for  $S'$ , are the typical interplanar spacings of the  $S_2$  silicide. Moreover, all of the other observed interplanar spacings, with the exception of 0.222, 0.171, 0.146, and 0.135 nm, are also in good agreement with those calculated for  $S_2$ . These interplanar spacings, however, match well with those of  $\alpha$ -titanium. Thus, it can be stated that  $S_2$  silicide definitely exists in that alloy.

It is important to mention here that Kotval and Calder<sup>[14]</sup> also have characterized silicides in the complex alloys Ti-5Al-5Sn-2Zr-0.8Mo-0.7Si and Ti-4.5Al-2Sn-2Zr-3Ga-2Mo-0.5Si as  $S'$ , using electron diffraction technique. Analysis of their selected area diffraction patterns reveals that the silicide in alloy Ti-4.5Al-2Sn-2Zr-3Ga-2Mo-0.5Si could be indexed either as  $S_1$  or  $S'$ . However, the electron diffraction pattern of the silicide in the alloy Ti-5Al-5Sn-2Zr-0.8Mo-0.7Si can be indexed only as  $S'$  silicide.

In conclusion, it may be stated that all of the interplanar spacings for the silicide in alloy Ti-6Al-3Sn-3Zr-0.5Si reported by Antony<sup>[5]</sup> are accounted for in terms of the typical  $S_2$  silicide and the matrix  $\alpha$ -titanium. However, in the context of the findings of Kotval and Calder,<sup>[14]</sup> detailed investigations using both X-ray as well as electron diffraction techniques are required to fully resolve the controversies.

## REFERENCES

1. S.R. Seagle and H.B. Bomberger: *The Science, Technology, and Application of Titanium*, R.I. Jaffee and N.E. Promiel, eds., Pergamon Press, New York, NY, 1970, pp. 1001-08.
2. M.R. Winstone, R.D. Rawlings, and D.R.F. West: *J. Less-Common Met.*, 1975, vol. 39, pp. 205-17.
3. A.T.K. Assadi, H.M. Flower, and D.R.F. West: *Met. Technol.*, 1979, Jan., pp. 16-23.
4. W. Cho, J.W. Jones, J.E. Allison, and W.T. Donlon: *6th World Conf. on Titanium*, Proc. Conf., Les Editions de Physique, Les Ulis Cedex, France, 1988, vol. 1, pp. 187-92.
5. K.C. Antony: *Trans. TMS-AIME*, 1968, vol. 242, pp. 1454-56.
6. H.M. Flower, P.R. Swann, and D.R.F. West: *Metall. Trans.*, 1971, vol. 2, pp. 3289-97.
7. F. Barbier, C. Servant, C. Quesne, and P. Lacombe: *J. Microsc. Spectrosc. Electron.*, 1981, vol. 6, pp. 299-301.
8. C. Ramachandra and V. Singh: *Metall. Trans. A*, 1982, vol. 13A, pp. 771-75.
9. C. Ramachandra and Vakil Singh: *J. Mater. Sci.*, 1988, vol. 23, pp. 835-41.
10. A.P. Woodfield, P.J. Postans, M.H. Loretto, and R.E. Smallman: *Acta Metall.*, 1988, vol. 36, pp. 507-15.

11. D. Banerjee, J.E. Allison, F.H. Froes, and J.C. Williams: *Titanium Sci. Tech.*, G. Lütjering, U. Zwicker, and W. Bunk, eds., Deutsche Gesell. Metallkunde, Oberursel, Federal Republic of Germany, 1985, vol. 3, pp. 1519-26.
12. C. Ramachandra: Ph.D. Thesis, Banaras Hindu University, Varanasi, India, 1985.
13. S. Ankem, D. Banerjee, D.J. McNeish, J.C. Williams, and S.R. Seagle: *Metall. Trans. A*, 1987, vol. 18A, pp. 2015-25.
14. P.S. Kotval and R.W. Calder: *Metall. Trans.*, 1972, vol. 3, pp. 1308-11.
15. T. Manoubi, C. Servant, and P. Lacombe: *J. Less-Common Met.*, 1980, vol. 69, pp. 219-36.

## Observation of a Massive Transformation from $\alpha$ to $\gamma$ in Quenched Ti-48 At. Pct Al Alloys

PING WANG, G.B. VISWANATHAN, and VIJAY K. VASUDEVAN

Owing to their unique combination of attractive properties, such as lightness, superior strength, creep and oxidation resistance, alloys based on the intermetallic compound TiAl have been of much interest in recent years as structural materials for elevated temperature aerospace applications.<sup>[1]</sup> The alloys developed to date that show the most promise with regard to room-temperature ductility and elevated temperature strength are based on the Ti-48Al composition (compositions in the text refer to atomic percent), with additions of elements such as V, Cr, Nb, Mn, etc., singly or in combination.<sup>[2-6]</sup> All of these alloys are two-phase, with a microstructure composed of either fully lamellar grains of  $Ti_3Al + TiAl$  ( $\alpha_2 + \gamma$ ) or duplex primary  $\gamma$  plus lamellar grains, depending on processing and heat treatment.<sup>[4]</sup> The properties of these alloys are quite sensitive to microstructure and, therefore, to heat treatment; duplex structures show higher tensile ductilities, for example, up to 2.2 pct in binary Ti-48Al<sup>[3,4]</sup> and up to 4 pct in ternary or quaternary alloys,<sup>[3-6]</sup> whereas fully lamellar structures have poor ductility.<sup>[4-7]</sup>

The lamellar ( $\alpha_2 + \gamma$ ) structure was first studied by Blackburn,<sup>[8]</sup> who reported the formation of alternate lamellae of  $\gamma$  and  $\alpha_2$  with an orientation relationship involving  $\{111\} \gamma // \{0001\} \alpha_2$  and  $\langle 0\bar{1}1 \rangle \gamma // \langle \bar{1}\bar{1}20 \rangle \alpha_2$  and suggested that the  $\gamma$  may form by a stacking fault mechanism. More recently, several studies of phase equilibria and transformations in two-phase  $Ti_3Al + TiAl$  alloys have appeared.<sup>[9-17]</sup> Of particular significance are the results of these investigations showing decidedly that the ( $\beta + \gamma$ ) two-phase field shown in previous Ti-Al phase diagrams<sup>[18]</sup> does not exist and, instead, the ( $\alpha + \gamma$ ) phase field extends up to the peritectic temperature; i.e., the  $\alpha$  region exists up to 1450 °C and 50 at. pct Al. Recently,

PING WANG, G.B. VISWANATHAN, Graduate Research Assistants, and VIJAY K. VASUDEVAN, Assistant Professor, are with the Department of Materials Science and Engineering, University of Cincinnati, Cincinnati, OH 45221.

Manuscript submitted April 17, 1991.

several investigators<sup>[19-22]</sup> have studied the lamellar structure and reported the observation of different types of orientation and twin variants and interfaces of TiAl. It has been suggested<sup>[14,17]</sup> that in alloys containing up to ~42Al, the lamellar structure is formed by the reaction  $\alpha \rightarrow \alpha_2 \rightarrow \alpha_2 + \gamma$ , whereas at higher concentrations, the  $\gamma$  lamellae are formed directly from the  $\alpha$  by possibly a stacking fault-like mechanism, and subsequently, the  $\alpha$  orders to  $\alpha_2$  to produce the same morphology of lamellae as observed at lower concentrations. It might be expected that the transformation of the  $\alpha$  phase would be sensitive to cooling rate. Other than studies on the effect of rapid solidification,<sup>[10-15]</sup> there have been limited studies of the effect of cooling rate on the transformation of the disordered  $\alpha$  phase in high-Al alloys. The purpose of this article is to report on such an investigation in a Ti-48Al alloy. In particular, the observation of a massive transformation from  $\alpha$  to  $\gamma$  is highlighted and documented for the first time.

A Ti-48Al alloy (#1) was prepared by arc melting commercial-purity Ti and 99.999 pct pure Al. The alloy button was homogenized at 1150 °C for 50 hours followed by slow cooling. A second Ti-48Al (#2) cast ingot was obtained from The Duriron Company, Inc., Dayton, OH, hot isostatically pressed at 1200 °C for 2 hours, sealed in a Ti-6Al-4V can under vacuum, and extruded at 1360 °C at a ratio of 6:1. The Al contents after homogenization in the two alloys were determined to be 47.20 and 47.86 at. pct, respectively. Caution was taken to minimize, as far as possible, the reaction of the samples during heat treatment with the atmosphere and the consequent ingestion of oxygen and nitrogen. Cut samples were placed in quartz capsules, evacuated to a pressure of  $10^{-6}$  torr repeatedly after back-filling with argon, and finally sealed under argon. In addition, Ti foils, placed separately inside the capsules well away from the samples, were heated to about 800 °C after encapsulation to getter any remnant oxygen and nitrogen in the back-filled argon. Another scheme for protection used consisted of coating the samples with a high-temperature glass-ceramic (CORNING\* Glass 7913) prior to direct placement in

\*CORNING is a trademark of Corning Glass Works, Corning, NY.

the furnace. Most of the results presented herein utilized the latter scheme. Protected samples were heated to the completely  $\alpha$  region, namely, 1400 °C, for various times ranging from 15 minutes to an hour and then cooled at various rates, namely, furnace cooled (FC), air cooled (AC), oil quenched (OQ), water quenched (WQ), and iced brine quenched (IBQ). Examination of the microstructures revealed no significant effects of the solutionizing time on the transformation modes. Finally, to address the issue of the possible effect of oxygen and nitrogen, some samples were solution treated in air for various times and cooled at various rates. The microstructures of these were essentially identical to those that received protection. The oxygen and nitrogen contents after these various treatments were analyzed and are presented later. Analysis of the Al contents after heat treatment indicated that a small loss, typically <0.25 at. pct, had occurred.

Optical microscopy observations were conducted on

samples mounted, polished, and etched with Kroll's reagent. The microstructures were also observed in a JEOL JXA-840 scanning electron microscope (SEM) utilizing back-scattered electrons for obtaining atomic number contrast. Fully quantitative electron microprobe analysis of the compositions of phases was conducted in the same SEM. Thin foils for transmission electron microscopy were prepared from the heat-treated samples by the twin-jet technique using a solution consisting of 300 ml methanol, 180 ml butyl alcohol, 20 ml perchloric acid, and 10 ml hydrochloric acid, at a voltage of ~70 V, current of 20 to 30 mA, and a temperature of ~-40 °C. Observations of the foils was conducted in a PHILIPS\* CM20

\*PHILIPS is a trademark of Philips Electronic Instruments Corporation, Mahwah, NJ.

transmission electron microscope (TEM) operated at 200 kV, utilizing bright-field (BF), dark-field (DF), and selected area diffraction (SAD) imaging modes.

The optical microstructures of samples of alloy 1 cooled at different rates from the completely  $\alpha$  region are shown in the micrographs in Figures 1(a) through (f). Aside from the characteristic fine lamellar structure,<sup>[14,13,17]</sup> another prominent feature present in the FC and particularly the AC micrographs (Figures 1(a) and (b)) is a structure that appears in a Widmanstätten morphology, in three to four orientations within a single grain. The AC sample also shows the presence of deeply etched, mottled regions. As shown later, both of these structures were established to be  $\gamma$ . A dramatic change in the microstructure is observed at the higher cooling rates. A remarkable feature seen in the micrographs of samples that were quenched in oil, water, and iced brine (Figures 1(c) through (e)) is the presence of dark, deeply etched, patchy regions in a featureless matrix. These regions appear to have nucleated largely at the prior  $\alpha$  grain boundaries and then spread rapidly into the grains in a spheroidal and massive fashion. Often these dark regions were also found within grains, at some distance from the grain boundaries (Figure 1(e)). The interface between the dark and light regions varies from smooth to jagged from one region to another and appears to be incoherent, although this has not been established positively. The volume fraction of the dark regions did not appear to change appreciably with an increase in cooling rate.

To ascertain whether the dark regions formed only upon quenching from the fully  $\alpha$  region, another sample was heated to 1400 °C, slowly cooled to 1360 °C, i.e., into the  $\alpha + \gamma$  region, and WQ. The micrograph corresponding to this treatment, shown in Figure 1(f), appears practically identical to those from samples quenched rapidly from above the  $\alpha$  transus. It should be noted, however, that a few  $\alpha + \gamma$  lamellae, primarily restricted to the grain boundaries, were formed during the initial cooling from 1400 °C, whereas the holding at 1360 °C prior to the quench did not produce any primary  $\gamma$  grains, so that the composition of the  $\alpha$ , for the most part, should have remained the same as the alloy composition. One possible reason for the absence of the primary  $\gamma$  grains is related to the fact that the nucleation of these is dependent on the prior grain size and holding time and both the large grain size of the as-cast + homogenized

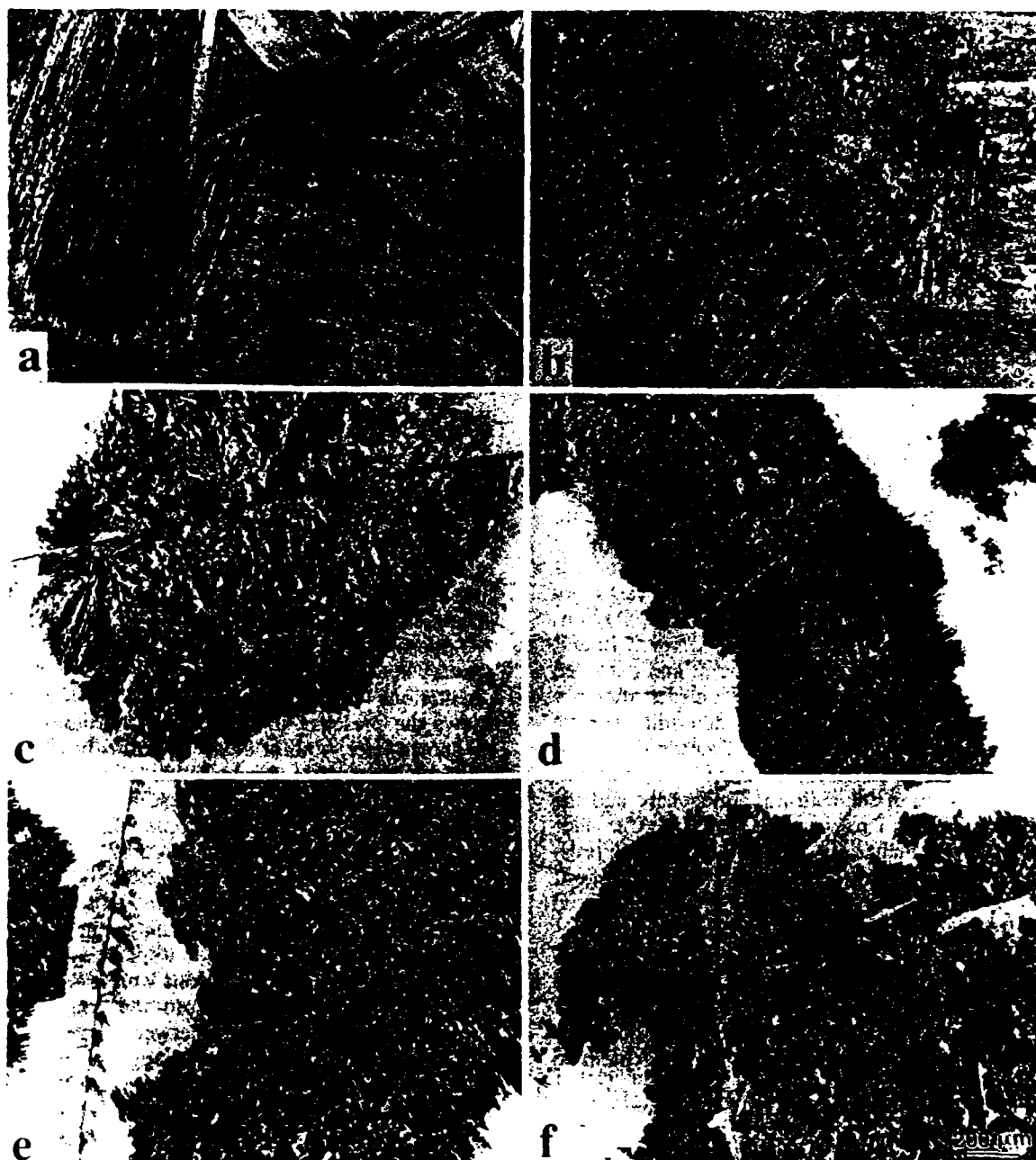


Fig. 1—Optical microstructures of Ti-47 2Al alloy held at 1400 °C for 1 h and cooled at various rates: (a) FC, (b) AC, (c) OQ, (d) WQ, (e) IBQ, and (f) slow cooled from 1400 °C to 1360 °C, held 15 min, followed by a water quench.

samples (500 through 1000  $\mu\text{m}$ ) and short time of 15 minutes diminished the opportunity for nucleation.

In order to further understand the microstructures, TEM observations of the samples cooled at the different rates were conducted. The light, featureless regions in the samples quenched at high cooling rates were established to be  $\alpha_2$ , as shown in the DF micrograph and inset diffraction pattern in Figure 2 taken from the WQ sample; the presence of antiphase domains, as well as, on occasion, stacking faults, can also be noted. The dark regions in the high cooling rate samples were determined to be  $\gamma$ . An example is shown in Figure 3 by the BF

micrograph and SAD patterns corresponding to several  $\gamma$  zone axes, taken from the WQ sample. The lattice parameters of the  $\gamma$  phase were determined to be  $a = 4.100 \text{ \AA}$  and  $c = 4.138 \text{ \AA}$ , *i.e.*,  $c/a$  of 1.009, which is slightly more cubic than the  $c/a$  of 1.016 for stoichiometric  $\gamma$ . A complex substructure consisting of antiphase boundaries (APBs), stacking faults, microtwins, and dislocations in the  $\gamma$  phase can be seen in Figure 3(a). Electron diffraction analysis of many  $\gamma$  grains showed the occurrence of all six variants. Aside from face-centered cubic (fcc) twin-related variants, numerous contacting variants in perpendicular twin relation, *i.e.*, mutually

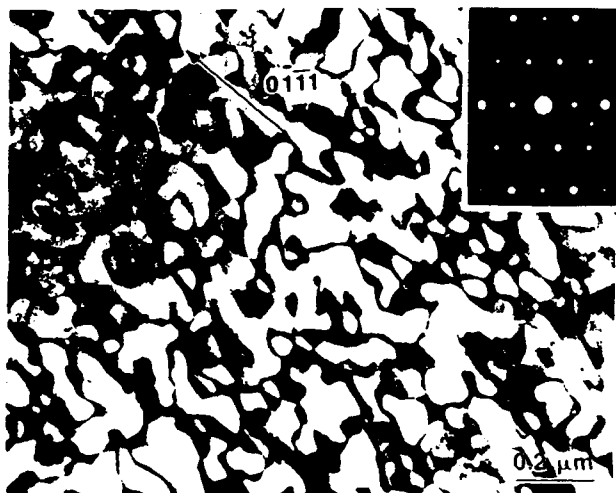


Fig. 2—DF TEM micrograph and inset  $[1\bar{2}13]$  SAD pattern showing the microstructure of  $\alpha_2$  in the Ti-47 2Al alloy held at 1400 °C for 1 h and WQ.

perpendicular  $c$ -axes, are observed. In fact, many of the boundaries between grains were observed to be intervariant boundaries. These observations suggest that a direct transformation from  $\alpha$  to  $\gamma$  had occurred, perhaps in a massive fashion. Pools of the lamellar ( $\alpha_2 + \gamma$ ) grains were also observed distributed sparsely between the  $\gamma$  grains. These presumably formed due to recalescence effects.

In order to establish that indeed a massive transformation had occurred, the samples were observed by back-scattered electron (BSE) imaging, and the chemical

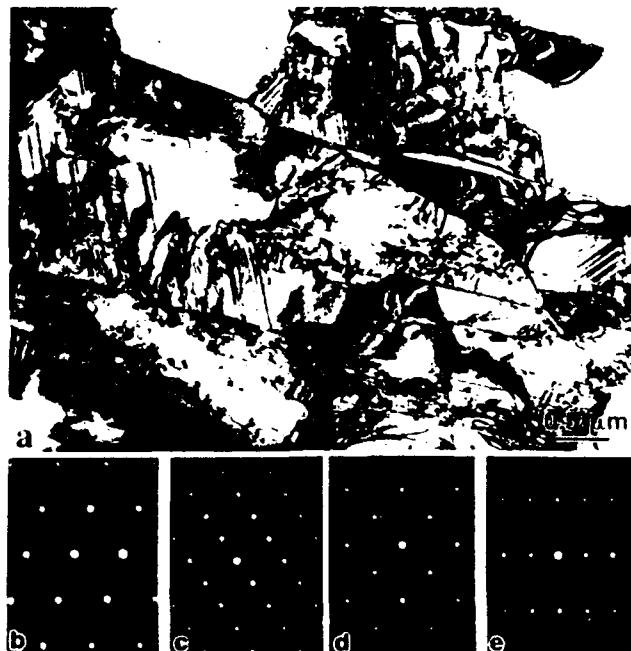


Fig. 3—TEM micrographs of Ti-47 2Al alloy held at 1400 °C for 1 h and WQ showing massively transformed  $\gamma$ : (a) BF micrograph and (b) through (e) are, respectively,  $[101]$ ,  $[110]$ ,  $[001]$ ,  $[010]$   $\gamma$  SAD patterns.

composition of the phases was determined by microprobe analysis. Thus, BSE micrographs of the WQ and IBQ samples are shown in Figures 4(a) and (b), respectively. The darker and lighter contrast regions correspond to  $\gamma$  and  $\alpha_2$ , respectively. Although the observation of contrast differences between the two phases indicates a difference in chemical composition, a microprobe scan analysis of the  $\alpha_2$  and  $\gamma$  regions extending through the interface, over a distance of  $\sim 700 \mu\text{m}$  at  $\sim 10\text{-}\mu\text{m}$  intervals (Figure 5), reveals that the compositions of the two phases are practically identical. Another feature observable in the SEM micrographs (Figures 4(a) through (b)) is that the interface seen in the optical micrographs (Figures 1(c) through (e)) often exhibits ledge features and planar and crystallographic facets, implying that it may actually be partially coherent, although this has not been established positively.

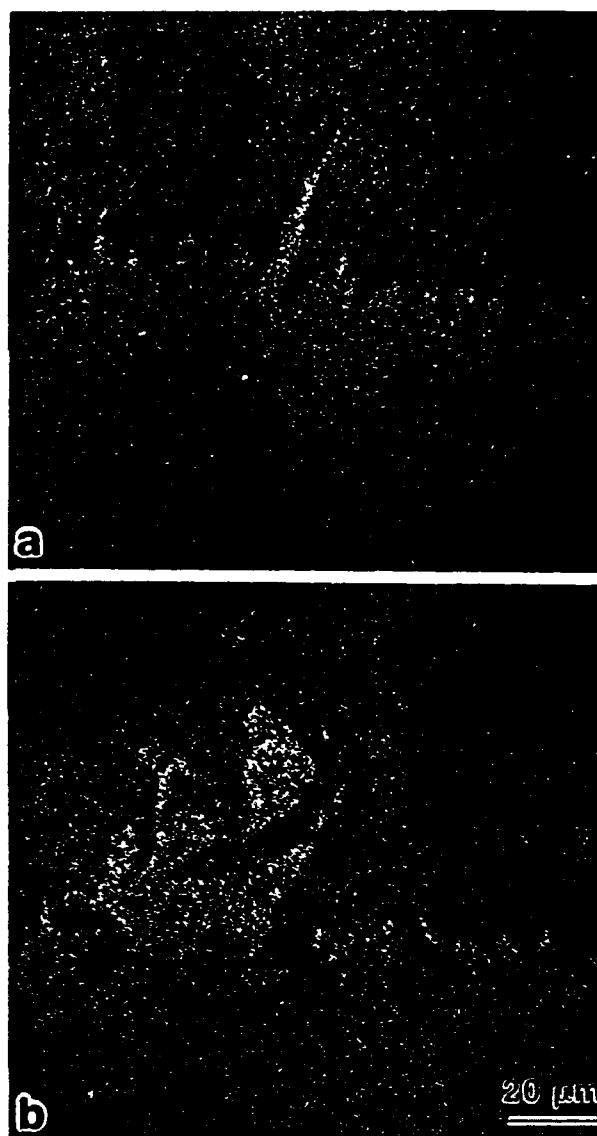


Fig. 4—Back-scattered SEM micrographs of Ti-47 2Al alloy. (a) WQ and (b) IBQ after a 1400 °C, 1-h treatment. The dark and light regions correspond to  $\gamma$  and  $\alpha_2$ , respectively.



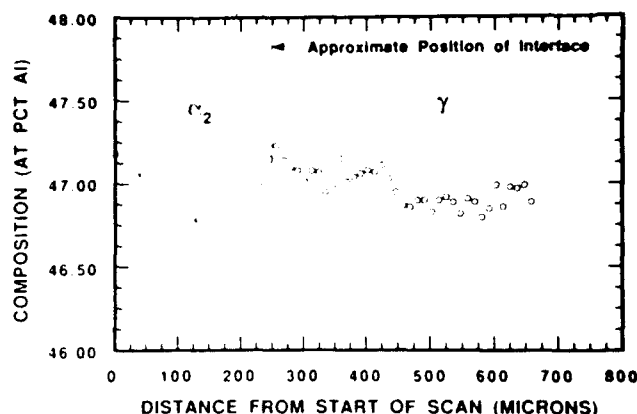


Fig. 5—Microprobe scan showing that the composition (at pct Al) of massive  $\gamma$  and  $\alpha_2$  phases in the Ti-47.2Al alloy held at 1400 °C for 1 h and WQ are practically identical.

Several points with regard to the BSE micrographs should be noted. Both the microprobe analysis and the BSE imaging were conducted on polished, unetched samples. The BSE micrographs in Figures 4(a) and (b) appear to indicate that the Al content of the  $\gamma$  phase is slightly higher than that of the  $\alpha_2$ . However, the microprobe analysis (Figure 5) does not show any such consistent trend that might support this. It was practically impossible to distinguish between the  $\alpha_2$  and massive  $\gamma$  regions under normal contrast settings in the SEM. At 75 pct of the maximum setting, differences in contrast became just discernible, becoming clearer at the maximum setting. It is possible that the contrast differences are produced by a channeling effect because of the difference in orientations of the two phases.<sup>12,11</sup> Were this the case, rotation or tilting of the sample should have produced changes/reversal in contrast, which was not observed. Based on these observations, it appears that the contrast differences seen in the BSE images may be associated with the differences in crystal structures and, possibly, density and defect structures of the two phases, although additional work is required to determine the exact cause. In any case, it is clear that the compositions of the  $\alpha_2$  and  $\gamma$  phases, within the experimental accuracy of the electron probe microanalysis technique, are nearly the same, which, together with TEM results, provides strong evidence for a massive transformation from  $\alpha$  to  $\gamma$  at high cooling rates.

To ascertain whether the transformations were sensitive to prior grain size, the extruded Ti-48Al alloy (#2) was heated to 1400 °C and cooled at various rates. Compared with the unextruded alloy (#1) with a grain size of 500 to 1000  $\mu\text{m}$ , the as-extruded microstructure is duplex (Figure 6(a)), consisting of primary  $\gamma$  and lamellar ( $\alpha_2 + \gamma$ ) grains with grain sizes of  $\sim 40$  and  $\sim 100 \mu\text{m}$ , respectively. The AC microstructure of the latter (Figure 6(b)) appears with a larger fraction of the Widmanstätten structure compared with that of the unextruded AC sample (Figure 1(b)). The WQ sample (Figure 6(c)) appears to have massively transformed to  $\gamma$  practically throughout the complete cross section of the sample. A feathery morphology for the massive product was also observed.

A BF TEM micrograph of the AC extruded sample is

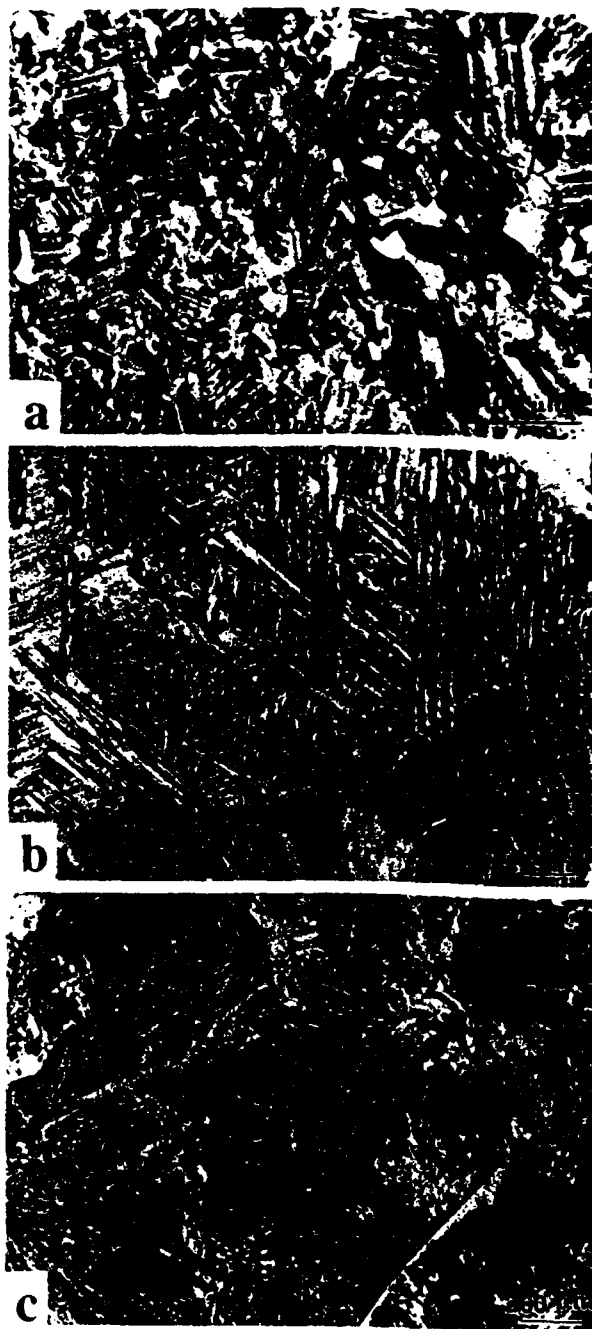


Fig. 6—Optical microstructures of Ti-47.86Al extruded alloy: (a) as-extruded and (b) and (c) AC and WQ, respectively, after a 1400 °C, 1 h treatment.

shown in Figures 7(a). The large feature present in the center of the micrograph corresponds to the Widmanstätten structure seen in the optical micrographs in Figures 1(b) and 6(b). By means of electron diffraction (Figure 7(b)), this structure was determined to be  $\gamma$ . Usually, three or four variants of  $\gamma$  were observed to be present within a Widmanstätten colony; a very thin layer of  $\alpha_2$  could also be detected. The micrograph in Figure 7(a) also shows the intragrain ( $\alpha_2 + \gamma$ ) lamellar structure, as established by the composite  $[110]_2 + [101]_1$ , twin  $\parallel [1\bar{1}20]_1$ , SAD

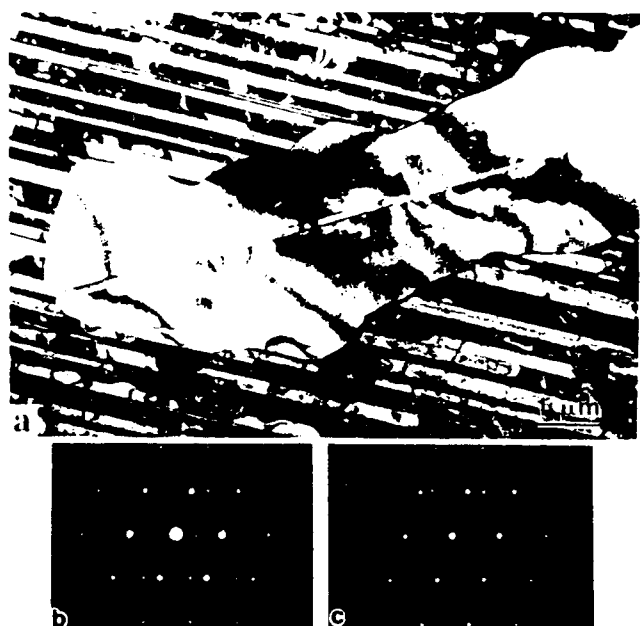


Fig. 7. (a) TEM micrographs of Ti-47.86Al extruded alloy AC after a 1400 °C, 1 h treatment. (a) BF micrograph showing Widmanstätten  $\gamma$  and  $(\alpha + \gamma)$  lamellar structure, (b)  $[101]\gamma \times [101]\gamma$  twin SAD pattern of Widmanstätten structure, and (c)  $[110]\gamma \times [101]\gamma$  twin  $\times [1120]\alpha$  SAD pattern from  $(\alpha + \gamma)$  structure

pattern in Figure 7(c). Transmission electron micrographs and SAD patterns taken from the extruded WQ alloy (Figure 8) establish that the  $\alpha$  has practically completely massively transformed to  $\gamma$ . In terms of defect structures, the  $\gamma$  appears with features very similar to those observed in the unextruded WQ alloy; a larger incidence of fcc twin-related variants was noted. Back-scattered electron images showed no observable differences in contrast, *i.e.*, were uniformly dark. Based on microprobe scan analysis, the composition of the alloy was determined to be uniformly near the value of 47.86 at. pct Al determined by wet chemical analysis.

The massive transformation has been extensively studied in the past.<sup>124,125</sup> Prominent examples of the massive transformation can be found in Cu-Zn,<sup>126,127</sup> Cu-Al,<sup>128</sup> Cu-Ga,<sup>129</sup> Ag-X,<sup>130,131</sup> Fe-Ni,<sup>132</sup> and Ti-X<sup>133</sup> alloys. Essentially, a massive transformation takes place by diffusional nucleation and growth and involves a change in crystal structure without a change in composition.<sup>124,125</sup> Generally, the massive transformation is observed provided competing equilibrium and other (namely, Widmanstätten) transformation modes are suppressed.<sup>124</sup> Usually, nucleation occurs at the grain boundaries of the parent phase, and growth always proceeds by a thermally activated process in which noncooperative transfer of atoms across relatively incoherent interfaces occurs.<sup>124,125</sup> In principle, a massive transformation can be observed in any system where the pertinent phase fields overlap in composition.<sup>124,125</sup> Moreover, it is possible for a massive reaction to be considered as occurring in the metastable two-phase field, such as that below a invariant reaction temperature (for example, eutectoid temperature). Significant penetration into an equilibrium or



Fig. 8. BF TEM micrograph and inset  $[101]\gamma \times [101]\gamma$  twin SAD pattern showing massively transformed  $\gamma$  in the Ti-47.86Al extruded alloy WQ after a 1400 °C, 1 h treatment

metastable equilibrium two-phase field can also occur during massive growth.<sup>125</sup>

The above conditions are adequately met around the two-phase  $(\alpha + \gamma)$  region in the Ti-Al system. The present study indicates that the  $\gamma$  may form from the  $\alpha$  in three morphologies depending on cooling rate, and therefore, undercooling. At low values, the lamellar morphology prevails; at slightly higher rates, the Widmanstätten structure appears; and at very high rates, the massive morphology is prevalent. The electron microscopy observations and the observed composition invariance provide strong evidence for the massive transformation from  $\alpha$  to  $\gamma$ . The extent of the Widmanstätten and massive morphologies also appears to depend on prior grain size. For instance, compared with the larger grain size unextruded sample, in the finer grain size extruded sample, the volume proportion of both morphologies is observed to increase, such that at the higher cooling rates, practically the entire sample is transformed to massive  $\gamma$ . One explanation for the difference in behavior can be forwarded based on a grain size effect. Since the unextruded samples of alloy 1 are characterized by a large grain size (500 to 1000  $\mu\text{m}$ ), fewer sites for nucleation of the massive  $\gamma$  exist. Once nucleated, these grow at high rates until the temperature drops sufficiently below 1125 °C to encounter the extended  $\alpha/\alpha'$  phase boundary, whereupon the transformation of the remaining  $\alpha$  to  $\alpha'$  intervenes and arrests further progression of the massive reaction. Another possible contribution comes from the higher Al content of the extruded material, which might permit the massive reaction to progress for longer times before the  $\alpha/\alpha'$  boundary is encountered. The relative contributions of these two effects is being investigated. Finally, while morphologically the Widmanstätten and massive  $\gamma$  structures appear different, there is uncertainty in distinguishing between the two in terms of mechanisms and temperature dependence, since the composition of the Widmanstätten  $\gamma$  has not been ascertained.

An important question relates to the temperature of nucleation of the massive  $\gamma$ . It is generally believed that the  $I$  line, *i.e.*, the locus of points at which the free energy of the two phases is equal, represents the limit

for the massive reaction and the distance between the  $T_0$  line and the temperature of the start of the reaction represents the undercooling and, therefore, the driving force for the massive transformation.<sup>[24,25]</sup> Hillert,<sup>[32]</sup> however, has argued that the massive transformation requires undercooling below the solvus line. Another point concerns the nature of the interface between the parent and the massive product. In this context, it is noteworthy that evidence for both incoherent and coherent growth during the massive transformation is a subject of much debate,<sup>[33]</sup> since the nature of the massive/parent interface varies from incoherent to semicoherent from system to system. Evidence for both the absence and presence of definite crystallographic relationships between the massive product and parent exists.<sup>[33,34]</sup> Even so, it has been argued that massive transformations must always involve special crystallographic relations (between the parent and the product), leading to coherent nucleation followed by growth, in which the interface changes from coherent to semicoherent and moves by a ledge mechanism.<sup>[34]</sup> Our current experimental evidence suggests that the interface between the  $\alpha_2$  and massive  $\gamma$  may be semicoherent. However, determination of the exact nature of the interface by the TEM will require foils in which the massive product, the parent, and the separating interface are present simultaneously, which is the subject of ongoing research. All of these aspects, together with the temperature and composition dependence and the nucleation and growth mechanisms of the different morphologies of  $\gamma$ , are the subject of ongoing research.

A final point concerns the possible role of oxygen and nitrogen. Various studies of the possible effects of interstitials were carried out in which the solution treatment time was varied from 15 minutes to an hour in both protected as well as unprotected samples. The interstitial contents analyzed following some of these treatments are

shown in Table I, from which it is clear that pickup of interstitials, particularly oxygen, is a function of time solutionizing and the protection scheme. At the longer times (1 hour), a fair amount of oxygen ( $\sim 0.3$  wt pct) appears to have been ingested into the samples compared with those at shorter times ( $\sim 0.096$  to  $0.14$  wt pct). (It is thought that the increased oxygen in many of these samples was caused by reaction with the glass ceramic coating or by contact with the quartz tubes used to protect the samples.) Even so, the microstructures of these samples cooled at various rates, including those cooled at high rates, with regard to the mode and morphology of the transformation products, remained essentially the same (Table I), suggesting that the interstitial contents do not exert a dominant influence on the transformation. Lastly, an important point to also be noted in Table I is that chemical analysis of the interior of the samples after removing  $\sim 2$  mm of the outer surface revealed that the pickup of oxygen was confined to the outer surface, whereas the interiors were practically unaffected.

In view of the foregoing, it is, nevertheless, interesting to examine the potential role that oxygen could play. In addition to the 48Al alloy, studies were also conducted on a nominal Ti-50Al alloy cooled at various rates from the  $\alpha$ -region. The behavior of the latter was similar to the 48Al alloy; both the Widmanstätten and massive  $\gamma$  morphologies were observed depending on cooling rate. Very recently, two publications, the first by Jones and Kaufmann<sup>[17]</sup> on phase equilibria and microstructures in TiAl-base alloys and the second on the effect of cooling rate on transformations of the  $\alpha$  phase in Ti-48Al-2Mn-2Nb alloys by McQuay *et al.*,<sup>[35]</sup> have appeared. Of particular interest to the present work are the results in the first on a 50Al alloy solution treated at  $1400^\circ\text{C}$  for 2 hours and  $1450^\circ\text{C}$ , for 1 hour and then WQ. The microstructures following these treatments are very

Table I. Oxygen, Nitrogen Contents, and Microstructure as a Function of Heat Treatment of Ti-47.86Al Alloy

Heat Treatment*	Wt Pct Oxygen	Wt Pct Nitrogen	Microstructure**
As-cast-hipped	0.049	0.006	L + $\gamma_p$
H + $1400^\circ\text{C}$ , 20 min, FC	0.096	0.009	L + little $\gamma_n$
H + $1400^\circ\text{C}$ , 1 h, FC	0.195	0.009	L + little $\gamma_n$
H + $1400^\circ\text{C}$ , 20 min, AC	0.104	0.008	L + $\gamma_n$
H + $1400^\circ\text{C}$ , 1 h, AC	0.255	0.011	L + $\gamma_n$
H + $1400^\circ\text{C}$ , 1 h, AC†	0.040	0.005	L + $\gamma_n$
H + $1400^\circ\text{C}$ , 20 min, OQ	0.133	0.008	L + $\gamma_n$ + $\gamma_m$
H + $1400^\circ\text{C}$ , 1 h, OQ	0.311	0.008	L + $\gamma_n$ + $\gamma_m$
H + $1400^\circ\text{C}$ , 20 min, WQ	0.119	0.009	mostly $\gamma_m$ + little $\alpha_2$ + L
H + $1400^\circ\text{C}$ , 1 h, WQ	0.285	0.008	mostly $\gamma_m$ + little $\alpha_2$ + L
H + $1400^\circ\text{C}$ , 1 h, WQ†	0.036	0.004	mostly $\gamma_m$ + little $\alpha_2$ + L
As-extruded (X)	0.065	0.033	L + $\gamma_p$
X + $1400^\circ\text{C}$ , 20 min, AC	0.140	0.033	L + $\gamma_n$
X + $1400^\circ\text{C}$ , 1 h, AC	0.319	0.158	L + $\gamma_n$
X + $1400^\circ\text{C}$ , 20 min, WQ	0.112	0.018	mostly $\gamma_m$ + little $\alpha_2$
X + $1400^\circ\text{C}$ , 1 h, WQ	0.270	0.119	mostly $\gamma_m$ + little $\alpha_2$
H + $1400^\circ\text{C}$ , 20 min (air), WQ	0.297	0.029	$\alpha_2$ + $\gamma_m$
H + $1400^\circ\text{C}$ , 1 h (air), WQ	0.900	0.180	$\alpha_2$ + $\gamma_m$
H + $1400^\circ\text{C}$ , 1 h (air), WQ†	0.052	0.005	$\alpha_2$ + $\gamma_m$

\*H = cast + hipped ( $1200^\circ\text{C}$ , 2 h, 105 MPa); X = as-extruded; FC = furnace cooled; AC = air cooled; OQ = oil quenched; and WQ = water quenched.

\*\*L = lamellar ( $\alpha_2$  +  $\gamma$ );  $\gamma_p$ ,  $\gamma_n$ , and  $\gamma_m$  are, respectively, primary, Widmanstätten, and massive  $\gamma$ .

†Analysis of interior of samples after removing  $\sim 2$  mm of outer surface.

similar to those observed by us in the 48 and 50Al alloys; both the Widmanstätten and massive morphologies could be noted. Indeed, it is significant that even though the measured oxygen and nitrogen contents after heat treatment in their study of the 50Al alloy differ appreciably for the two temperatures (oxygen 0.051 and 0.163 wt pct, nitrogen 0.021 and 0.09 wt pct, respectively), the microstructures are essentially the same. The microstructures observed at low (FC, AC) and high cooling rates (OQ, WQ) by McQuay *et al.* in alloys with an oxygen content of 0.08 wt pct after heat treatment are also very similar. Indeed, the occurrence of massive  $\gamma$  at high cooling rates in these alloys has been confirmed.<sup>[36]</sup>

Finally, in our study of the unextruded samples solution treated in air at 1400 °C for times from 15 minutes to an hour, the massive reaction was observed to be slightly lesser in extent near the outer surface compared to those in the protected samples (Table I). This might suggest that the high oxygen and nitrogen ingested into the surface regions of the former act to *inhibit rather than permit* the massive reaction from  $\alpha$  to  $\gamma$ . Alternately, it is possible that sufficient loss of Al occurred to prevent the massive transformation, since alloys with Al contents less than ~45 at. pct WQ from the fully  $\alpha$ -phase region transformed completely to  $\alpha_2$  and showed no evidence of massive  $\gamma$ . However, analysis of the Al content after heat treatment in both the surface and interior of the samples showed no appreciable change from the value before heat treatment. If indeed the ingestion of interstitial oxygen is able to produce such dramatic changes in the transformation mode, that, in itself, poses some rather intriguing questions with regard to how such a change is brought about, since oxygen is known to stabilize the  $\alpha$  phase. There is one instance, namely, pure Ti, where because of the addition of oxygen, a massive transformation from  $\beta$  to  $\alpha$  has been postulated to occur prior to the martensitic transformation.<sup>[37]</sup> Thus, one potential way in which oxygen could have an effect is by altering the  $\alpha$  and  $\gamma$  phase boundaries such that the overlap in compositions of the two phases at different temperatures is increased, thereby permitting the massive reaction to occur over a wider range of Al contents. Although the possibility that even very low levels of oxygen can produce such changes cannot be overruled, our current experimental evidence, together with the results of others<sup>[17,35]</sup> discussed in the foregoing, is consistent with the suggestion that the massive transformation is a real effect, not some chance consequence of ingestion of interstitials, particularly oxygen. Additional work on low oxygen alloys solutionized and quenched in vacuum has essentially confirmed this.

Support for this research from the Engineering Foundation, the Alcoa Foundation, and the State of Ohio Edison Materials Technology Center is deeply appreciated. The authors are thankful to the Air Force Materials Laboratory, Wright-Patterson AFB, Dayton, OH, for use of the extrusion and SEM facilities and to Mr. Cameron Begg for his help with the SEM and microprobe work.

## REFERENCES

1. H.A. Lipsitt: *MRS Symp. Proc.*, 1985, vol. 39, pp. 351-64.
2. M.J. Blackburn and M.P. Smith: U.S. Patent No. 4,294,619, 1981.
3. S.C. Huang and E.L. Hall: *MRS Symp. Proc.*, 1989, vol. 131, pp. 373-83.
4. Y.W. Kim: *MRS Symp. Proc.*, 1991, vol. 213, pp. 777-94.
5. T. Hanamura, R. Uemori, and M. Tanino: *J. Mater. Res.*, 1988, vol. 3, pp. 656-64.
6. D.S. Shih, S.C. Huang, G.K. Scarr, H. Jang, and J.C. Chesnutt in *Microstructure/Property Relations in Titanium Alloys and Titanium Aluminides*, Y.W. Kim and R.R. Boyer, eds., TMS-AIME, Warrendale, PA, 1990, in press.
7. Shyh-Chin Huang and Ernest L. Hall: *Metall. Trans. A*, 1991, vol. 22A, pp. 427-39.
8. M.J. Blackburn: in *The Science, Technology and Application of Titanium Alloys*, R.I. Jaffee and N.E. Promisel, eds., Plenum Press, New York, NY, 1970, vol. 3, pp. 633-43.
9. S.A. Jones, R.D. Shull, A.J. McAlister, and M.J. Kaufmann: *Scripta Metall.*, 1988, vol. 22, pp. 1235-40.
10. J.A. Graves, J.H. Perepezko, C.H. Ward, and F.H. Froes: *Scripta Metall.*, 1987, vol. 21, pp. 567-72.
11. J.J. Valencia, C. McCullough, C.G. Levi, and R. Mehrabian: *Scripta Metall.*, 1987, vol. 21, pp. 1341-46.
12. J.A. Graves, L.A. Bendersky, F.S. Biancanello, J.H. Perepezko, and W.J. Boettinger: *Mater. Sci. Eng.*, 1988, vol. 98, pp. 265-68.
13. C. McCullough, J.J. Valencia, C.G. Levi, and R. Mehrabian: *Acta Metall.*, 1989, vol. 37, pp. 1321-36.
14. E.L. Hall and S.C. Huang: *Acta Metall.*, 1990, vol. 38, pp. 539-49.
15. C. McCullough, J.J. Valencia, C.G. Levi, and R. Mehrabian: *Mater. Sci. Eng.*, 1990, vol. A124, pp. 83-101.
16. R.D. Shull and J.P. Clein: *High Temp. Sci.*, 1990, vol. 26, pp. 95-117.
17. S.A. Jones and M.J. Kaufmann: University of Florida, unpublished research, 1990.
18. J.L. Murray: in *Binary Alloy Phase Diagrams*, T.B. Massalski, ed., ASM, Metals Park, OH, 1986, pp. 175-78.
19. C.R. Feng, D.J. Michel, and C.R. Crowe: *Scripta Metall.*, 1988, vol. 22, pp. 1481-86.
20. C.R. Feng, D.J. Michel, and C.R. Crowe: *Phil. Mag. Lett.*, 1990, vol. 61, pp. 95-100.
21. D.S. Schwartz and S.M.L. Sastry: *Scripta Metall.*, 1989, vol. 23, pp. 1621-26.
22. Y.S. Yang and S.K. Wu: *Scripta Metall.*, 1990, vol. 24, pp. 1801-06.
23. J.I. Goldstein, D.E. Newberry, P. Echlin, D.C. Joy, C. Fiori, and E. Lifshin: in *Scanning Electron Microscopy and X-Ray Microanalysis*, Plenum Press, New York, NY, 1981, pp. 75-87 and 156-62.
24. T.B. Massalski: in *Phase Transformations*, ASM, Metals Park, OH, 1970, pp. 433-86.
25. J.H. Perepezko: *Metall. Trans. A*, 1984, vol. 15A, pp. 437-47.
26. T.B. Massalski: *Acta Metall.*, 1958, vol. 6, pp. 243-53.
27. D.A. Karlyn, J.W. Cahn, and M. Cohen: *Trans. AIME*, 1969, vol. 245, pp. 197-207.
28. J.H. Perepezko and T.B. Massalski: *Acta Metall.*, 1975, vol. 23, pp. 621-31.
29. J.D. Ayers and T.B. Massalski: *Metall. Trans.*, 1972, vol. 3, pp. 261-71.
30. W.D. Swanson and J.G. Parr: *J. Iron Steel Inst.*, 1964, vol. 202, pp. 104-06.
31. M.R. Plichta, H.I. Aaronson, and J.H. Perepezko: *Acta Metall.*, 1978, vol. 26, pp. 1293-1305.
32. M. Hillert: *Metall. Trans. A*, 1984, vol. 15A, pp. 411-19.
33. T.B. Massalski: *Metall. Trans. A*, 1984, vol. 15A, pp. 421-25.
34. M.R. Plichta, W.A.T. Clark, and H.I. Aaronson: *Metall. Trans. A*, 1984, vol. 15A, pp. 427-35.
35. P. McQuay, D.M. Dimiduk, and S.L. Semiatin: *Scripta Metall.*, 1991, vol. 25, pp. 1689-94.
36. P. McQuay and V.K. Vasudevan: University of Cincinnati, Cincinnati, OH, unpublished research, 1991.
37. M. Cormier and F. Claisse: *J. Less-Common Met.*, 1974, vol. 34, pp. 181-89.

RI-B-90-04

**Elimination of Abnormally Large Grains in Hot-Worked  
Billets of High-Temperature Nickel-Base Alloys**

Professor Steven W. Thompson  
Department of Metallurgical and Materials Engineering  
Colorado School of Mines

#### 4.0 SUMMARY

A series of hot-compression tests were conducted on coarse-grained wrought alloys, Monel K-500 and alloy 718. The most interesting results came from tests conducted with a deformation level of 30%, a temperature of 1125°C, and a strain rate of  $1.0 \text{ s}^{-1}$ . A major difference in recrystallization behavior between the two alloys was observed. In particular, the overall recrystallization rate for Monel K-500 was higher than that for alloy 718; however, the nucleation rate at boundaries in the Monel alloy was extremely variable, and this feature gave rise to large "patches" in the microstructure which remained unrecrystallized even after about 50% of the microstructure had recrystallized. Some "patches" were larger than 1.5 millimeters, which would correspond to a size greater than 100 millimeters in typical castings of this alloy. It is postulated these phenomena are responsible for the observation of very coarse grains in billets of Monel K-500. In contrast, alloy 718 exhibits a well-defined "necklace" structure which results from a rather uniform nucleation rate at almost all grain boundaries. As a result, the microstructures of billets of alloy 718 should be uniformly fine grained. Recommendations for improving the uniformity of microstructure in billets of Monel K-500 are included in the body of this report.

RI-B-90-05

**Experimental Investigation of Attenuation Characteristics of  
Subsurface Materials**

Professor Young Jin Mok  
Department of Civil Engineering  
Kansas State University

## ABSTRACT

The primary use of in situ seismic measurements in soil is to evaluate wave velocities and, hence, to characterize elastic moduli. However, material damping characteristics of soil are also important but are rarely measured in situ. The crosshole seismic method is shown to be a very useful method for performing attenuation (damping) measurements at small strains.

To initiate developing a field method of measuring in situ attenuation characteristics, testing equipment and a test site developed and characterized. Some of important variables associated field implementation of damping measurements were investigated. Important variables are: 1. the frequency content of the waveform, 2. the ratio of the wavelength to the source-receiver spacing, 3. the frequency characteristics of receivers in boreholes and 4. the quality of casing and grouting. The use of windowing time-domain records to minimize interference from reflected and refracted waves and the calculation of spectral ratios in the frequency domain are necessary approaches to data processing in these tests. Also, difference in frequency characteristics between two receivers in boreholes play a major role in damping measurement.

Recommendations are suggested for further study as follows:

1. the test site needs to be fully characterized by using other in situ testing technique such as Standard Penetration Test, Cone penetration Test and Pressuremeter and can, thus be designated as a one of national geotechnical experimentation sites
2. The effect of casing and grouting on damping measurements should be investigated. That can be done by drilling holes and burying receivers at specific depths without casing and grouting.
3. The Utilization of SH-waves on damping measurements is recommended. Further refinement of the in-hole source with a solenoid developed in this project is expected to make it possible.



RI-B-90-06

**Quantitative Stereology of Concrete Microcracking**

Professor Kim D. Basham  
Department of Civil and Architectural Engineering  
University of Wyoming

## **Executive Summary**

The following semiannual progress report is submitted in partial fulfillment of the requirements of the Air Force Engineering Foundation Grant RI-B-90-06. The final report is due October 15, 1991.

## **Introduction**

The specific aim of this research is to develop an automated technique for quantifying concrete microcracking using the principles of quantitative stereology (Underwood, 1970). The goal is to investigate the automation of the oriented secant method either by a digitized system or by using an image analyzer, and to determine the effectiveness of this computerized procedure in characterizing concrete microcracking. Data on concrete cylinder specimens subjected to uniaxial compression obtained by Cornell University investigators in the mid-1960's is being used to establish the validity of this automated method. (Hsu, et al., 1963). The Cornell investigators used a cumbersome and difficult procedure to measure and relate concrete microcracking to uniaxial stress-strain curves. The fully computerized, automated method being developed uses the oriented secant method to quantify internal microcracking. This automated procedure will enable investigators to efficiently characterize concrete microcracking with respect to density and orientation. For more information concerning the Cornell work and the oriented secant method please see original proposal entitled "Quantitative Stereology of Concrete Microcracking."

RI-B-90-07

**Compression Strength of Composite Laminates**

Professor Dimitris Lagoudas  
Department of Civil Engineering  
Rennsselaer Polytechnic Institute

## COMPRESSIVE FAILURE DUE TO KINKING OF FIBROUS COMPOSITES

by

Dimitris C. Lagoudas and Ahmed M. Saleh

Department of Civil and Environmental Engineering  
and Institute Center for Composite Materials  
Rensselaer Polytechnic Institute, Troy, NY 12180

### ABSTRACT

This work addresses the important engineering problem of the compressive strength of fibrous laminated composites, bridging the micromechanics relevant to compressive failure due to fiber kinking with the global characteristics of a composite structure. Simple modeling incorporates the influence of boundary conditions, laminate thickness and lay-up configuration, as well as the importance of the micro-geometry. The mechanism of failure under compression is assumed to be micro buckling of fibers that localizes and leads to the formation and, under critical conditions, propagation of kink bands. To analyze the mechanics of kinking and calculate the critical compressive stress, a steady state kink propagation model is utilized for the layers under compression in the fiber direction. The analysis results are used to gain a better understanding of the influence of the macro-geometry in addition to the micro-geometry and the fiber and matrix material properties. The predictions of the model are compared with experimental results for carbon/thermoplastic unidirectional laminates under direct compression and cross-ply laminates under four-point bending.

RI-B-90-08

**Friction Mechanism of Granular Material Along an Interface**

Professor Samuel G. Paikowsky  
Department of Civil Engineering  
University of Lowell

# **Friction of Granular Material Along an Interface:**

## **Mechanical Modelling**

**By Samuel G. Paikowsky<sup>1</sup>, Member , ASCE**

### **Abstract**

The need to predict the friction along an interface between a solid body and granular material exists in many different disciplines. However, there is currently no model which describes or explains this friction/shear mechanism. The controlling parameters of this mechanism are studied through a mechanical model enabling to predict the friction coefficient at the interface. This mechanical model (S.G. - Sphere in the Groove) considers the micro behavior of granular material examining a single rigid grain (sphere or ellipsoid) supported by adjacent particles (frictional groove) and subjected at an additional contact point, to normal and traction forces. These forces can result from a moving frictional plane (modeling the body in contact along an interface) or from the motion of an adjacent particle (modeling shear conditions within the granular material itself).

Based on observations of granular soil behavior, the S.G. model assumes that the grain will roll or slide along the groove between the supporting particles. A limiting equilibrium analysis is applied to the interface and interparticle contacts, examining the possibility of sliding or rolling in both locations. A companion paper examines the S.G. model in light of experimental work measuring the friction of sands along interfaces. These analyses are then followed by simplified relations describing the coefficient of friction between quartzic sand and solid bodies.

---

<sup>1</sup> Ass't Professor, Dept. of Civil Eng., University of Lowell, Lowell, MA 01854.

RI-B-90-09

**A System for the Measurement of a Component Concentration  
in Two-Phase (Air-Water) Flows in Rectangular Channels**

Professor Jerzy K. Keska  
Department of Mechanical Engineering  
University of Nebraska-Lincoln

# **A SYSTEM FOR THE MEASUREMENT OF A COMPONENT CONCENTRATION IN TWO-PHASE (AIR-WATER) FLOWS IN RECTANGULAR CHANNELS**

Grant R1-B-90-9

Final Report, September, 1991

Principal Investigator

**JERRY K. KESKA, D. Sc. Eng.**

Associate Professor of Mechanical Engineering

University of Nebraska

Lincoln, NE 68588-0656

## **Conclusions and Suggestions for Future Work**

An instrument has been developed which can be used to measure spatial concentration in an air-water mixture. The instrument not only provides the capability for spatial concentration determination, but also allows for the measurement of water film thickness as well as potential for flow pattern identification including identification of the transition regions between flow patterns. The instrument (CAC) effectively measures the spatial concentration and film thickness of water and air in the active space of the capacitive sensor in nonobstructive manner.

Visually observed flow regimes (CCD system and flow visualization system) were compared with fluctuation of spatial concentration, where the frequency distribution (FDC) and the cumulative frequency distribution (CFDC) curves of spatial concentration were the characteristics chosen to be discriminators of the flow pattern.



The project also resulted in a number of conclusions relevant to instrument development and implementation:

1. Increasing the number of capacitive sensors may provide several benefits including increased resolution and more accurate measurements, and identification of the interpretative algorithm as well as control of a calibration status.
2. The electrodes should be approximately in the range of 0.1 to 2 diameters in length; longer electrodes will yield larger averaging in the output while shorter lengths will result in some decrease of the measured delta value. For average cross-sectional spatial concentration analysis, rapid response time is not crucial. However, for time dependent analysis, as in the measure of spatial concentration fluctuations (AC component), a minimum electrode length is desirable to minimize spatial averaging in this parameter value.
3. In order to obtain an accurate concentration value in water-air mixture, the correction factor for each flow pattern should be carefully determined and evaluated. It is suggested that the mathematical model with on-line flow pattern detector should be further developed in order to increase accuracy.
4. Two types of capacitive sensors have been employed in the present study (types I and III), and the sensors seems to be reliable and stable enough as a base for further optimization process of the sensors for the measurement of spatial concentration and film thickness of a liquid in a channel.
5. The effects of spatial concentration and the temporal and spatial distribution, as well as a configuration of a capacitive sensor on the sensor characteristic are significant.

It should be noted that the general conclusions drawn regarding the capacitive type concentration meter for water-air mixture are of a preliminary and a exploratory nature. No extensive study of such parameters as: temperature, conductivity, size and configuration of electrodes, dielectric constant, sensor

configurations, etc..., was undertaken. It is recommended that further research needs to be made as follows:

- \* The computed spatial concentration is somewhat flow regime dependent. Correction factors could be incorporated to compensate this process.
- \* The shape of the FDC possesses a high potential for use in objective determination of flow patterns in two-phase flow. It should be noted that further study of the flow pattern identification would seem to be recommended.
- \* The experimental evidence obtained in this study indicates that many variables effect the capacitance of the sensor and that establishment of the desired value may be difficult. It is suggested that calibration test need to be developed for a high controllable conditions for such variables as spatial concentration and its temporal and spatial distribution, and sensor configuration.

RI-B-90-10

**Effects of Reinforcement Geometry on Inelastic Deformation  
in Metal-Matrix Composites**

Professor David G. Taggart  
Department of Mechanical and Applied Mechanics  
The University of Rhode Island

## Chapter 1. Overview

This report summarizes the results of the research program, "Effects of Reinforcement Geometry on Inelastic Deformation in Metal-Matrix Composites," sponsored by the Air Force / Engineering Foundation Grant RI-B-90-10. This research program consists of both analytical and experimental phases.

The analytical phase is the development of an appropriate micromechanics model to predict the elastic-plastic response of metal-matrix composites with ellipsoidal inclusions. The elastic-plastic response of metal-matrix composites has received considerable attention in recent years. Due to the complex microstructure of these materials, analytical modeling efforts are forced to idealize the geometry in order to define solvable boundary value problems. The study of the elastic-plastic response parallels earlier studies of the elastic response. Typical approaches for the elastic properties include the use of dilute approximations (Dewey, 1947), self-consistent approximations (Hill, 1965 and Budiansky, 1965), idealized geometries (such as Hashin's composite sphere model (1962), Hashin and Rosen's composite cylinder model (1964), and Christensen and Lo's (1979) three-phase model), and approximate methods based on the so-called Mori-Tanaka (1973) method. Many of these models make use of Eshelby's (1957) elasticity solution for a single ellipsoidal inclusion in an infinite matrix. In the present study, the dilute, self-consistent and three-phase models are extended to study the composite elastic-plastic response. Since closed form plasticity solutions (analogous to Eshelby's solution) are not available, numerical elastic-plastic solutions are obtained to provide dilute and three-phase estimates of the effects of reinforcement geometry on the composite elastic-plastic response. A generalized formulation has been developed to allow direct comparisons between the dilute, self-consistent and three-phase model. For the case of spherical inclusions, a Rayleigh-Ritz procedure is used to solve the boundary value problems defined by each model. The results of the three models are compared and discussed in detail in Chapter 2 of this report as well as in the recent paper by Taggart (1991). It is concluded that the three-phase approach provides reliable, reasonable estimates of the macroscopic response as well as details of the microstructural deformation mechanisms.

Since the dilute approximation of the elastic-plastic response is a straightforward (yet numerically intensive) calculation, the effects of reinforcement geometry are first studied using the dilute approach. The boundary value problem defined by the dilute model is that of a single inclusion embedded in an infinite elastic-plastic matrix subjected to remote uniaxial stressing. To solve this problem, a elastic-plastic finite element analysis program was developed and applied to the case of ellipsoidal inclusions of various aspect ratios. Note that the numerical approach allows for future studies of arbitrary axisymmetric inclusion geometries. While the results of the dilute model are expected to be valid only for very low inclusion volume fractions, it is anticipated that the qualitative trends will be consistent with improved models. Chapter 3 summarizes the results of the development and application of a dilute model for the effects of inclusion geometry on the composite elastic-plastic response. These results are also presented in the recent paper by Adley and Taggart (1991).

In chapter 4, the three-phase model studied in chapter 2 for the case of spherical inclusions is extended to study the effects of reinforcement geometry on the composite elastic-plastic response. For the case of ellipsoidal inclusions, the application of the three-phase model requires additional assumptions which are not required for the case of spherical inclusions. The assumptions are discussed and evaluated in detail in chapter 4. As in the case of spherical inclusions, the dilute and three-phase approximations provide similar results at low inclusion volume fractions. At increased volume fractions, the three-phase model is shown to provide a stiffer composite response.

The experimental phase of the program is summarized in Chapter 5. This study consists of both microstructural and mechanical characterizations of commercial extruded metal-matrix composites with both particulate and whisker reinforcement geometries. The microstructural characterization consists of both optical and scanning electron microscopy of the as-received composite microstructure. Quantitative analysis of these micrographs provide information as to the reinforcement geometry, aspect ratio, volume fraction, orientation and distribution. Additional microstructural characterization consist of the examination fracture surfaces and internal damage associated with mechanical loading. These results give insight into the critical failure mechanisms. The mechanical tests consists of uniaxial tension tests of specimens sectioned both parallel and normal to the extrusion

direction in both the as-received state and after the heat treatment recommended by the supplier. The elastic-plastic response for these composites are compared to each other and correlated with the analytical predictions. It is concluded that for the case of particulate composites, for the material system and inclusion volume fraction evaluated, the dilute and three-phase models give nearly identical estimates of the composite response. The predicted elastic modulus and post-yield strain hardening agrees with the observed behavior but the predicted yield stress underestimates the experimental yield stress. For the case of whisker reinforced composites, both models give good estimates of the elastic modulus and overestimate the composite yield stress. The three-phase model gives a good estimate of the post-yield strain hardening behavior while the dilute model underestimates the strain hardening. The discrepancies between the experimental and theoretical results are attributed to the models' failure to consider the effects of processing induced residual stresses and internal damage mechanisms. Future studies into the effect of residual stresses and damage mechanisms on the composite macroscopic response are planned.

RI-B-90-11

**Wake-Body Interactions and the Formation of Vortex Shedding  
Behind Bluff Bodies**

Professor Paul J. Strykowski  
Department of Mechanical Engineering  
University of Minnesota

## Wake-Body Interactions and the Formation of Vortex Shedding Behind Bluff Bodies

### Abstract

The present study investigates the flow around a circular cylinder for the range of Reynolds numbers of  $49 < Re < 300$ . A thorough investigation was done on the boundary conditions such that a 'universal' relationship between the Strouhal number and Reynolds number was established. The boundary conditions considered included flow uniformity, cylinder vibration, and cylinder end conditions. The effect of the hot wire probe on vortex shedding frequency was also examined.

An investigation on the control of vortex shedding was also done. A small-diameter circular cylinder was maneuvered parallel to the main cylinder in the near wake region. At low Reynolds numbers the control cylinder was able to suppress the formation of the vortex street. At a higher Reynolds numbers the effect was to suppress the formation of three-dimensional vortex structures. This control study determined that actions in the shear layer close to the cylinder were responsible for the formation of the vortex street. Furthermore, the changes in the wake shear layer, brought about by the control cylinder, could be correlated to alterations in the pressure field at the cylinder itself.



RI-B-90-12

**Investigation of Mechanical Response During  
Phase Transitions in Polymers**

Professor Mehrdad Negahban  
Department of Engineering Mechanics  
University of Nebraska-Lincoln

## Overview

Crystallization in polymers is a gradual process. In some polymers the completion of this process can take several years. This process can normally be accelerated by subjecting the material to strain. In all cases the characteristics of the resulting polymer is a function of the process under which the crystallization takes place.

To characterize this process we have developed a mathematical model which is presented in chapter 2. This model is based on an averaging procedure that evaluates the constitutive equation for the Cauchy stress from averaging the effective response of the amorphous (not crystallized) part of the material and an array of continuously developing crystals.

In chapter 3 the proposed model has been further developed to represent those materials which the change in volume is only related to crystallization. The model has been fit to results for the crystallization of natural rubber and the predictions of the resulting model for homogeneous deformations has been presented. Included in these results are the definitions of elastic modulus, shear modulus, and Poisson's ratio for a crystallizing material which is under large deformations. In addition to evaluating how these quantities change in the process of unconstrained crystallization and crystallization under uniaxial extension, the residual strain is evaluated. This part of the work was prepared and sent for publication.

The anomalous behavior seen by Rosen, Kolsky, and Pipkin [2] and Kolsky and Pipkin [1] for a torsional oscillator with two cylindrical torsional springs made from natural rubber is studied in chapter 4. This study is done in terms of the proposed model and it is shown that the model proposed for crystallization can predict the behavior of the oscillator.

The behavior of polyethylene is studied in chapter 5. An overview of the work done on the mechanical behavior of polyethylene is presented. The results from a set of modified stress relaxation tests done at 10%, 30%, and 60% strain at room temperature are presented. The modification to the stress relaxation was the addition of small jumps on the initial strain which were used to evaluate the elastic modulus at fixed intervals. The results from similar tests done at 30% strain and at 35°C, 45°C, and 55°C are also presented.

Concluding remarks are given in chapter 6.

RI-B-90-13

**In-Situ Fatigue Experiments in the High-Voltage Transmission  
Electron Microscope**

Professor M. E. Kassner  
Department of Mechanical Engineering  
Oregon State University

## PROJECT SUMMARY

The metal-fatigue phenomenon is poorly understood, partially because the dislocation dynamics of reversed deformation have not been characterized. This is because there has been, in the past, only limited success with direct observation of dislocations during cyclic deformation, such as with in-situ cyclic or reversed plastic deformation tests in the transmission electron microscope (TEM). This is due to problems associated with buckling of thin foils when an applied tensile or shear stress is reversed. Analysis shows that dislocation movement can be reversed by tensile stressing in alternating perpendicular directions (i.e., 90° rotations of a tensile stress in "X" and "Y" directions), and buckling of the foil can be avoided. A new specimen holder was designed by the principal investigator for performing such X-Y mechanical tests in-situ in the TEM. Recent tests supported by one-year funding by an AFOSR-Engineering Foundation Faculty Research Initiation Grant and a NATO Collaborative Research grant have provided significant preliminary success. With some experimental modifications, it is believed that a superior series of in-situ reversed deformation and fatigue experiments in the TEM can finally be performed. These experiments would provide new insights into reversed deformation phenomena, such as the Bauschinger effect and fatigue.

RI-B-90-14

**The Structure of Wakes Behind Various Bluff and Non-bluff Bodies**

Professor Barsam Marasli  
Department of Mechanical Engineering  
The University of Maryland

## 1. Introduction and background

Wake flows behind a variety of bodies ranging from circular cylinders to square rods and screens to airfoils have been studied extensively (Strouhal (1878), Rayleigh (1879), Karman (1911), Roshko (1954), Sato and Kuriki (1961) and others). Studies in the turbulent cylinder far wakes by Townsend (1947, 1949) led to the early ideas of self-preservation and Reynolds number independence (Townsend 1956). Townsend postulated that, sufficiently far downstream of the cylinder, an asymptotic self-preserving state is achieved for which the flow can be described by a single velocity scale  $u_0$  and a single length scale  $L_0$  (see figure 1 for nomenclature).

It has been well established (Uberoi & Freymuth 1969, Yamada *et al.* 1980) that far wake flows are self-preserving. It can be shown that (see for example, Wygnanski *et al.* 1986) the nondimensional velocity and length scales vary as

$$\left(\frac{U_\infty}{u_0}\right)^2 = A \frac{x - x_0}{2\theta}, \quad (1)$$

and

$$\left(\frac{L_0}{\theta}\right)^2 = B \frac{x - x_0}{2\theta}, \quad (2)$$

where, the constants  $A$  and  $B$  indicate the spreading rate of the wake, and  $x_0$  is the virtual origin. These constants would have to be identical for all wakes if the self-preserving state were *universal*.

Marasli (1983) and Wygnanski *et al.* (1986) conducted experiments to determine whether a universal self-preserving wake exists. For this purpose a set of experiments were designed to investigate the wakes of porous screens of various solidities. A solid strip was also considered as a limiting case of 100% solidity. The width of the screens were varied to keep the momentum thickness,  $\theta$ , (hence the drag) constant at approximately 2.5 mm. The free stream velocity was 14.5 m/sec. The results are depicted in figure 2 which shows the evolution of the centerline velocity deficit  $u_0$  with the nondimensional streamwise coordinate. Solid lines are linear least square fits to the points in the far wake where self-preservation is achieved. The self-preservation of each wake was established from the turbulence intensities, which did not vary with  $x$  when normalized by the local velocity and length scales. It is clear that the each of these wakes develop differently, indicating that the self-preserving states are not universal. This is attributed to the different initial conditions and the evolution of large scale coherent structures in the wake. The slope of each line in figure 2 increases with increasing screen solidity. However, the wake of the solid strip spreads the slowest, in contrary to the

expected order. This behavior is quite puzzling and has not yet been resolved.

One possible explanation for this unexpected behavior may be given when the near wakes of these bodies are considered. Castro (1971) reported that porous bodies with solidity greater than 80%, shed vortices. If we use his observation as a gage and assume that there was no vortex shedding from the screens used in our experiments, (the least porous screen used had 70% solidity,) this leaves the solid strip as the only shedding body. Monkewitz & Nguyen (1987) and Triantafyllou *et al.* (1986) report predictions of the Karman vortex shedding frequency behind circular cylinders via linear stability analysis of the near wake velocity profile. Profiles with large velocity deficits are absolutely unstable (see Huerre and Monkewitz 1985) where an impulsively generated small pulse grows in place and the system acts as a self-driven oscillator. If the pulse is convected away, then the profile is said to be convectively unstable, which is the case for smaller deficit wakes. There is encouraging evidence that shedding is a product of absolute instability (see Monkewitz & Nguyen 1987). It is not clear why vortex shedding should affect the far wake behavior, since Karman type vortices are known to decay exponentially with  $x$ . Nevertheless, the possible contrast between the far fields of absolutely unstable wakes versus convectively unstable wakes may help clarify the puzzle stated earlier.

An important question remains unanswered about the relationship between the near and far wakes. Can the far wake of a body be predicted from its near field characteristics? We have some evidence that (Wynanski *et al.* 1986) the spreading rate of the wake in the far field is related to the near field fluctuation intensity. Figure 3 shows the streamwise evolution of the maximum turbulence intensities for the screens. Notice that the 70% screen has the highest initial value, followed by the 45% and 30% solidity screens. Unfortunately, the near field data for the solid strip is not available, since at the time the main focus of the research was the far wake. Nevertheless, it seems like high near field turbulence intensity translates to faster spreading of the wake, which we proposed to establish for a variety of wake generators and Reynolds numbers.

It is very promising that the slope of the straight lines shown in figure 2 can be estimated from one measurement in the near wake of the generator. The prediction of the far mean field then would be complete if the virtual origin,  $x_0$ , could be obtained from the near wake data. Recall that  $x_0$  is the  $x$ -intercept of the straight line going through the far wake data. Wynanski *et al.* (1986) mention that  $x_0$  is used to account for Reynolds number effects. However the available data is inconclusive in any respect. The nondimensional quantity  $x_0/2\theta$  for the screen data presented here are 58, 27, -21 and -64 in increasing order of solidity, which does not correlate with the spreading rates. We do not know whether the 70% screen was shedding vortices, and earlier we discussed the possibility of its being a

non-shedding generator based on the observations of Castro (1971). However, if it were shedding, (which is quite possible since 70% is very close to Castro's threshold value of 80%) then a negative  $x_0$  would be indicating a shedding body. Marasli (1983) reports negative virtual origins for a circular cylinder and a roughened airfoil (also known to be shedding) and positive  $x_0$  for a nonshedding flat plate. Then, the question is: how does the shedding characteristics of a wake relate to the translational shift in its spreading? We claim that the stability characteristics of the near field fluctuations are responsible from this translation effect. Marasli (1991) presented a discussion describing the basis for this claim.

Several important questions remain unanswered about the relation between the near and far wake behaviors.

- Can the spreading of the far wake be predicted from the near wake characteristics?
- From far field measurements what can we say about the initial conditions? What can we say about the wake generator itself?
- What is the physical meaning of the virtual origin? Can it be predicted from near wake measurements only?
- What is the effect of vortex shedding on the development of the wake? Do absolutely unstable wakes have different far field structures than convectively unstable wakes?

We proposed to conduct experiments in the near and far wakes of various wake generators in order to substantiate the claims made in the previous section regarding these questions. We would like to establish a quantitative link between the initial conditions and the far wake behavior. For this purpose we proposed a systematic investigation of wakes behind screens, flat plates, circular cylinders etc. and correlate the wake spreading and the virtual origin to the possible vortex shedding or the amplitude of the disturbances in the near field.

During the initial stages of the grant period, our efforts were concentrated on making the wake measurements feasible in the University of Maryland Turbulence Research Laboratory. The results of the feasibility studies were presented in the progress report (Marasli 1991). We also spent some effort on the development of a special probe which would enable us to measure the vorticity field in the wake. Our initial attempt regarding the vorticity probe development was also presented in Marasli (1991). In this final report we shall present the results of the studies done on the screen wakes and our more recent efforts on the vorticity probe development.



## 2. Wake studies of screens with various solidities

Near wake studies have shown that there are two main types of wake generators: ones that shed vortices into the flow and ones that do not. Immediate flow fields behind these two types of wake generators are radically different and lead to different types of flow development far from the body. Unsteady forces induced are vastly different and at times might lead to resonant vibrations of the wake generator.

We conducted experiments in the University of Maryland Turbulence Research Laboratory to study some of the details of the wakes behind screen with various solidities from 30% to 100%. The widths of the screens were varied to keep the momentum thickness (hence the drag) constant. Wakes were visualized using the smoke-wire technique. Snapshots of the flow behind some of the screens are shown in figure 4. The solidities of the screens increase from top to bottom and they are 30%, 56%, 71% and 100% respectively. The free stream velocity was 3 m/s. It appears that the wake width increases with solidity except for the 100% case. This observation is in accord with our previous measurements and the reason for this peculiar behavior is unknown.

The near wakes of these various generators are quite different. The 30% screen creates two mixing layers, one on each side, which initially evolve independently from one another and merge further downstream to form a wake. Shear layer instabilities which develop into distinct roll-ups characterize this wake. The 56% screen presents a larger obstacle to the flow, hence the flow is fully turbulent immediately following the generator. Some traces of organized motion is evident. The 71% screen creates a wake which is quite similar to that of a circular cylinder. Vortices are shed from the body at a certain frequency which does not change streamwise distance. The 100% solidity screen does not show much structure except very close to the body where hints of von Karman shedding are present.

Hot-wire measurements of the wakes of these screens are presented in figure 5. The quantity  $L_0 U_\infty / u_0 \theta$ , which we shall call the wake growth parameter (Marasli 1989, Marasli *et al.* 1991, 1992), represents the spreading of the wake, and is plotted versus the nondimensional streamwise coordinate  $x/\theta$ . The growth parameter can be shown to vary linearly for the self-preserving far wake ( $x/\theta > 600$ ). In this phase of the present project we concentrated on the near wake, hence the growth parameter need not vary linearly with  $x/\theta$ . The variation of the growth parameter for the 30% and 56% screens is shown in figure 5a, while the growth parameter for the 71% and 100% screens is shown in figure 5b. The initial mixing layer region for the 30% screen is quite evident where the growth parameter is constant. Clearly, the 56% screen grows much faster than the 30% screen. Although initially there is some nonmonotonous variation in the 71% data, from the last three points it is clear that the wake

spreading rate is fastest for this case.

In order to gain some insight to the transition process from shedding to non-shedding wakes, we tried to determine the exact solidity where shedding starts to occur. In our efforts we determined that the transition occurs somewhere between 64% – 67% solidity. Our next goal was to determine whether this transition is sudden or smooth. For this purpose, smoke photographs of the flow field generated by the identical generator was taken repeatedly. Figure 6 shows photos of the 67% screen-wake at a free stream velocity of 5 m/s taken at various instances of time. The flow is dominated by von Karman type vortices. Different photos show similar flow structure where the wavelength of these vortices are constant from one realization to the next. A typical power spectrum of the streamwise velocity fluctuations recorded by a hot-wire in this wake show a sharp peak at the shedding frequency (figure 7). Short-time power spectra have also indicated that the shedding frequency does not change with time. Figure 8 shows photos of the 64% screen-wake. Clearly there is no von Karman vortex shedding originating from the body. Organized structures seem to appear in patches at various streamwise locations. The wavelengths of these structures are slightly different in each photo. A typical power spectrum of the streamwise velocity fluctuations recorded by a hot-wire in this wake shows a broad band peak (figure 9). Our initial attempts to analyse the short-time spectra has indicated that not only these structures appear in patches, their frequency vary with time as hinted by the photos. This analysis however showed the shortcomings of the Fourier Transform as the results were extremely difficult to interpret.

The spectral peaks for the screens are presented in figure 10. The Strouhal number,  $St_\theta = f\theta/U_\infty$  for the nonshedding screens are shown in figure 10a versus  $x/\theta$ . Notice that the  $St_\theta$  decreases with downstream distance, which is the signature of convective instability.  $St_\theta$  for the shedding screens is shown in figure 10b. In this case the shedding frequency and the free stream velocities are constant in each case, thus the streamwise variation of  $St_\theta$  is entirely due to uncertainties in the estimation of the momentum thickness. Indeed when the Strouhal number based on the screen width  $W$ ,  $St_W = fW/U_\infty$ , is plotted we see that it remains constant in  $x$  (see figure 10c.)

In conclusion, several important questions regarding these wake flows remain unanswered. Recently, it has been postulated that (Huerre and Monkewitz 1990) the two distinct wake behaviors can be explained via two different classes of stability, namely *absolute* and *convective*. The vortex shedding phenomenon is believed to be the result of an absolute instability originating near the wake generator and causing the wake behave like a self-sustained oscillator. By contrast, the non-shedding wakes are convectively unstable and are characterized by the absence of a single sustained frequency.

The relationship between the near and far fields generated by shedding and non-shedding wake generators need to be studied in some detail. In order to study the details of the transition from a non-shedding to shedding wake, the transient signature of the transition has to be recorded. This can be made possible by looking at the wake of two low solidity screens placed one after another. If the meshes are aligned, the composite solidity will be low and there won't be any shedding. If the meshes are staggered the solidity will increase and shedding will occur provided that the composite solidity exceeds the critical value which is estimated to be somewhere between 64% and 67%. The transient signal can be recorded by synchronizing the screen movement with the data acquisition.

The short-time spectral analysis of the intermittent, nearly periodic signals via the Fourier Transform has been observed to be inadequate. Owing to the uncertainty of the duration of the intermittencies the results are often unreliable. In order to overcome this difficulty we propose to apply the Wavelet Transform technique (Farge 1992). The Wavelet Transform is designed to overcome the difficulties encountered by the Fourier Transform and has been successfully implemented in speech analysis and image processing. Application of the Wavelet Transform to turbulent flows is fairly new and is expected to open new avenues in the understanding of turbulence.

### 3. The vorticity probe

#### 3.1. Probe description and calibration procedure

Vorticity, which is defined as the curl of the velocity field is known to be the most important quantity related to the structure of a turbulent flow field. However, since the vorticity involves the gradients of the velocity field, until recently its measurement has been limited to very few simple cases.

Vukoslavčević *et al.* (1991) describe a miniature probe with nine hot-wire sensors which is capable of measuring the velocity and vorticity vectors with a spatial resolution of about six Kolmogorov microscales in a turbulent boundary layer.

The orientation of the sensors and the calibration procedure was believed to hinder the performance of the Vukoslavčević probe. Hence, a new circular design and calibration technique was developed by Marasli (1991). This new probe was designed to measure nine unknowns which are the three components of the instantaneous velocity vector  $\mathbf{u} = (u, v, w)$  and the six instantaneous velocity gradients  $\partial u/\partial y$ ,  $\partial u/\partial z$ ,  $\partial v/\partial y$ ,  $\partial v/\partial z$ ,  $\partial w/\partial y$  and  $\partial w/\partial z$ . The gradients in the streamwise direction are then obtained via Taylor's hypothesis (Piomelli *et al.* 1989), thus enabling the estimation of all three components of the instantaneous vorticity vector. The response equations obtained from the nine sensors would provide the

information required the solve for the nine unknowns. The testing of this newly circular probe showed the basic weakness of any nine-sensor probe: since the hot-wire response equations are nonlinear, the solution of a  $9 \times 9$  system is not unique. Which means that for a given set of anemometer voltages, there correspond more than one solution, which is not acceptable physically. Extra information is needed to resolve the nonuniqueness.

A yet newer probe which consists of twelve sensors was developed. The twelve sensors provide twelve equations to solve for nine unknowns. The redundant information is used to resolve the nonuniqueness problem. The sketch of the new probe is shown in figure 11. The twelve sensors are arranged in three arrays each consisting of four wires. The centers of the arrays are located at the corners of an equilateral triangle which measures 1.32 mm on each side. The prongs on which the wires are welded are separated by 0.44 mm. The 24 tungsten prongs are tapered down to  $30 \mu$  diameter at the tip. The sensors are also made of tungsten and are  $2.5 \mu$  in diameter.

The quality of any hot-wire measurement technique starts with the quality of the calibration. Regardless of the technique used, the calibration of hot-wire probes deteriorate with time due to various reasons such as temperature variations, drift in electronics, impurities in the flow, etc. Therefore, speedy calibration and measurement are essential. The technique described here enables the calibration of a multi-sensor probe (non-zero pitch-yaw combinations included) in less than 5 minutes with a computer controlled traversing mechanism. The short duration of calibration period directly translates to improved measurement quality. Following Marasli and Nguyen (1991), we start with the effective cooling velocity which is given by Jorgensen's (1971) response equation:

$$U_{eff}^2 = u_N^2 + k^2 u_T^2 + h^2 u_B^2 \quad (3)$$

where  $u_N^2$ ,  $u_T^2$  and  $u_B^2$  are the normal, tangential and binormal components of the velocity with respect to the sensor (see figure 11b) and  $k$  and  $h$  are the tangential and binormal cooling coefficients respectively. A fourth order polynomial is used to relate the effective cooling velocity to the anemometer bridge voltage in the following form:

$$U_{eff}^2 = P(E) = A_0 + A_1 E + A_2 E^2 + A_3 E^3 + A_4 E^4. \quad (4)$$

For a slanted, inclined wire

$$u_N = n_1 u + n_2 v + n_3 w, \quad (5)$$

$$u_T = t_1 u + t_2 v + t_3 w, \quad (6)$$

$$u_B = b_1 u + b_2 v + b_3 w, \quad (7)$$

where  $n_i$ ,  $t_i$  and  $b_i$  ( $i = 1-3$ ) are known coefficients that depend on the orientation of the wire. Substitution of (5-7) into (4) yields:

$$U_{eff}^2 = A_1 u^2 + A_2 v^2 + A_3 w^2 + A_4 uv + A_5 uw + A_6 vw = P(E) \quad (8)$$

For each of the twelve sensors in the probe we end up with an equation such as (8). Since we have nine unknowns, (three velocity components and six gradients,) the twelve equations provide extra information which can be utilized to resolve the nonuniqueness problem. We choose to solve the equations in a least-square sense, which provides unique solutions within the calibration domain. For convenience we write (8) as

$$u_j^2 = P_j(E_j) + K_1 v_j^2 + K_2 w_j^2 + K_3 u_j v_j + K_4 u_j w_j + K_5 v_j w_j \quad (9)$$

for  $j = 1-12$  sensors. Notice that we have lumped the known coefficients  $n_i$ ,  $t_i$  and  $b_i$  into the unknown calibration coefficients  $K_{ij}$  to be determined during calibration. Thus errors due to uncertainties in the slant and roll angles are eliminated, which is one major advantage of this calibration procedure. When a multi-sensor probe is used in a non-uniform flow, the velocity vector seen by each sensor will be different. Following Vukoslavčević *et al.* (1991) we expand the velocity measured by each sensor in a Taylor series around the centroid of the probe. Hence we let

$$u_j = u + c_j \frac{\partial u}{\partial y} + d_j \frac{\partial u}{\partial z} + \dots \quad (10)$$

$$v_j = v + c_j \frac{\partial v}{\partial y} + d_j \frac{\partial v}{\partial z} + \dots \quad (11)$$

$$w_j = w + c_j \frac{\partial w}{\partial y} + d_j \frac{\partial w}{\partial z} + \dots \quad (12)$$

where the right-hand-side is evaluated at the probe centroid. The constants  $c_j$  and  $d_j$  are the vertical and horizontal distances from the centroid of each wire to the centroid of the probe respectively. Substitution of (10-12) into (9) yields 12 nonlinear algebraic equations with the 9 unknowns.

$$u, v, w, \frac{\partial u}{\partial y}, \frac{\partial u}{\partial z}, \frac{\partial v}{\partial y}, \frac{\partial v}{\partial z}, \frac{\partial w}{\partial y} \text{ and } \frac{\partial w}{\partial z} \quad (13)$$

evaluated at the centroid of the probe, which can be solved in a least-square sense using

standard numerical techniques such as Newton's method. The nonlinear equations are:

$$f_j(u, v, w, \frac{\partial u}{\partial y}, \frac{\partial u}{\partial z}, \frac{\partial v}{\partial y}, \frac{\partial v}{\partial z}, \frac{\partial w}{\partial y}, \frac{\partial w}{\partial z}, P_j, c_j, d_j) = 0 \quad (14)$$

where

$$P_j = A_{0j} + A_{1j}E_j + A_{2j}E_j^2 + A_{3j}E_j^3 + A_{4j}E_j^4 \quad (15)$$

and

$$\begin{aligned} f_j = & -P_j + u^2 + 2c_j u \frac{\partial u}{\partial y} + 2d_j u \frac{\partial u}{\partial z} \\ & -K_{1j} \left[ v^2 + 2c_j v \frac{\partial v}{\partial y} + 2d_j v \frac{\partial v}{\partial z} \right] \\ & -K_{2j} \left[ w^2 + 2c_j w \frac{\partial w}{\partial y} + 2d_j w \frac{\partial w}{\partial z} \right] \\ & -K_{3j} \left[ uv + c_j \left( u \frac{\partial v}{\partial y} + v \frac{\partial u}{\partial y} \right) + d_j \left( u \frac{\partial v}{\partial z} + v \frac{\partial u}{\partial z} \right) \right] \\ & -K_{4j} \left[ uw + c_j \left( u \frac{\partial w}{\partial y} + w \frac{\partial u}{\partial y} \right) + d_j \left( u \frac{\partial w}{\partial z} + w \frac{\partial u}{\partial z} \right) \right] \\ & -K_{5j} \left[ vw + c_j \left( v \frac{\partial w}{\partial y} + w \frac{\partial v}{\partial y} \right) + d_j \left( v \frac{\partial w}{\partial z} + w \frac{\partial v}{\partial z} \right) \right]. \end{aligned} \quad (17)$$

The unknown constants  $A_{ij}$  and  $K_{ij}$  are obtained during calibration by subjecting the probe to uniform flow ( $Q$ ) coming at various pitch ( $\alpha$ ) and yaw ( $\beta$ ) angles. The calibration velocity components ( $u, v, w$ ) are then given by  $u = Q \cos \alpha \cos \beta$ ,  $v = Q \sin \alpha \cos \beta$  and  $w = Q \sin \beta$ . For calibration the probe is mounted on the traversing mechanism of a calibration jet which keeps the sensing volume of the probe at the same location as the pitch and yaw angles are varied. Typically, a combination of 3 yaw and 3 pitch angles are used between  $\pm 20^\circ$  at two different speeds, thus giving a total of 18 calibration points. A typical calibration curve for one sensor is shown in figure 12 where the calibration data points (indicated by symbols) are plotted versus the bridge voltage. For the symbols, the ordinate is  $U_{eff}^2$ , where the velocity vector  $u$  is known from the pitch and yaw angles, and the constants  $K_i$  have been obtained during calibration. The solid curve is a fourth order polynomial fit which describes the relationship between the effective cooling velocity and the bridge voltage. The fact that all points collapse on one curve is an indication that the assumed cooling law is satisfactory. Figure 12 displays the calibration curve for one sensor only. All twelve sensors of the probe exhibit similar calibration properties. The quality of the calibration can be checked by trying to recover the velocities used in the process. In addition, since the probe

is calibrated in a uniform flow, there should be no gradients in the calibration data. A good calibration is one which recovers the velocities within 1% and gives spurious vorticities that are less than  $20 \text{ sec}^{-1}$ . The sample data shown here fall in that category.

Note that the present calibration scheme can easily be applied to probes with different geometries. The only geometrical information needed is the distance from the center of each wire to the centroid of the frontal sensing area of the probe. The number of sensors need not be fixed at twelve.

### 3.2. Vorticity measurements in the wake of a circular cylinder

The performance of the twelve-sensor vorticity probe was tested in the wake of a 6.35 mm diameter circular cylinder. The probe was placed downstream of the cylinder at the location  $x/d = 30$ . The free stream velocity was  $U_\infty = 5 \text{ m/s}$ , resulting in a Reynolds number of 2000 based on the diameter.

The mean velocity profile is shown in figure 13. The ordinate is the vertical coordinate normalized by the half-width of the wake,  $L_0$ , which was 8.5 mm. The abscissa is the velocity deficit normalized by the centerline value  $u_0 = 0.82 \text{ m/s}$ . The momentum thickness,  $\theta$ , which is proportional to the drag of the cylinder was 2.8 mm. In figure 13 the symbols represent the measurements and the solid curve corresponds to an analytical curve fit to the experimental data. The profile is quite symmetric around the centerline as it should be.

The turbulence intensities of the  $u$  (streamwise or  $x$ -direction),  $v$  (cross-stream or  $y$ -direction) and  $w$  (spanwise or  $z$ -direction) velocity components are shown in figure 14. The  $v$  component has the most intense fluctuations, which is due to the von Karman vortex shedding present in the flow. The Reynolds shear stresses are presented in figure 15. Notice that the  $\overline{u'w'}$  and  $\overline{v'w'}$  components are negligible compared to the dominant  $\overline{u'v'}$  component. Ideally  $\overline{u'w'}$  and  $\overline{v'w'}$  should be identically zero.

Figure 16 compares the distribution of the mean velocity gradient  $\partial \overline{U} / \partial y$  measured directly with the twelve-sensor probe with the derivative of the curve fit to the  $\overline{U}$  distribution shown in figure 13. Notice the excellent agreement between the two, which shows the capability of this probe to measure instantaneous velocity gradients accurately, which is essential for vorticity measurements.

The mean vorticity components are shown in figure 17. Notice that  $\overline{\Omega_z}$  component is the dominant one which results from the mean velocity gradient in the cross-stream direction. The  $\overline{\Omega_x}$  and  $\overline{\Omega_y}$  components should ideally be zero. The extremely small nonzero components recorded is an overall indication of the lack of spanwise uniformity in the flow and the ability of the probe to resolve the gradients. The variance of the vorticity fluctuations are shown in

figure 18. Unlike the mean vorticity, all three components of the vorticity fluctuations are of the same order of magnitude, which is a property of turbulence in general.

The power spectra of the velocity fluctuations at three different cross-stream locations are shown in figure 19. The sharp peak in the spectra corresponds to the von Karman vortex shedding, which occurs at 160 Hz or Strouhal number,  $St = fd/U_\infty = 0.2$ . Notice that the shedding is most evident in the  $v$ -spectra and nonexistent in the  $w$ -spectra, which is an indication of the nominal two-dimensionality of the flow. The vorticity spectra are shown in figure 20. Again the shedding frequency is visible in the spanwise vorticity component, which corresponds to the two-dimensional nature of the shedding.

In conclusion, we consider these measurements in the circular cylinder wake as a landmark success. To our knowledge, this is the first documentation of the simultaneous measurement of all three components of the velocity and all three components of the vorticity vectors. Efforts toward the usage of this probe in flows where the three dimensional structure is more eminent is underway.

#### 4. Publications resulting from present grant

Funds provided by the present grant were crucial in the continuation of the research projects which resulted in the publication Marasli & Nguyen (1991). We also submitted an abstract to *2nd International Symposium on Engineering Turbulence Modelling and Measurements* to be held on May 31 – June 2, 1993 in Florence, Italy. Mr. Phuc Nguyen is doing his Ph.D. dissertation on the vortical structure of the wake and his dissertation work, upon completion, will be submitted to an archival journal for publication. Mr. John Wright, who is doing his M.S. thesis on the screen wakes, will finish soon and his work will be submitted to an archival journal for publication. The sponsorship of the Engineering Foundation will be gratefully acknowledged in those publications.

#### 5. References

- CASTRO, I. 1971 *J. Fluid Mech.* 46, 599.
- FARGE, M. 1992 "Wavelet transforms and their applications to turbulence," *Annu. Rev. Fluid Mech.*, 24, 395.
- HUERRE, P. & MONKEWITZ, P. A. 1985 *J. Fluid Mech.* 159, 151.
- HUERRE, P. & MONKEWITZ, P. 1992 "Local and global instabilities in spatially developing flows," *Annu. Rev. Fluid Mech.*, 24, 395.
- JORGENSEN, F. E. 1971 *DISA Inform.* 11, 31.
- KARMAN, T. VON 1911 *Gottinger Nachr., math-phys. Kl.*, 509.



- MARASLI, B. 1983 Master's thesis, Dept. of AME, University of Arizona.
- MARASLI, B. 1991 The structure of wakes behind various bluff and non-bluff bodies. Progress Report submitted to Engineering Foundation.
- MARASLI, B. 1989 Ph.D. dissertation, University of Arizona.
- MARASLI, B., CHAMPAGNE, F. & WYGNANSKI, I. 1991 *Phys. Fluids A* **3**, 665.
- MARASLI, B., CHAMPAGNE, F. & WYGNANSKI, I. 1992 *J. Fluid Mech.* **235**, 511.
- MARASLI, B. & NGUYEN, P. 1991 "A calibration technique for multiple-sensor hot-wire probes," *Bull. Am. Phys. Soc.* **36**, 2623.
- MONKEWITZ, P. A. & NGUYEN, L. N. 1987 *J. Fluids Struct.* **1**, 165.
- PIOMELLI, U., BALINT, J.-L. & WALLACE, J. M. 1989 *Phys. Fluids* **32**, 609.
- RAYLEIGH, LORD 1879 *Phil. Mag. ser. 5*, **7**(42), 149.
- ROSHKO, A. 1954 *NACA Rep.* 1191.
- SATO, H. & KURIKI, K. 1961 *J. Fluid Mech.* **11**, 321.
- STROUHAL, V. 1878 *Ann. Phys. Chem.* **5**, 217.
- TOWNSEND, A. A. 1947 *Proc. R. Soc. Lond.* **A190**, 551.
- TOWNSEND, A. A. 1949 *Austral. J. Sci.* **2**, 451.
- TOWNSEND, A. A. 1956 *The Structure of Turbulent Shear Flow*. Cambridge University Press.
- TRANTAFYLLOU, G. S., TRIANTAFYLLOU, M. S. & CHRYSOSTOMIDIS C. 1986 *J. Fluid Mech.* **170**, 461.
- UBEROI, M. S. & FREYMUTH, P. 1969 *Phys. Fluids* **12**, 1359.
- VUKOSLAVČEVIĆ, P., WALLACE, J. M. & BALINT, J.-L. 1991 *J. Fluid Mech.* **228**, 25.
- WALLACE, J. M. 1983 *Bull. Am. Phys. Soc.* **28**, 1401.
- WYGNANSKI, I. J., CHAMPAGNE, F. H. & MARASLI, B. 1986 *J. Fluid Mech.* **168**, 31.
- YAMADA, H., KAWATA, Y., OSAKA, H. & KAGEYAMA, Y. 1980 Tech. Rep. Yamaguchi University, Japan, **2**(4).

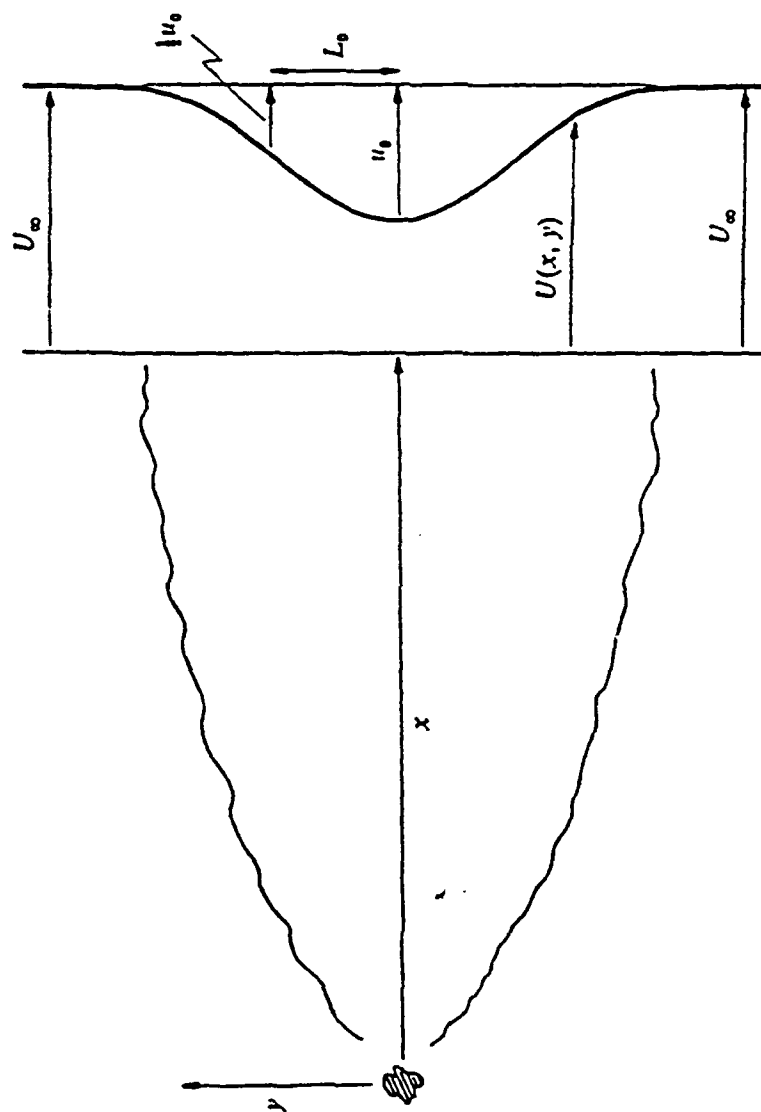


FIGURE 1. A sketch defining the nomenclature.

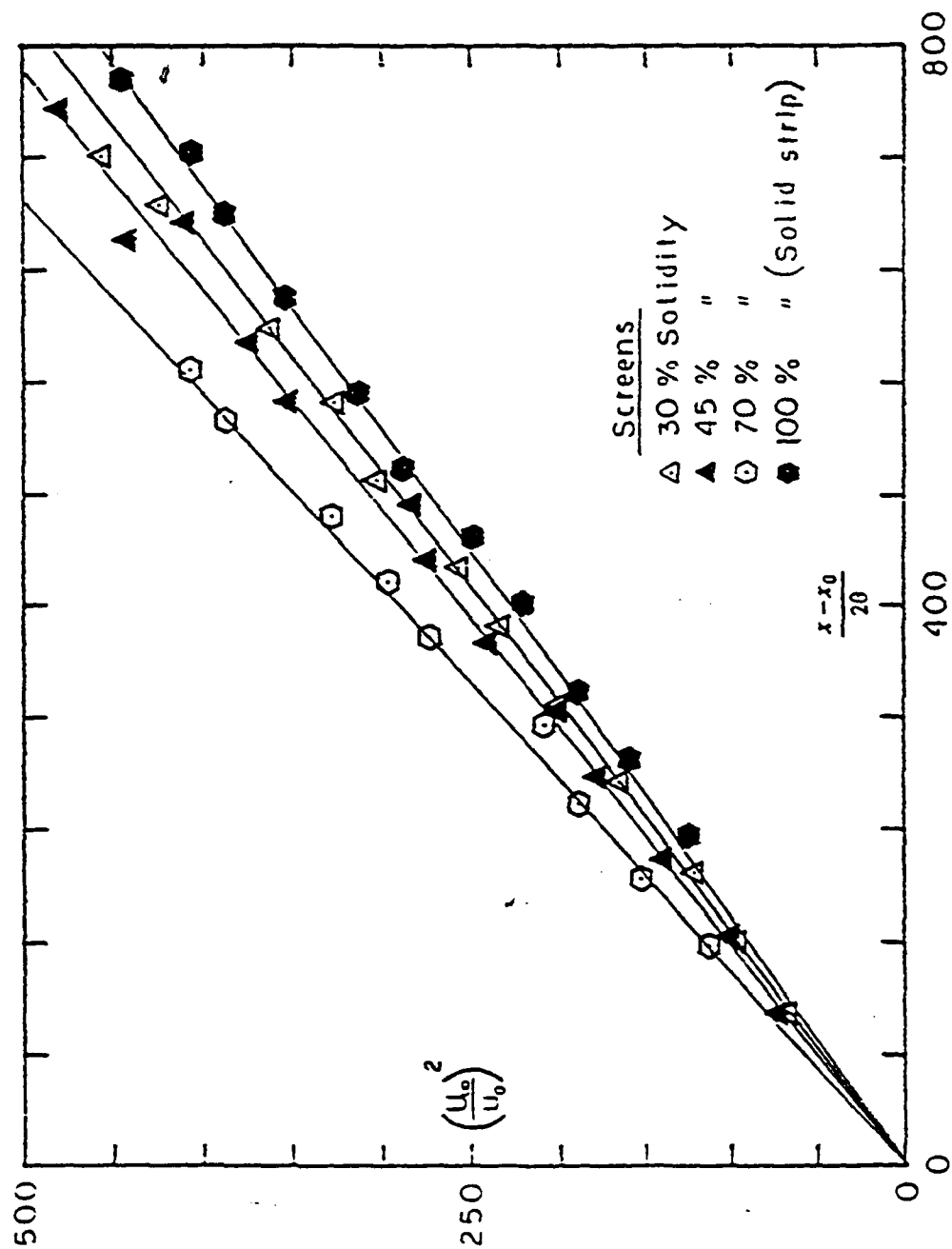


Figure 2. The streamwise evolution of  $\left[\frac{u}{u_0}\right]^2$  for various screens.

△ 30 % Solidity screen  
 ▲ 45 %       "  
 ⊕ 70 %       "  
 ◆ 100 %       " (Solid strip)

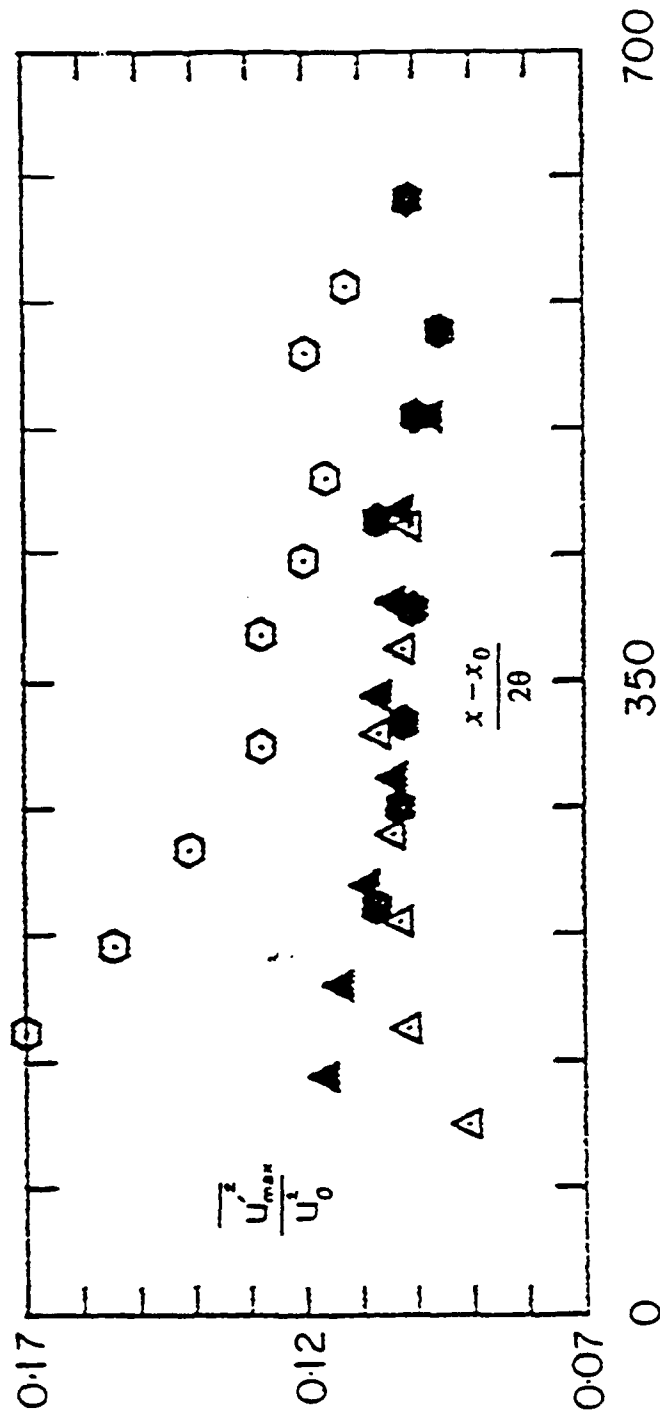


Figure 3. The maximum turbulence intensities versus the streamwise coordinate for the screens.

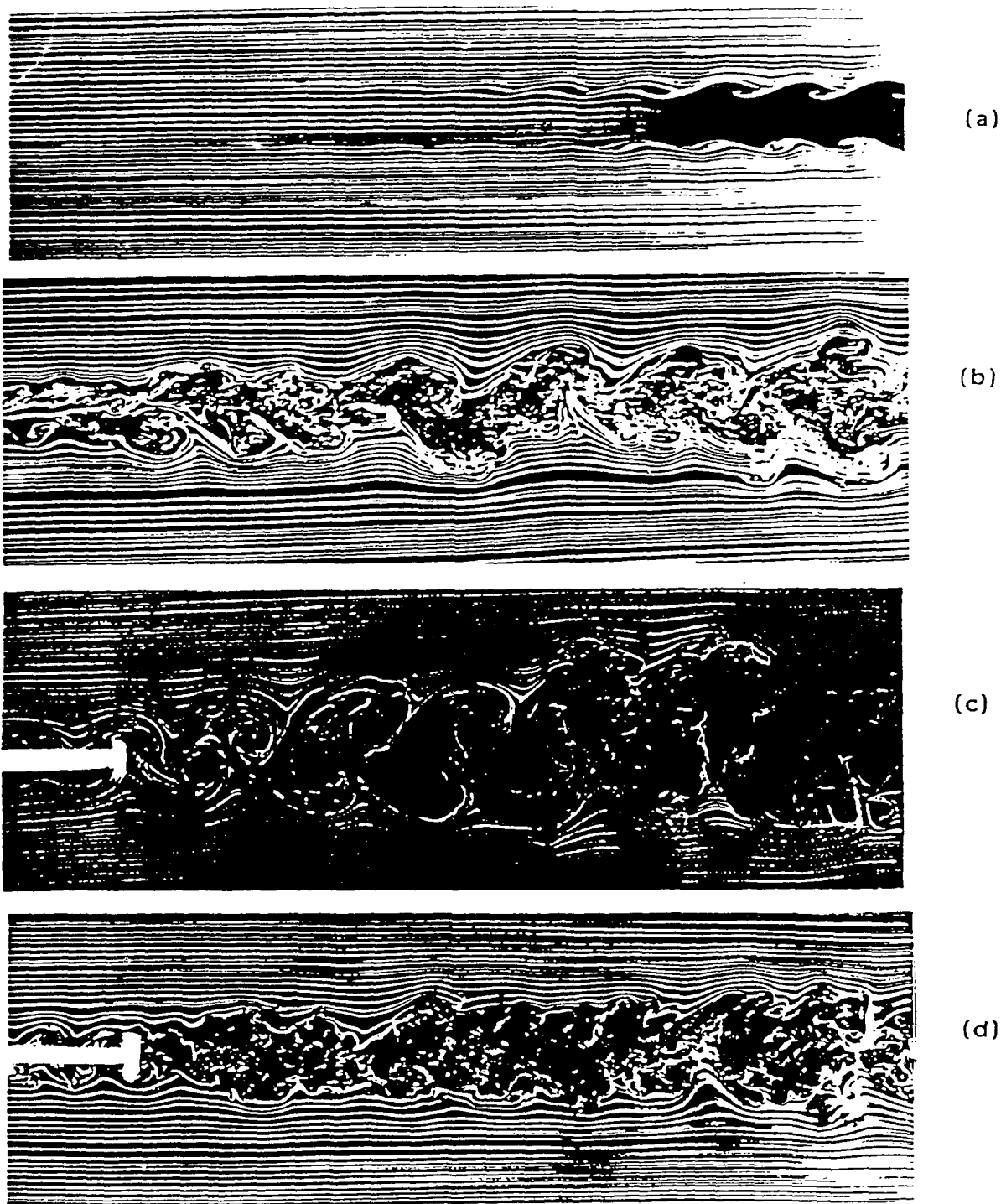


Figure 4. Smoke photographs behind wakes of screens with various solidities: (a) 30% solidity; (b) 50%; (c) 70%; (d) 100%.

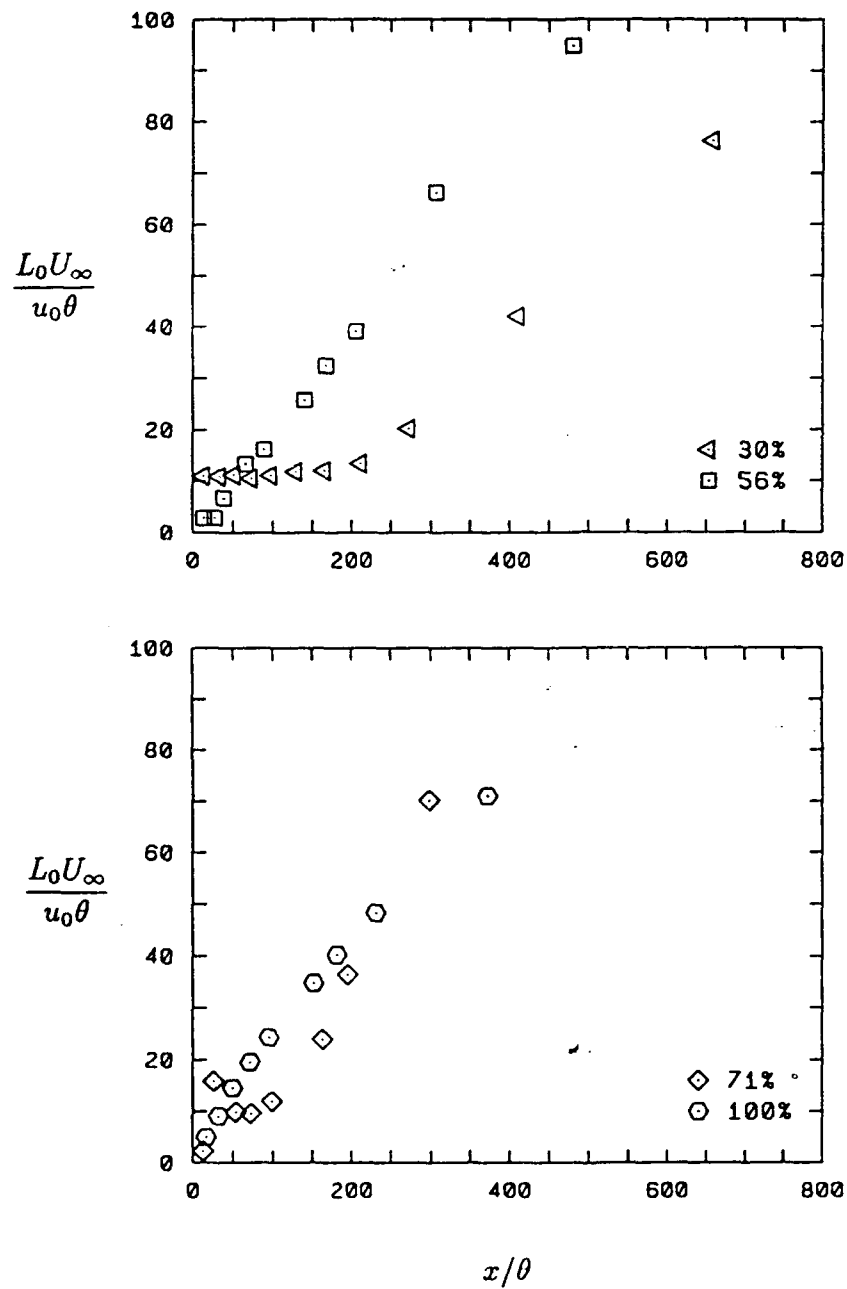


FIGURE 5. Variation of the mean flow growth parameter with streamwise distance for the screen wakes.

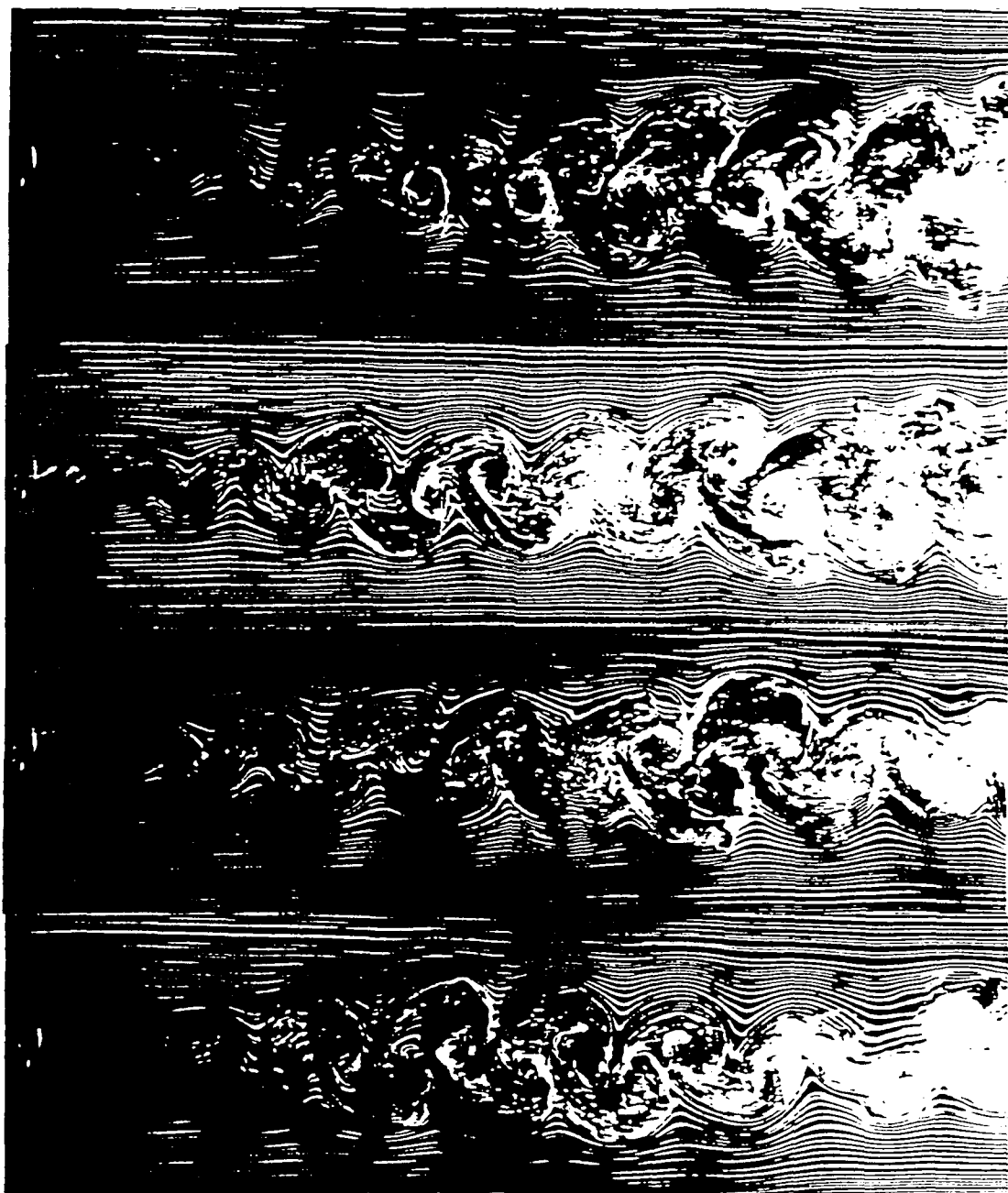


Figure 7. Smoke photographs behind the wake of 67% solidity screen.  
Each photo corresponds to a different instant of time.

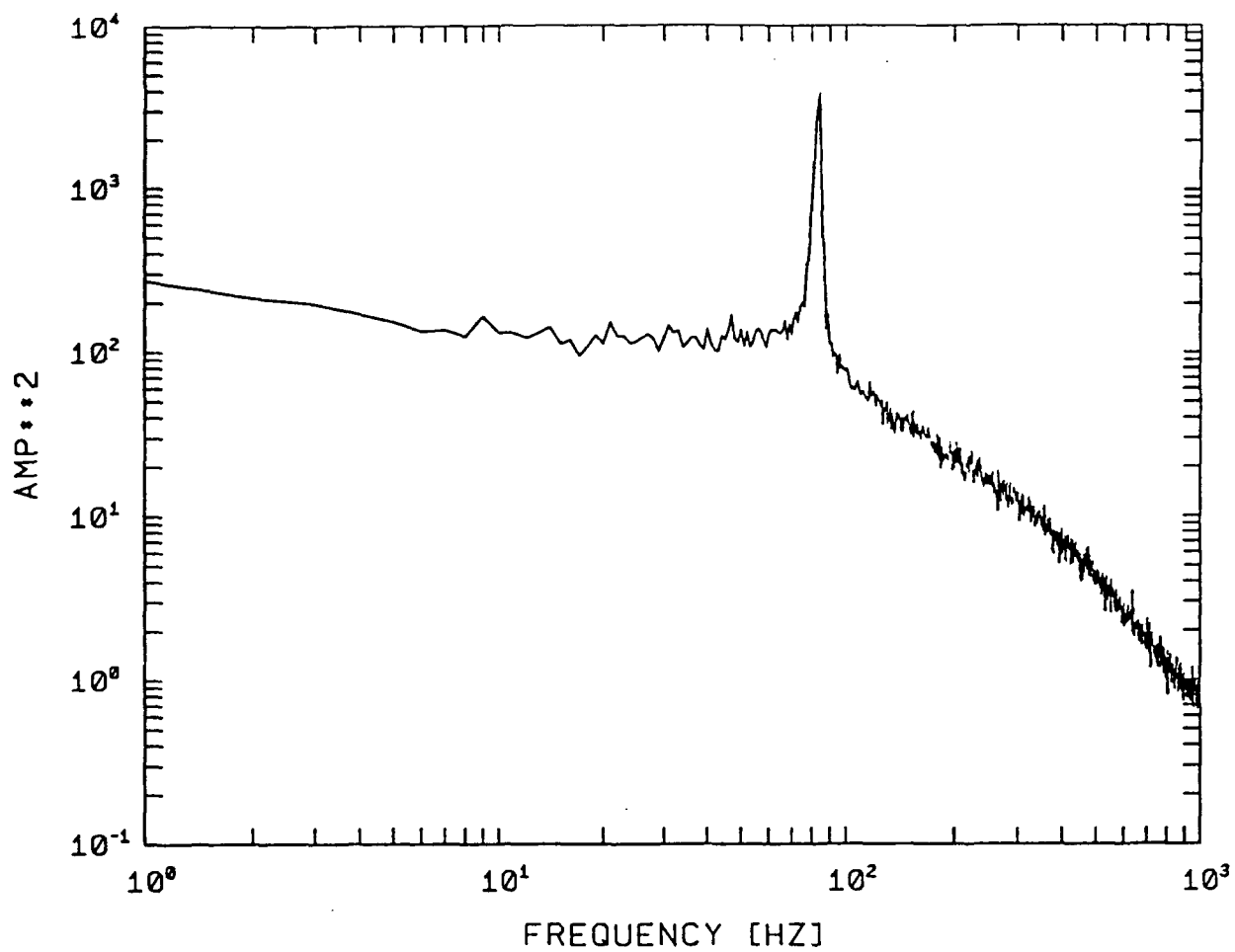


FIGURE 7. Power spectrum in the wake of 67% solidity screen. The sharp peak corresponds to von Karman shedding frequency.



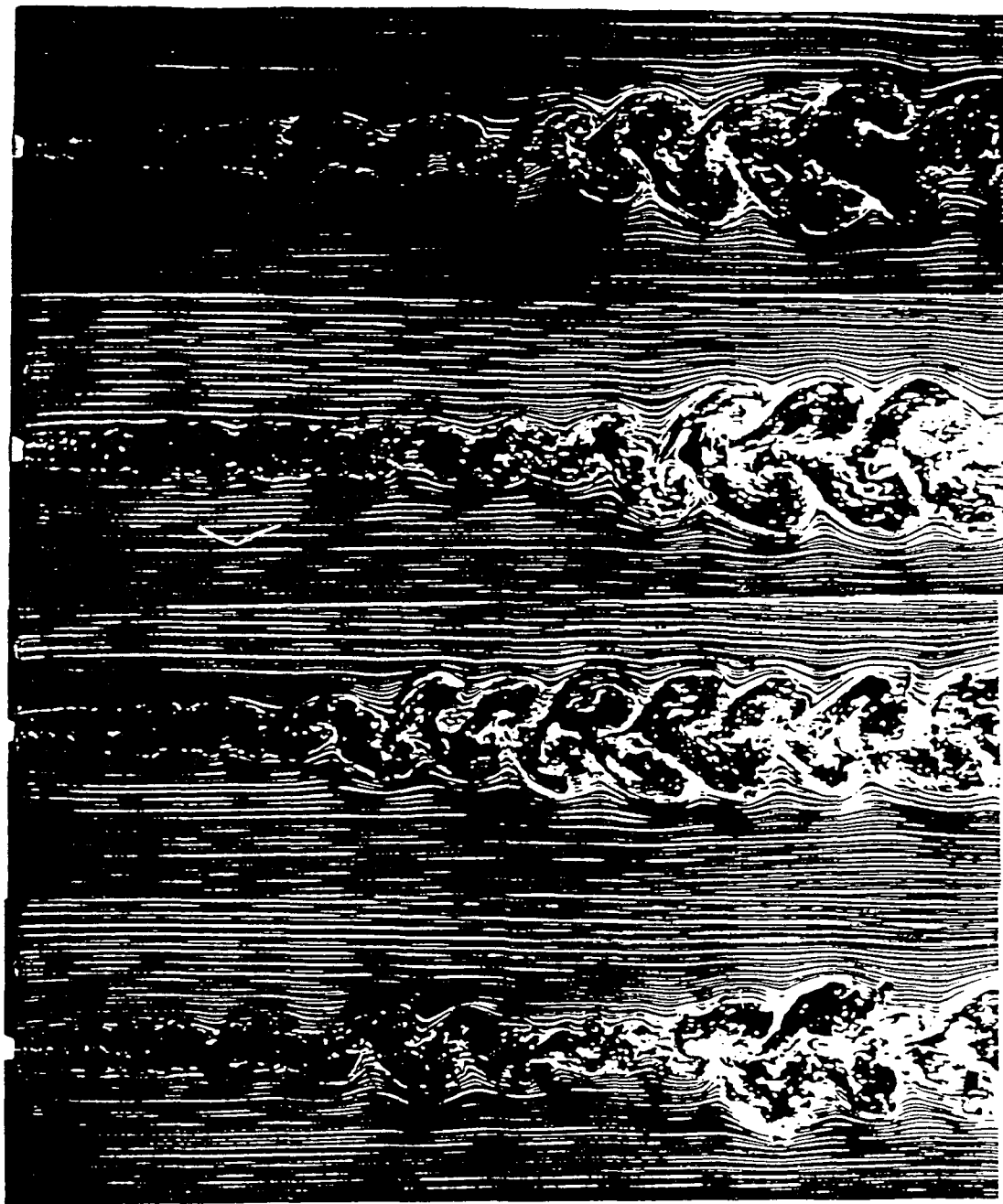


Figure 3. Smoke photographs behind the wake of 64% solidity screen.  
Each photo corresponds to a different instant in time.

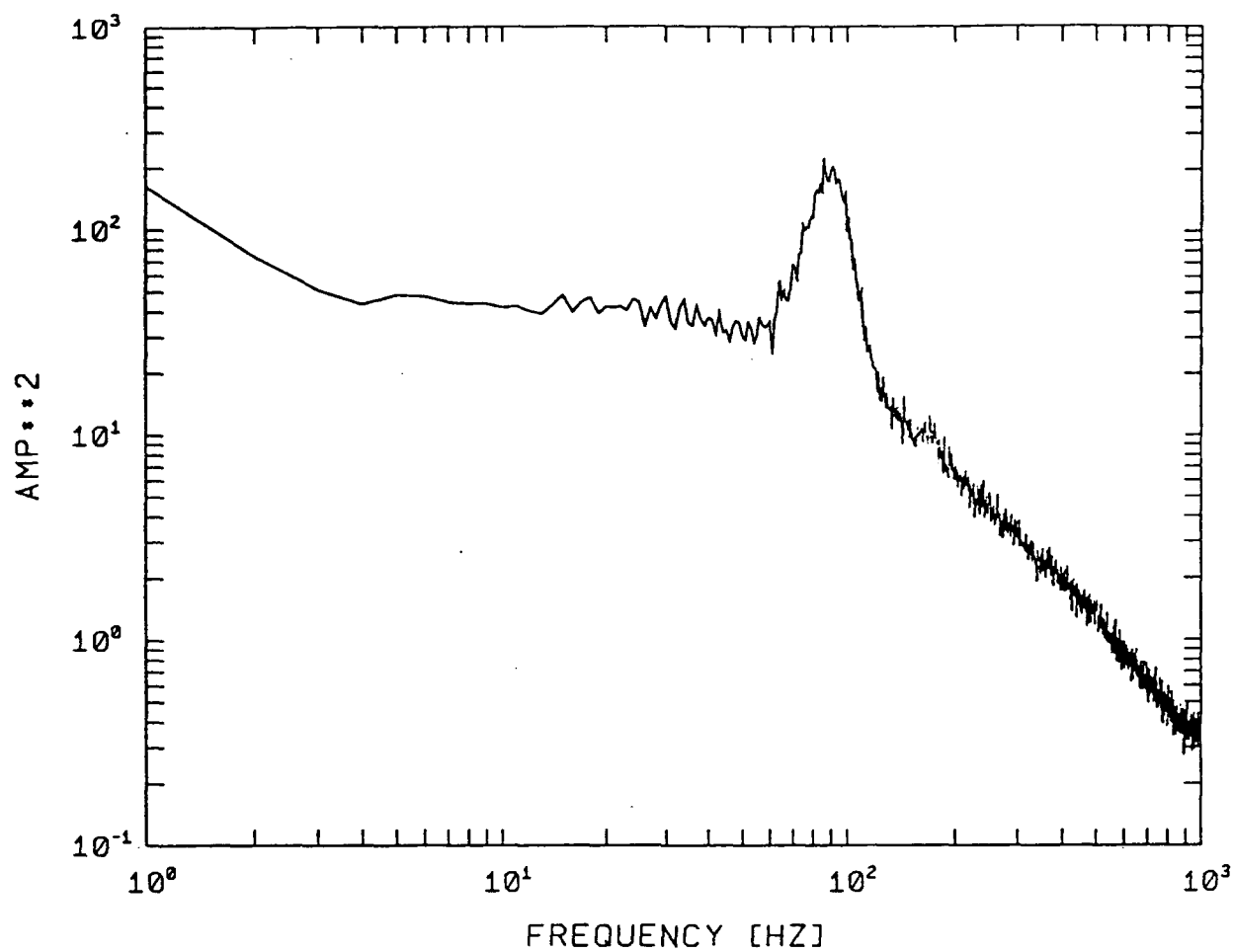


FIGURE 9. Power spectrum in the wake of 64% solidity screen. The broad-band peak corresponds to the range of frequencies of the intermittent structures.

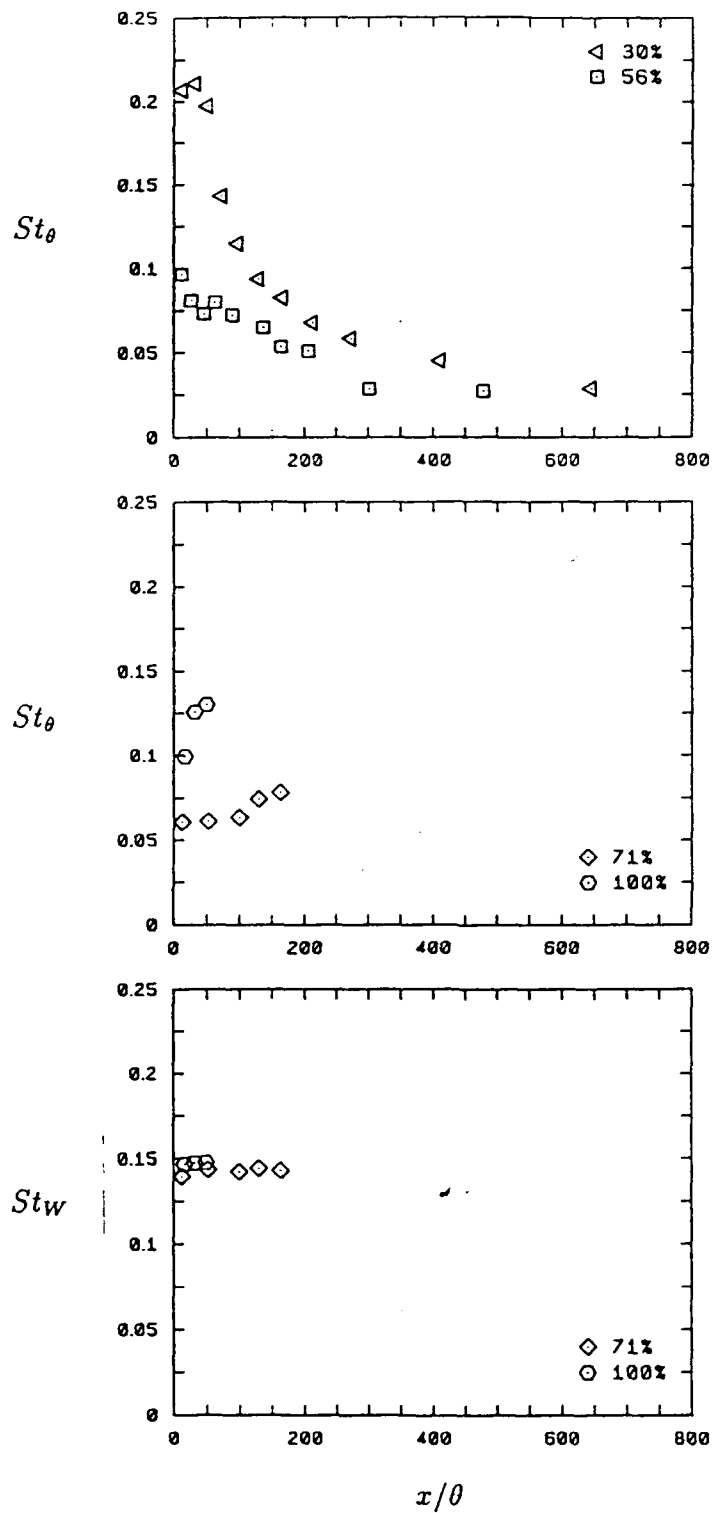


FIGURE 10. Variation of the Strouhal number with streamwise distance for the screen wakes.

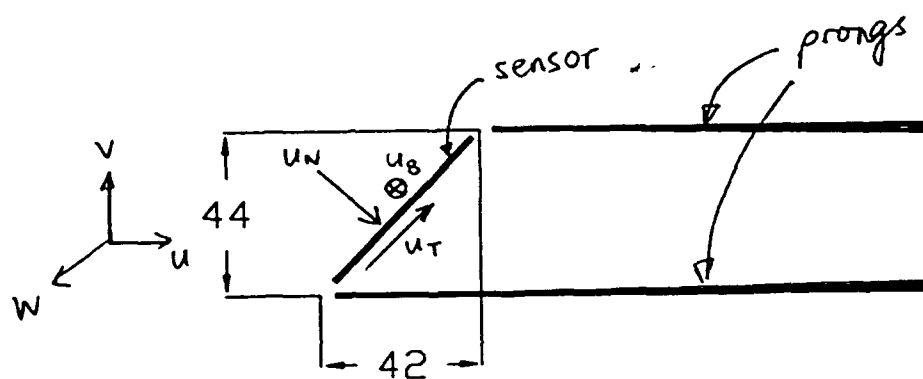
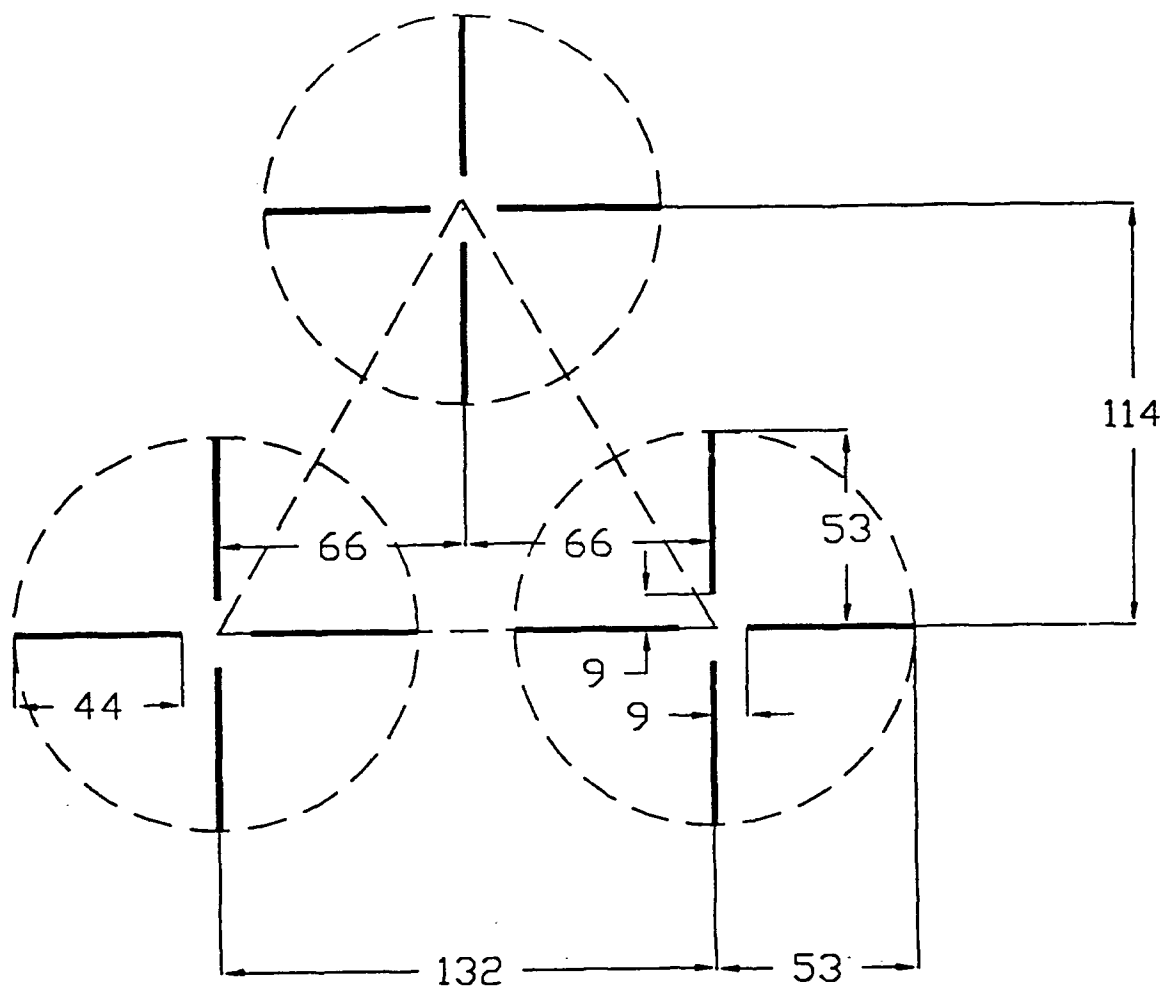


FIGURE 11. Sketch of the twelve-sensor vorticity probe. (a) Front view; (b) side view of one sensor. All dimensions are in 1/100 mm.

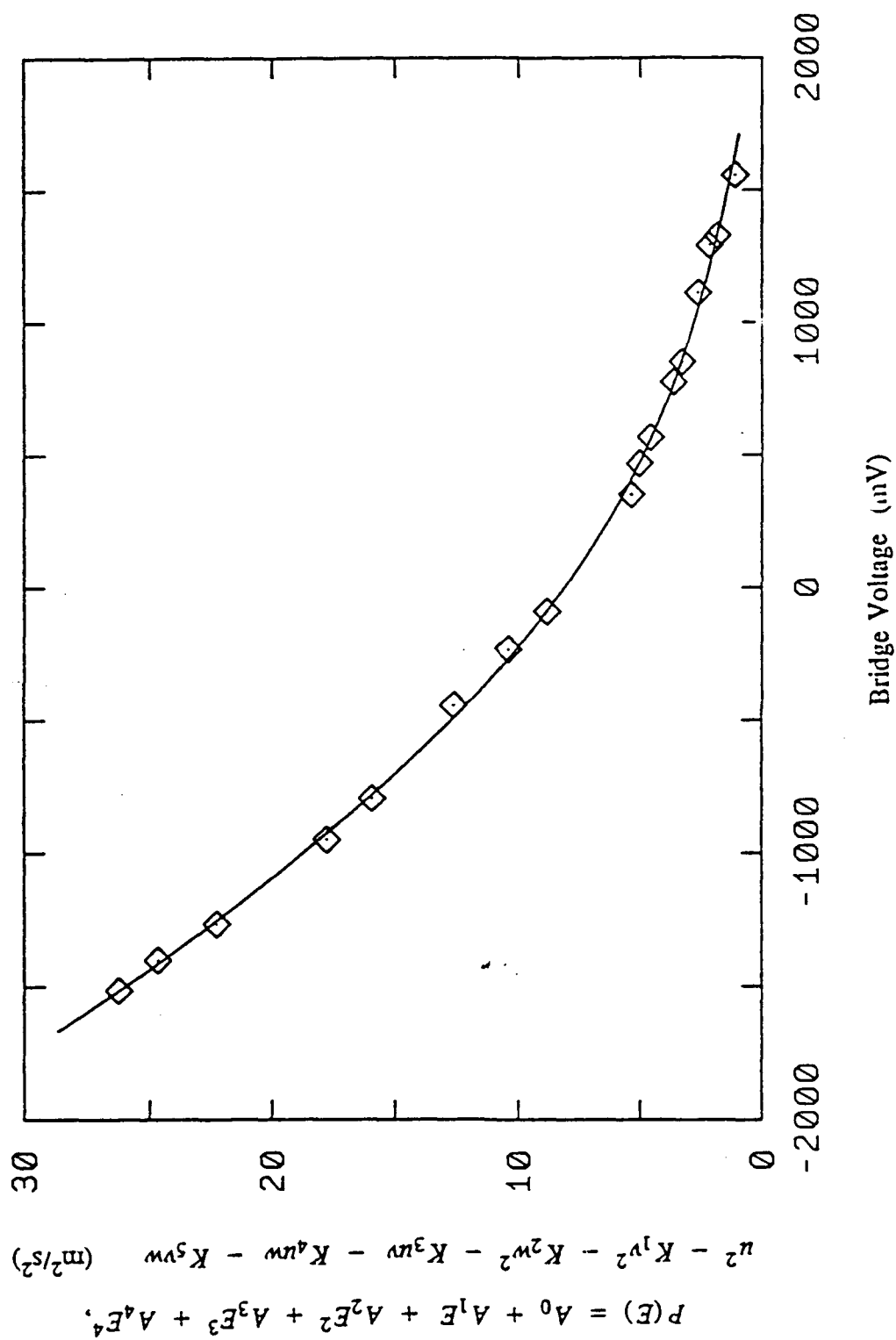


Figure 12 Typical calibration data for one sensor of the vorticity probe. The symbols represent the measured data while the solid curve corresponds to the polynomial fit.

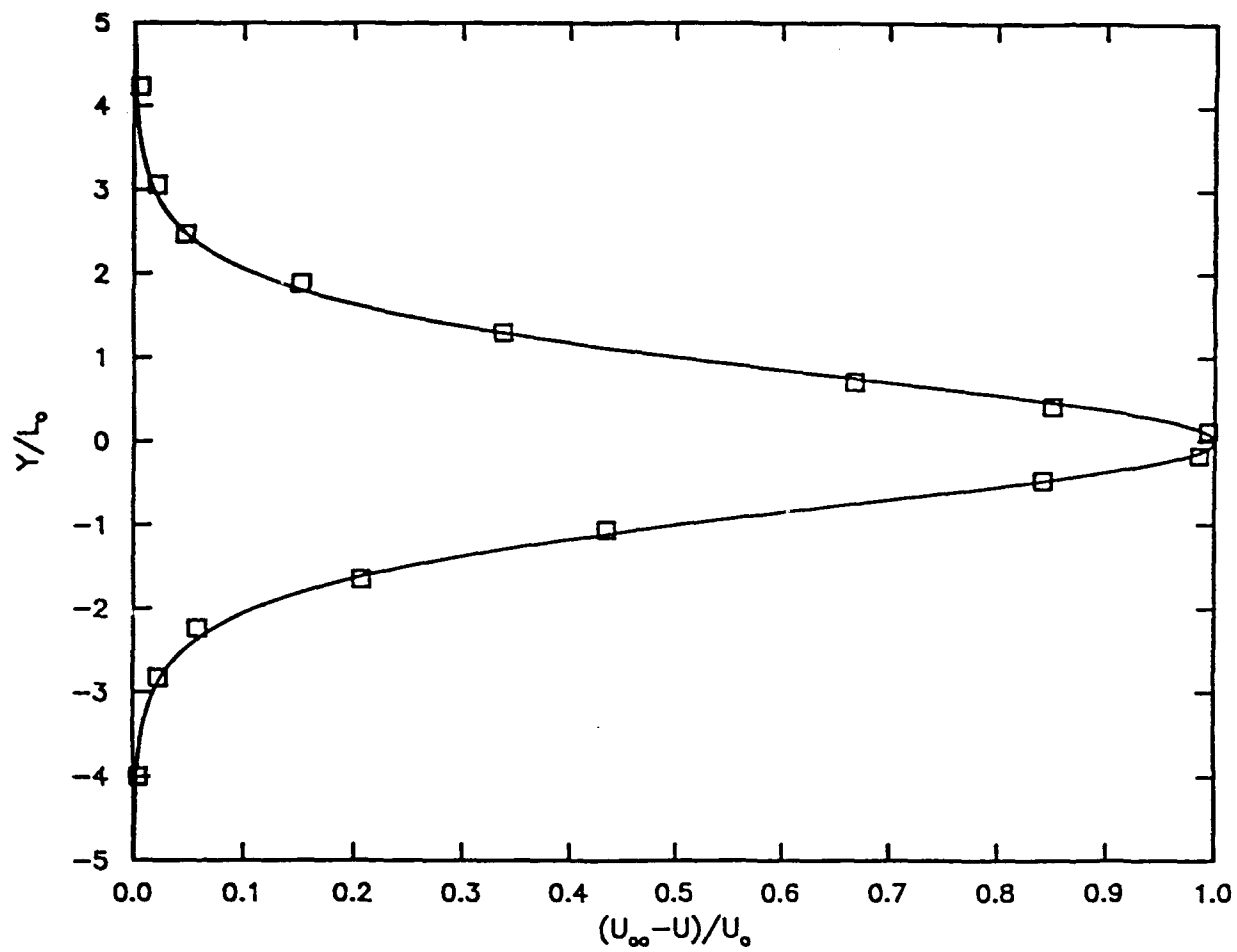


FIGURE 13. Mean velocity profile measured by the vorticity probe in the circular cylinder wake.

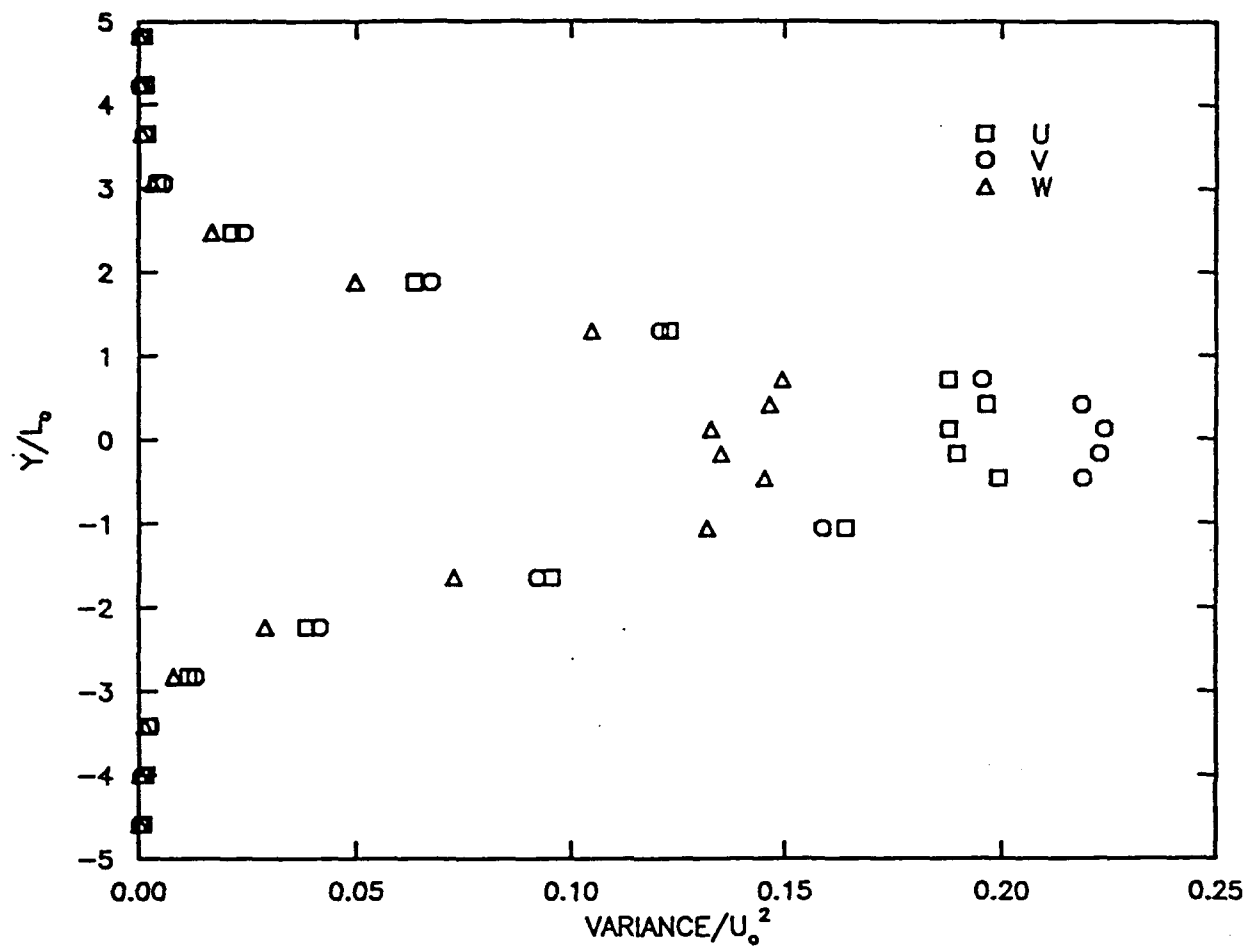


FIGURE 14. Turbulence intensities measured by the vorticity probe in the circular cylinder wake.

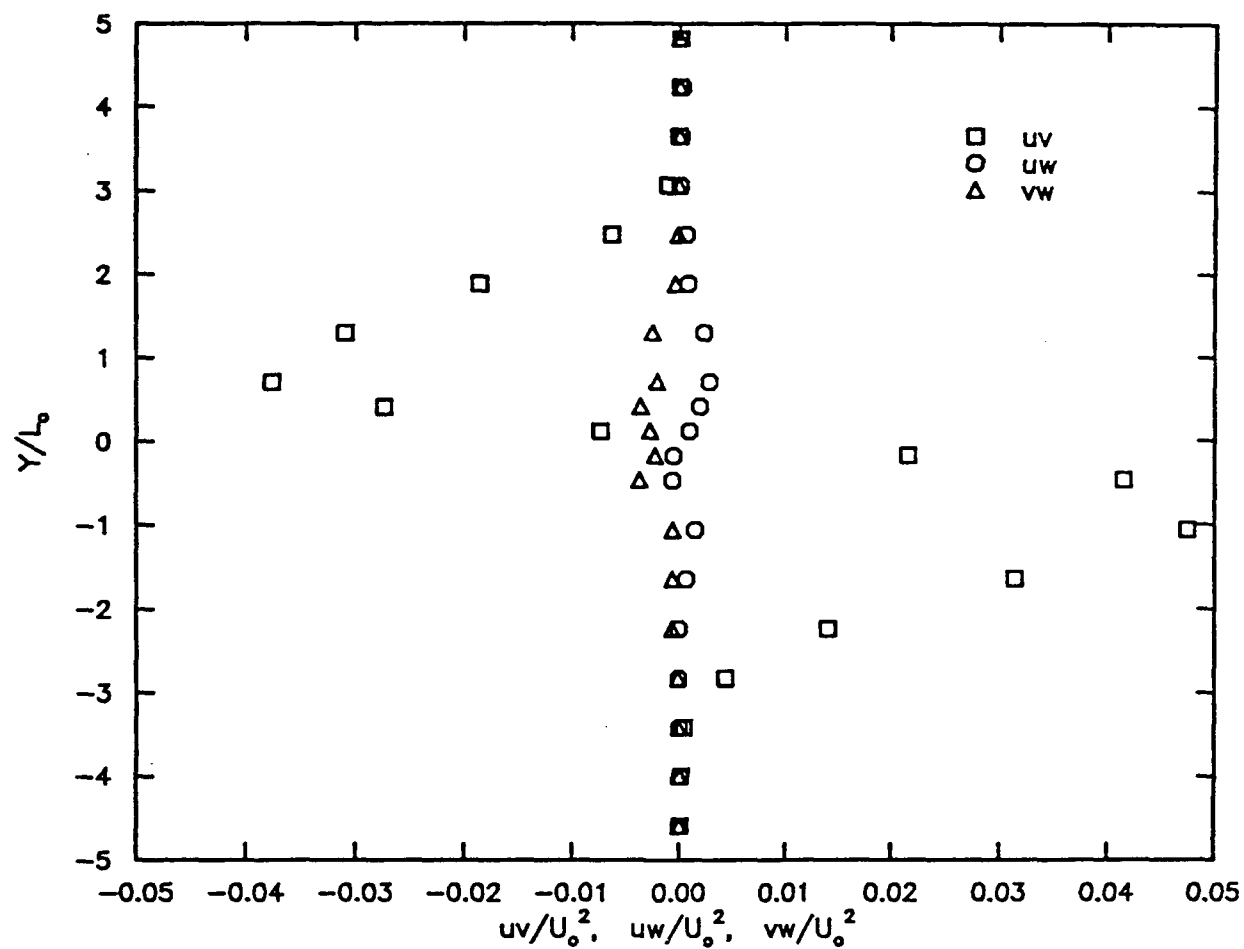


FIGURE 15. Reynolds shear stress profiles measured by the vorticity probe in the circular cylinder wake.



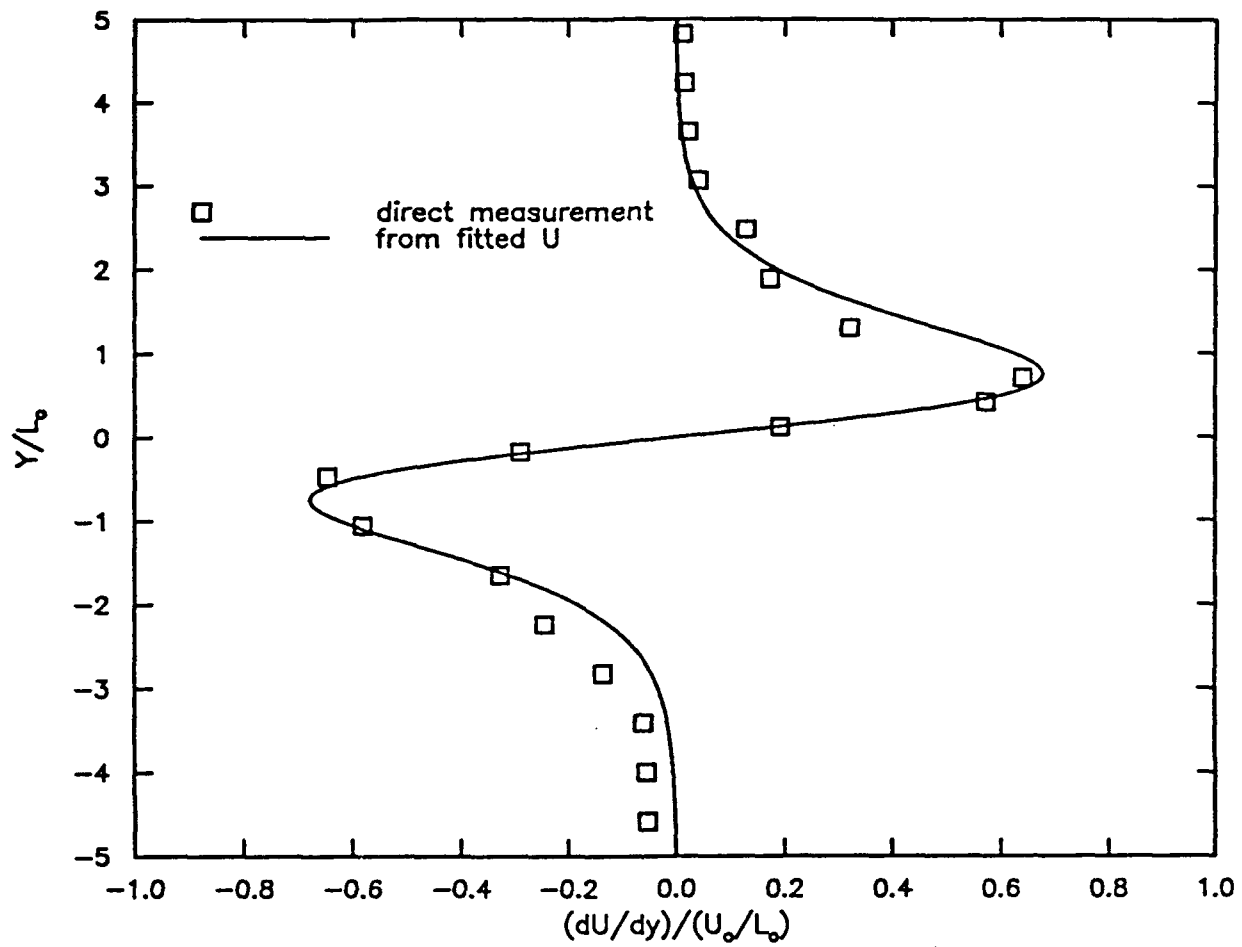


FIGURE 16. Mean flow gradient measured by the vorticity probe in the circular cylinder wake.

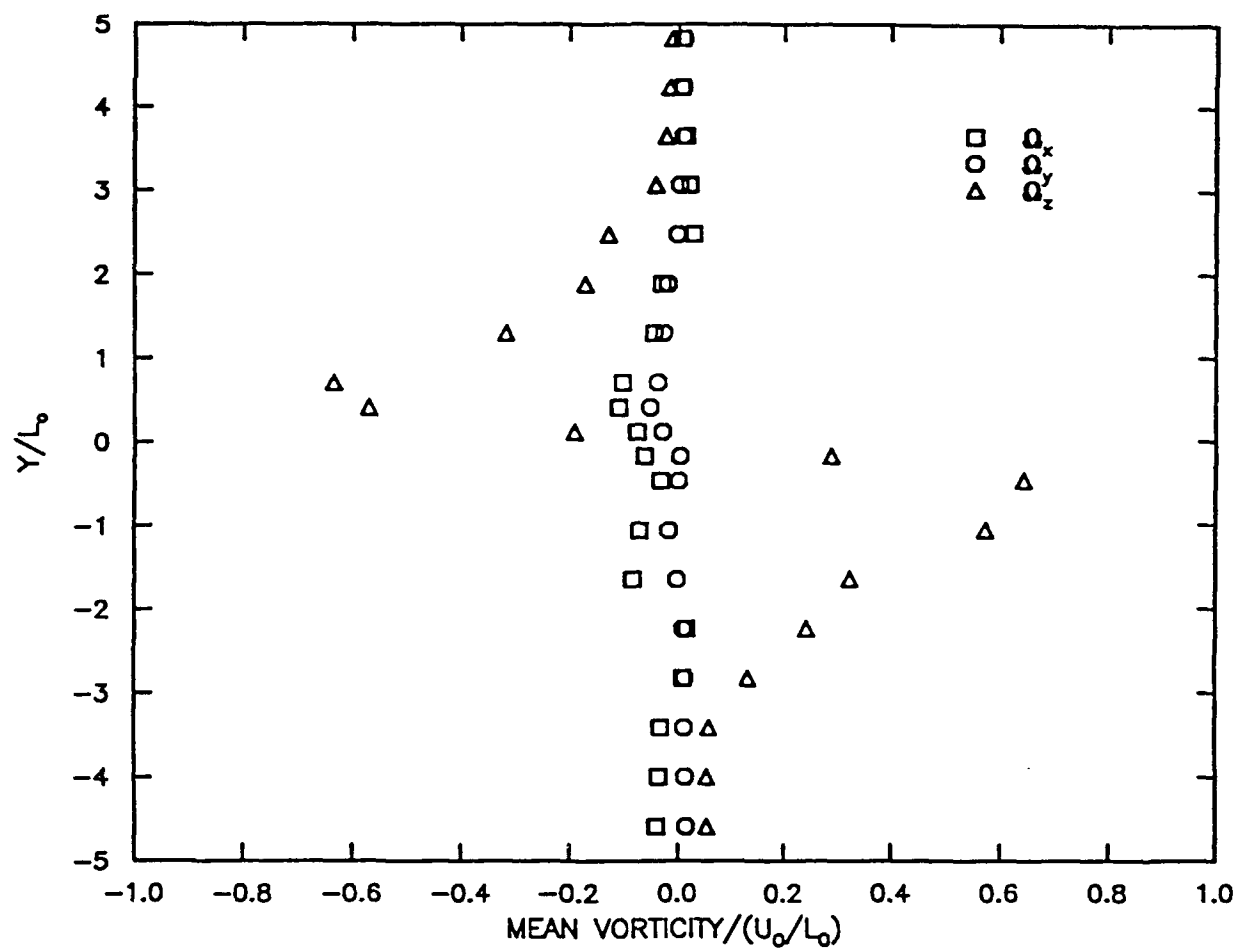


FIGURE 17. Mean vorticity profiles measured by the vorticity probe in the circular cylinder wake.

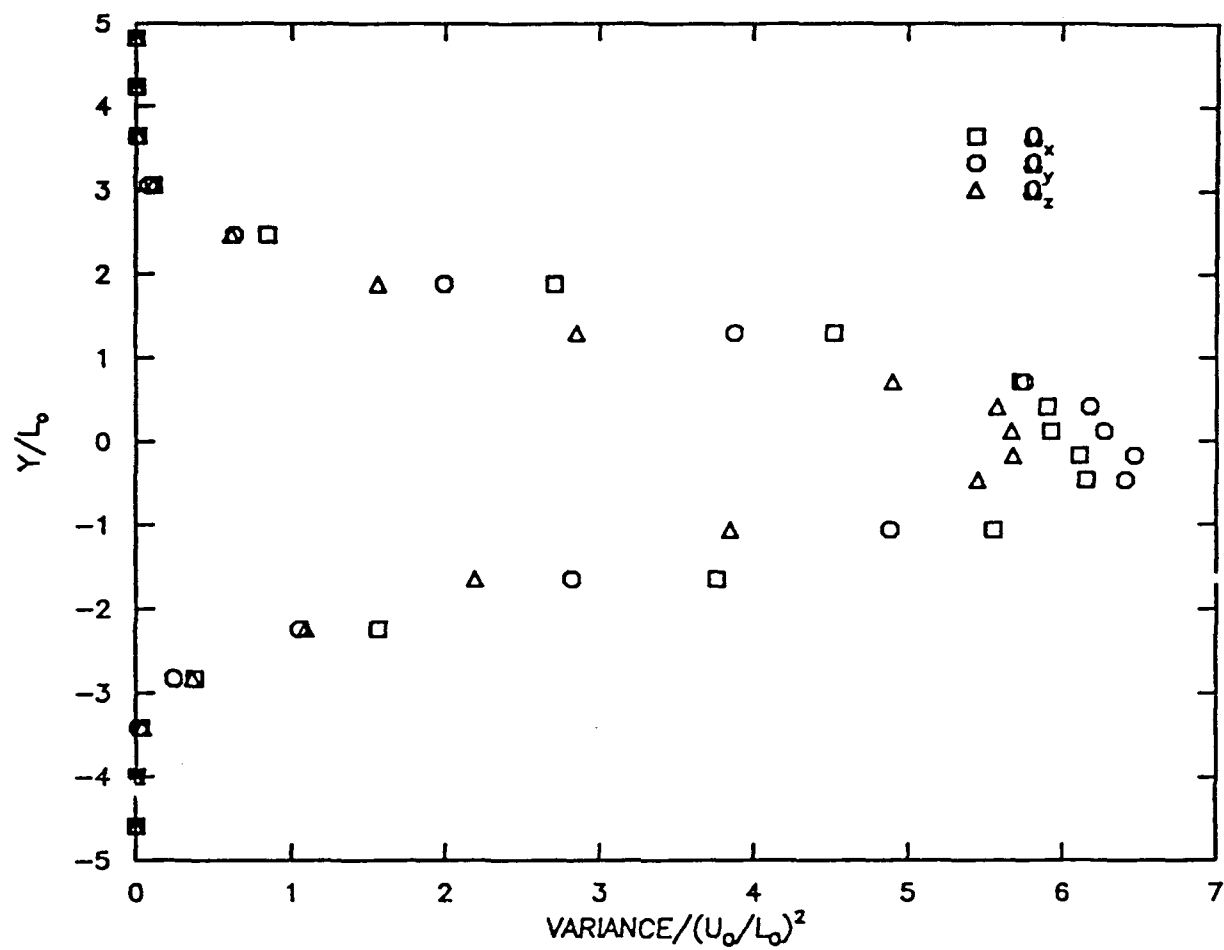


FIGURE 18. Variance of vorticity fluctuations measured by the vorticity probe in the circular cylinder wake.

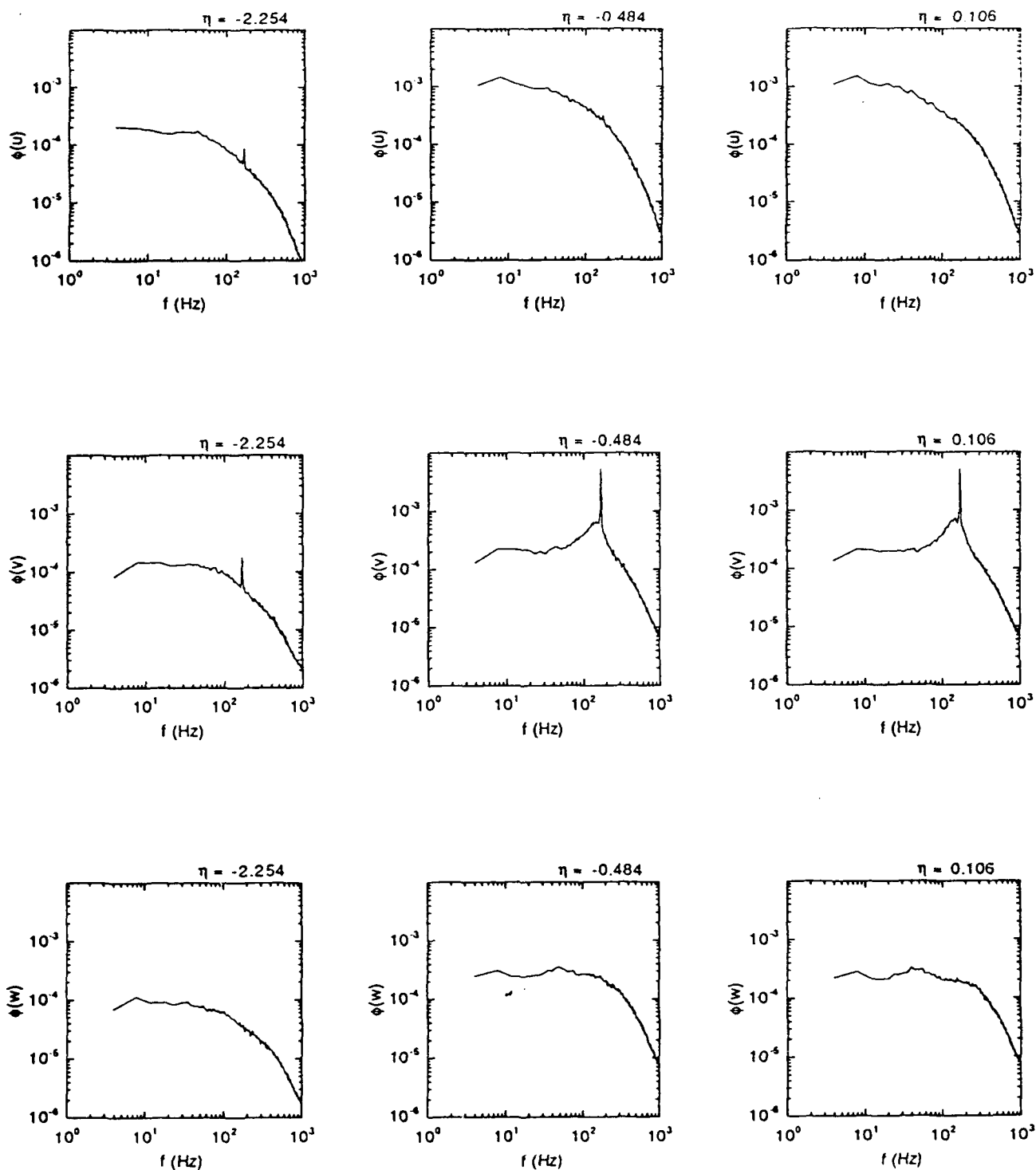


FIGURE 19. Velocity power spectra measured by the vorticity probe in the circular cylinder wake at various cross-stream locations ( $\eta = y/L_0$ ).

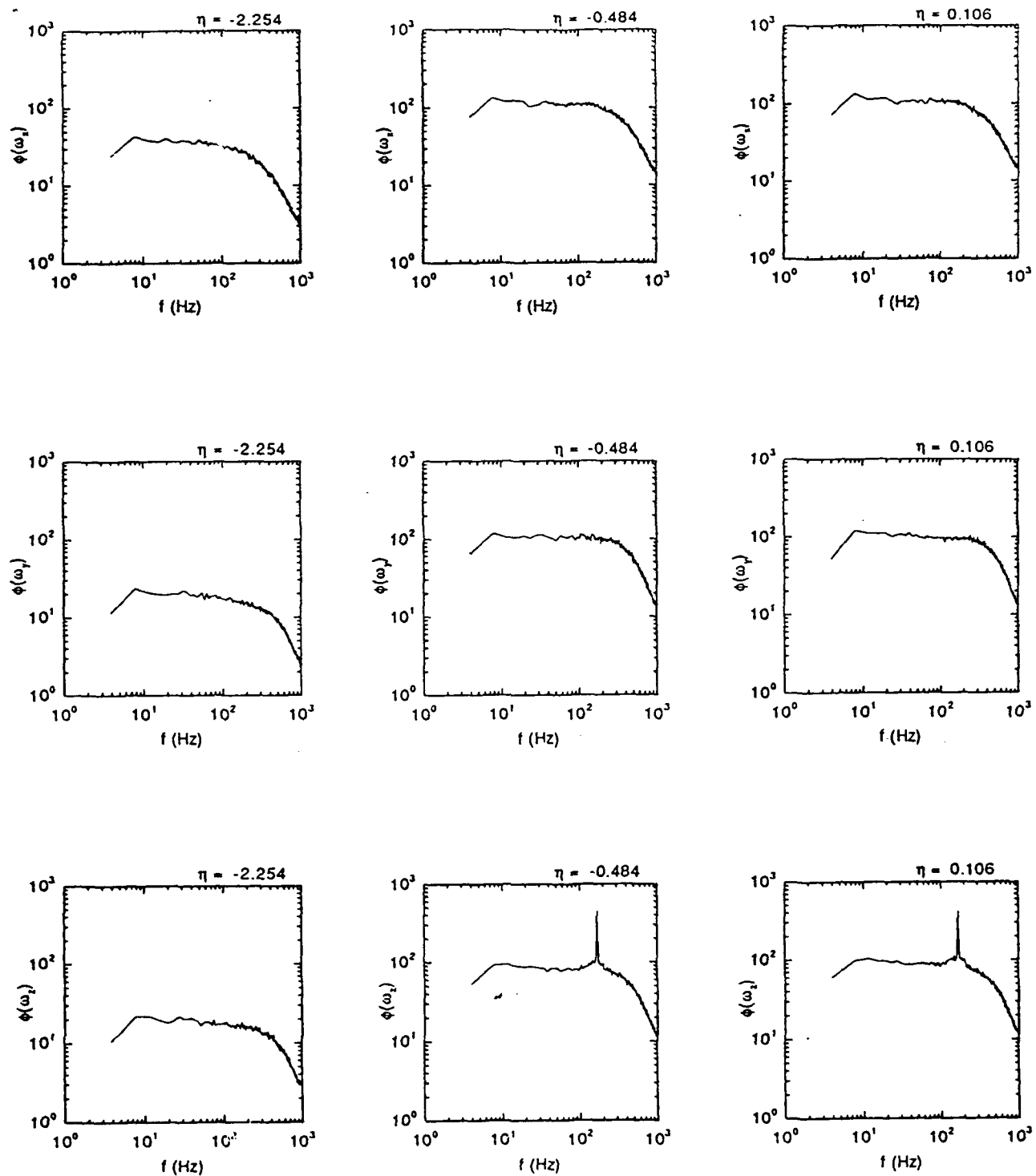


FIGURE 20. Vorticity power spectra measured by the vorticity probe in the circular cylinder wake at various cross-stream locations ( $\eta = y/L_0$ ).

RI-B-90-15

**Experimental Determination of Multiple Nonlinear Kinematic  
Hardening Rules for Cyclic Viscoplasticity Models**

Professor John Moosbrugger  
Department of Mechanical and Industrial Engineering  
Clarkson University

## REPORT SUMMARY

This report documents the results of a one year project funded by Air Force Engineering Foundation Research Initiation Grant RI-B-90-15. A general framework for small strain, isothermal, cyclic viscoplasticity of metals and alloys is presented. The framework employs multiple nonlinear kinematic hardening rules. An approach for partitioning isotropic hardening effects between the so-called "yield stress" and "drag stress" in the viscoplastic flow rule and the saturation level of the kinematic hardening subvariables is presented. A bounding surface interpretation, which is useful for interpretation of experimental results is also given. Materials and biaxial, tension-torsion experiments on thin walled tubular specimens are described and then used to illustrate a technique for estimating overstress from uninterrupted cyclic tests. The results of these estimations are interpreted in the context of the general framework. The technique is applied to data obtained for Type 304 stainless steel tested at room temperature and for Waspaloy (fine and coarse grain microstructures) tested at 650°C. Determination of the appropriate number of nonlinear kinematic hardening rules is accomplished by differentiation of backstress histories for proportional cycles computed with the knowledge of the effective overstress at approximately the same effective inelastic strain rate. Special cases of the general nonlinear kinematic hardening rule are considered. The appropriate distribution of isotropic hardening among the saturation levels of the nonlinear kinematic hardening subvariables is considered in light of the presented results. Kinematic hardening rates are compared with experimental results and refinement is made based on this comparison. Isotropic hardening rules and rate sensitivity functions are formulated and the complete model is integrated for representative biaxial, strain-controlled test histories and compared with experimental results for both Waspaloy microstructures.

RI-B-90-16

**Optimization of the Manufacturing Process of a Titanium Aluminide Metal  
Matrix Composite Using a Viscoplastic Constitutive Theory**

Professor James A. Sherwood  
Department of Mechanical Engineering and Physical Sciences  
University of New Hampshire



## V. CONCLUSIONS

It can be concluded from the results of this study that the implementation of the unified state variable constitutive theory into the ADINA finite element program yields important information pertaining to the mechanical behavior of the fiber/matrix system. From the preliminary tensile tests of the constitutive model in ADINA, it was found that the model had the capability of capturing such material response as the stress drop phenomenon which would not be observed in a bilinear elastic-plastic model. A reasonable finite element mesh was selected after extensive comparisons of a variety of models.

As a result of the research, insight has been gained as to the magnitude of the residual stress field located at the fiber/matrix interface. Various cooling profiles were investigated and shown to have a limited effect on the reduction of the residual stress field. Stress reductions achieved through temperature and pressure holds of various times were also seen to change the residual stress field very little. Stress ratchetting was observed in thermally cycled composites. By applying a constant radial pressure to the composite and thermally cycling the system between 300°C and 600°C, a reduction in the residual stress field magnitude was achieved. This thermal- and pressure-loading combination shows the most promise for the development of composites with residual stress fields below the magnitudes at which fiber/matrix interface damage is initiated.

RI-B-90-17

**Stress Corrosion Cracking of a Superplastic Aluminum-Lithium Alloy**

Professor M. N. Srinivasan  
Department of Mechanical Engineering  
Texas A&M University

## ABSTRACT

An investigation was conducted to study the stress corrosion cracking susceptibility of superplastically deformed Werdalite 049, which was available in a thermomechanically processed form, suitable for superplastic forming. Tensile test specimens machined from sheets of 0.090 inch thickness were initially superplastically deformed to different strain levels at a constant true strain rate of  $2 \times 10^{-4}/s$  and a temperature of about 500 C using an INSTRON superplastic testing facility, available in the Department of Mechanical Engineering of Texas A&M University. Most specimens were deformed under a hydrostatic (back) pressure of 400 psi, but some selected specimens were deformed without back pressure. After superplastic deformation, most specimens were aged by solutionizing at 504 C for 1 hr, followed by precipitation hardening for 24 hr at 180 C, but again some selected specimens were not aged.

Stress corrosion testing was then conducted on the superplastically deformed specimens at an (initial) slow strain rate of  $2 \times 10^{-6}/s$ , using a CORTEST Slow Strain Rate Testing Machine. A test cell specially designed and fabricated by the investigator was used for this purpose. The tests were conducted using 3.5% NaCl solution in deionized water as the electrolyte. The test potential was mostly -800 mV, but in selected cases the tests were conducted at other potentials. For comparative purposes, tests were also made on as-received samples, both in the electrolyte and in air.

The results indicate that for the aged samples superplastically tested under back pressure, the elongation at -800 mV is more sensitive to superplastic strain than the tensile strength, though both the values show a decreasing trend with increase in the superplastic strain. The application of back pressure during superplastic testing helps to improve the stress corrosion resistance, presumably by resisting the growth of cavities and the activation of potential cavity nuclei. Aging improves the inherent strength of the material and is therefore desirable for improving the resistance to stress corrosion susceptibility in relation to not aged samples. The aged samples show increased susceptibility for stress corrosion cracking as the applied potential is moved towards the pitting potential. Under pitting conditions, these specimens are completely corroded.

RI-B-90-18

**Effect of Fiber-Matrix Interface Conditions on the Effective  
Properties of Fiber Reinforced Composites**

Professor Gregory Gillette  
Department of Civil Engineering  
The Catholic University of America

## ABSTRACT

A technique is presented, which renders computational the bounds on the effective properties of two-dimensional composites developed by previous researchers. Statistical integrals appearing in these bounds contain three-point correlation functions on material properties in the plane transverse to the fiber axis. The correlation functions can be systematically reexpressed in terms of the substructure geometry, for fiber reinforced composites: matrix properties, fiber size and relative positioning, and fiber properties. The method presented here is innovative in that it allows for non-uniform material properties within the fibers themselves. The motivation for this is to predict properties of composites when there is an arbitrary transition into the surrounding matrix, such as a coating, a surface roughness which creates a smooth transition region, or an incipient separation of the fiber-matrix interface. The usual model case of uniform fibers is treated first, and then the more general case of non-uniform fibers.

RI-B-90-19

**Novel Microstrip Antenna Configurations for Enhanced Performance**

Professor James T. Aberle  
Department of Electrical Engineering  
Arizona State University

## 5.0 CONCLUSIONS

During this project, a number of conformal antenna geometries have been studied as a means of overcoming some of the disadvantages of conventional microstrip patch antennas such as narrow bandwidth, restricted scan volume, and large echo area at discrete frequencies without comprising attractive features such as low cost and light weight. Using the Green's function/Galerkin technique, numerical models for single radiating elements comprising circular patches backed by rectangular cavities and circular patches surrounded by conducting super-planes and for infinite arrays of circular patches with each patch backed by a rectangular cavity have been developed. Results from these numerical models have been compared to well-validated results for equivalent conventional circular patch cases. The new geometries exhibit impedance characteristics and radiation patterns within the operating band that do not differ greatly from those of conventional circular patches. However, scattering characteristics for the new geometries differ significantly outside of the operating band from those of conventional circular patches. They possess an extra degree of freedom which allows minimization of the RCS at discrete frequencies outside of the operating band, which may be useful in certain applications. Perhaps the most important result of this research has been the confirmation of the fact that the scan performance of conformal patch arrays can be dramatically improved by breaking the substrate into discrete cavities. Indeed, cavity-backed patch arrays do not suffer from the scan-bandwidth tradeoff inherent to conventional patch arrays. In summary, it seems that Geometry 2 is useful for situations where it is desirable to minimize scattering at certain frequencies outside the operating band of the antenna. It is better for this situation than Geometry 1 because the additional super-plane conductor should add very little weight to the antenna whereas a cavity-backing would probably add substantial weight. For arrays, the dramatic improvement in scan performance probably overcomes the drawback of the additional weight of Geometry 1. It is interesting to note that other workers are also beginning to consider cavity-backed patch geometries [2]. In [2], another advantage of the cavity-backed geometry is mentioned: improved heat dissipation which is important when active devices are used. The cavity-backing described in [2] is circular, and in the future, we intend to extend our solution to circular cavity backings because these may be easier to machine.

Evaluation of the RCS of these various geometries requires substantial CPU time. We are currently looking into various interpolation techniques which would allow the RCS to be accurately interpolated at very fine frequency increments from the exact calculation which is performed only over a very few frequencies. One promising technique seems to be model-based parameter estimation [3].

We are also attempting to accelerate the convergence of the series expressions for the matrix element  $z_{N+1,N+1}$  for Geometry 1 using similar techniques as are used for Geometry 2 in Section 2.3. However, results to date have not been promising.

Experimental work on tunable conformal antennas to date shows some promise, and work is continuing in this area. Perhaps the most desirable achievement would be the development of an analytical model for a slot backed by a cavity that is partially filled with ferrite.



## REFERENCES

- [1] M. Abramowitz, I.A. Stegun, eds., *Handbook of Mathematical Functions*, Dover, 1972.
- [2] J.A. Navarro, "A 29.3-GHz cavity-enclosed aperture-coupled circular-patch antenna for microwave circuit integration," *IEEE Microwave and Guided Wave Letters*, vol. 1, no. 7, pp. 170-171, July 1991.
- [3] G.J. Burke, E.K. Miller, S. Chakrabati and K. Demarest, "Using model-based parameter estimation to increase the efficiency of computing electromagnetic transfer functions," *IEEE Transactions on Magnetics*, vol. 25, no. 4, pp. 2807-2809, July 1989.

RI-B-90-20

**Simulation of Amorphous Silicon Hydride Devices**

Professor Finley R. Shapiro  
Department of Electrical and Computer Engineering  
Drexel University

## SUMMARY AND DISCUSSION

Simulations have been presented of TOF experiments across abrupt and graded amorphous semiconductor heterojunctions. The features of transients can be associated with processes which take place in the device during simulated experiments. If the transients were more complicated, their features could be analyzed by varying internal variables of the simulator.

The simulations suggest that TOF experiments can make an important contribution to understanding of amorphous semiconductor heterojunctions. Experiments with abrupt junctions and with various graded junctions could show if an abrupt heterojunction is really equivalent to a graded junction of zero or near zero width. If not, the difference would be due to the effect of surface states at the heterojunction.

These experiments may also provide a direct measure of the band energy change at the junction.

By studying capture and emission rates as shown in TOF transients with different device thicknesses, it should also be possible to find more reliable values of the capture coefficients of the states at different energies. In addition, experiments such as these may give information on how shallow tail states contribute to transport in the region where the mobility edge is shifting to higher energy. This may reveal important insights to the applicability of the band conduction model to room temperature conduction in amorphous materials.

Once the experiments are performed, it will be possible to simulate them using the same experimental parameters. It will then be possible to make direct comparisons between the experimental and the simulation parameters.

RI-B-90-21

**Continuous-Time Adaptive Signal Processing Techniques**

Professor Frank Cornett  
Department of Electrical Engineering  
Tennessee Technological University

### Project Description

This project addresses the need for a well-developed theory in the area of continuous-time, or analog, adaptive signal processing. To date, the adaptive processing of signals has been conducted almost entirely with discrete-time, or digital, implementations. Although the digital implementation is effective for a broad class of signals, it has two drawbacks. Firstly, many signals exist which have bandwidths beyond the capabilities of digital hardware. Although the speed of digital circuitry is increasing rapidly, the bandwidths of signals in telecommunications, radar, etc., can always be expected to expand just as rapidly, thus remaining out of the reach of digital adaptive filters. For the same reasons, analog circuitry will always have bandwidth capabilities beyond those of digital electronics, making analog implementations attractive for wideband adaptive filters. Secondly, for a given application, analog circuitry is much more efficient than digital circuitry in terms of complexity, size, weight, and power. Thus, if performance is equivalent for the two implementations, the analog implementation is usually preferable. Demonstration of this equivalence of performance is one of the goals of this project, and success in this respect has been achieved.

Specific objectives for the project are as follows:

- 1) Comparison of discrete-time (DT) and continuous-time (CT) adaptive filters. The first step in this task is the development of algorithms for the adaptation of the CT filter. Following this development is the comparison of performance in terms of mean-square error and convergence time. These steps are to be conducted for both the common transversal structure and the more complex lattice structure.

2) Investigation of recursive adaptation schemes. Both the transversal and lattice structures referred to above are all-zero filters, and consequently are unconditionally stable (although the adaptation process can be unstable). In many cases, the tradeoff for this unconditional stability is increased complexity for a given performance level in comparison to the performance offered by recursive filters which have both poles and zeros. Consequently, this task has the goal of developing algorithms for adaptive recursive filters.

3) Unification of the theory. Where possible, the analyses conducted in this project are applied to both DT and CT implementations, with numerous comparisons of the two approaches drawn along the way. The result of this unification is a body of information which can be exploited by the engineer to address the problem of adaptive filtering without being forced into a digital or an analog implementation at the outset.

#### Activity

Funding from the Engineering Foundation for this project provides partial support for the principal investigator (PI), Dr. Frank Cornett, at an intended level of 25% during the academic year and 100% for two months of the summer of 1991. The actual level of effort for the PI was closer to 40% during the academic year, made possible by the release of the PI from the teaching of one course during both the fall and spring semesters. This release has been accomplished with matching funds provided by the Center for Manufacturing Research and Technology Utilization at Tennessee Technological University. The PI utilized this time for both conducting his own research and for advising two students who conducted research leading to the masters degree. The efforts of all three of these individuals are directly applicable to the goals of this project.

One student is Mr. David Reynolds, who, having completed his course work, devoted 100% of his time since the inception of this grant to research for the completion of his degree requirements. Mr. Reynolds completed the writing of his thesis, fulfilled degree requirements in March, and graduated officially in May of 1991. Although his research applies to this project, Mr. Reynolds was not supported under this grant.

The second student under the advisement of the PI is Mr. Arunkumar Rajasekaran, who began his masters program in the fall of 1990. Mr. Rajasekaran has completed most of his course work, and is conducting research in the area of recursive adaptive filters. During the summer of 1991, he worked full time at his research. He is supported by funds from the Manufacturing Center under the terms of this grant.

### Progress

In order to facilitate the discussions to follow, a block diagram illustrating the so-called direct form structure of the continuous-time adaptive transversal filter is provided in Figure 1. The filter consists of a sequence of analog blocks, each with transfer function  $H(s)$ , feedforward coefficients  $a_i$ ,  $i=0,1,\dots,M$ , and feedback coefficients  $b_j$ ,  $j=1,2,\dots,N$ . For purposes of illustration,  $M = N = 3$  in Figure 1, although these parameters are unrestricted in practice. The process which adapts the  $a$  and  $b$  coefficients in order to meet the filter performance criterion is not shown explicitly. Those familiar with DT adaptive filters will note that the structure in Figure 1 is identical to that for the DT implementation, except that in the DT structure,  $H(s)$  is replaced by  $H(z) = z^{-1}$ , the unit delay operator. This similarity in structure leads to a number of commonalities in performance between the CT

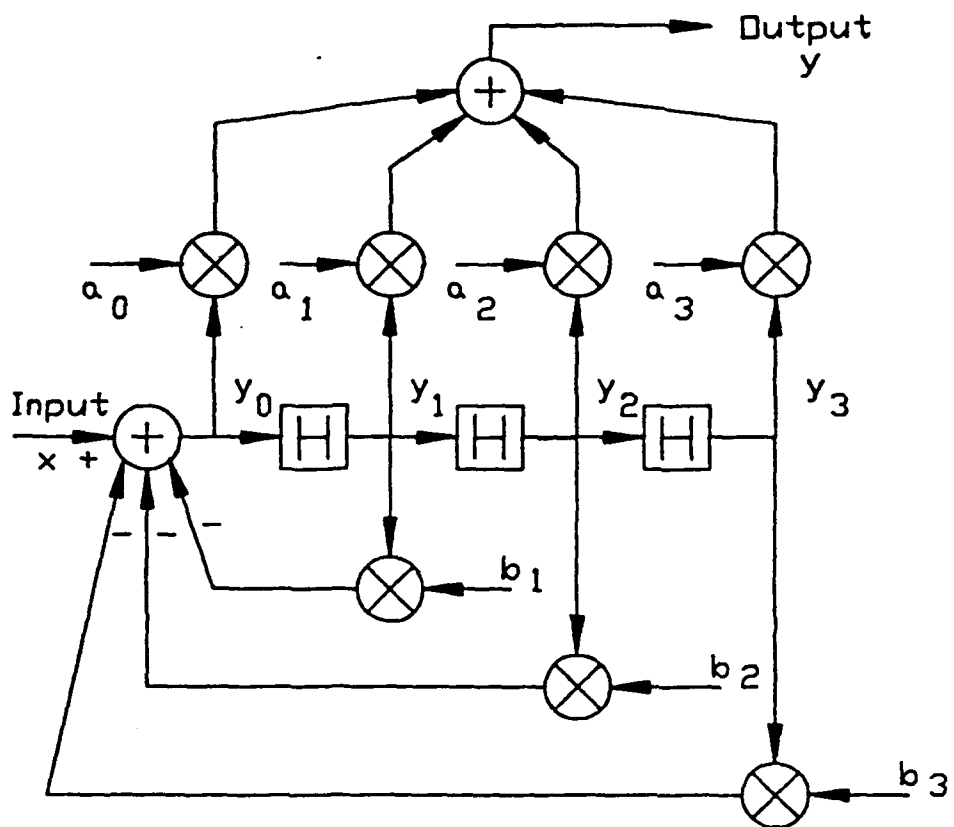


**FIGURE 1**  
DIRECT-FORM STRUCTURE



and DT adaptive filters. An equivalent similarity and set of commonalities exists between the CT and DT lattice structures[Ref. 1].

Progress to date can be stated in terms of the three objectives delineated above:

1) Comparison of discrete-time and continuous-time adaptive filters. All of the work conducted within this task has been confined to transversal filters, that is, filters for which the feedback coefficients  $b_i$  in Figure 1 are all zero, and to lattice filters with only feedforward signal propagation. Investigation of recursive filters, that is, filters with feedback, was carried out as a separate task, described below.

Analyses were conducted in the context of interference reduction or signal equalization, both of which are common signal processing operations in the field of telecommunications. In these contexts, the input signal  $x(t)$  shown in Figure 1 consists of a desired signal (possibly distorted by an unknown filter) plus noise and/or interference. The role of the adaptive filter is to minimize the power (mean-square) in the error signal  $e(t) = y(t) - d(t)$ , where  $d(t)$  is the desired signal, undistorted and noise free, and  $y(t)$  is the filter output.

For the direct form adaptive structure, the following progress has been made: an adaptation algorithm has been derived which continuously updates the feedforward coefficients  $a_i$  so as to minimize the mean-square error (MSE). Two critical performance characteristics in the adaptation process are the time required for the filter coefficients to converge to their proper values, and the value of the minimum MSE (MMSE) which can be achieved after convergence is complete. Analysis of both characteristics has been completed, showing that the performance of the CT adaptive filter is essentially identical

to that of the DT filter. This result is critical, indicating that the design engineer need not give up performance in order to obtain the bandwidth and complexity advantages of the analog implementation.

Sensitivity of the MMSE to errors in the bandwidth of the basic analog block  $H(s)$  has been determined. The effects of such errors, which are inherent in an analog system, are substantially mitigated by the adaptation process itself in an adaptive structure. The adaptation simply causes the filter coefficients to be modified in such a way as to accommodate the bandwidth errors, in addition to minimizing the MSE. Consequently, if the parameters of  $H(s)$  are controlled to reasonable tolerances, as would be expected, inaccuracies do not result in significant system performance degradation.

For the CT lattice structure, both a normalized and an unnormalized adaptation algorithm have been derived. Convergence and MMSE characteristics have been determined, once again indicating that the CT structure yields performance identical to the DT implementation.

For both the direct form and lattice structures, analyses have been completed to determine the effect of the choice for the basic analog block  $H(s)$  used in the adaptive filter. Both one-pole lowpass and one-pole allpass blocks have been considered, and the MMSE has been shown to be identical for both block types. However, adaptive structures made up of lowpass blocks exhibit in many situations a very large spread between the maximum and minimum eigenvalues of the signal autocorrelation matrix, which results in very slow convergence. By comparison, the eigenvalue spread for structures incorporating allpass blocks may be smaller by several orders of magnitude, indicating that the allpass block is

preferable in order to obtain good convergence characteristics. A second reason for preferring the allpass block over the lowpass block is that the  $a_i$  coefficients for the filter made up of allpass blocks have a much smaller minimum-to-maximum range. Since a large dynamic range is difficult to achieve in analog multipliers, this result is very important in terms of a practical implementation.

In addition to allpass and lowpass characteristics, the analog block  $H(s)$  can be chosen to be an integrator, for which  $H(s) = 1/s$ , or a differentiator, for which  $H(s) = s$ . These two choices lead to a simplification in the analysis of the adaptive structure, and also result in no interaction of the adaptive filter coefficients, as occurs with either an allpass or lowpass basic analog block. There are numerous practical difficulties associated with integrators and differentiators, in particular, differentiators exhibit problems with high-frequency noise, and integrators are plagued by nonzero offset voltages. Despite these difficulties, it was felt that the potential for simplification warranted an investigation of their use. In the investigation conducted, which was for a particular application of equalization, much the same set of problems was encountered as for the lowpass analog block, leading to the conclusion that, among the four types of basic analog block types considered, the allpass structure provides the best performance. It is also practical to implement, consisting of a simple RC network and an active amplifier with a gain of 2.

This preference for the allpass block carries over to the lattice structure as well. An important benefit of the lattice filter is the orthogonalization of the backward error residual signals. This feature occurs naturally in the DT lattice filter, but is obtained in the CT filter only if the analog blocks are allpass.

Numerous computer simulations have been completed for both analog and digital implementations of both direct form and lattice structures. These simulations corroborate the theoretical analysis very well, and bear out the performance equivalence between digital and analog adaptive filters.

During the summer of 1991, the results achieved within this task were incorporated into two papers which are planned for submission for publication in the Transactions on Circuits and Systems of the IEEE. The first paper delineates results related to the direct form structure, whereas the second provides results for the lattice structure.

2) Investigation of recursive adaptation schemes. It is well known that in most filtering applications, recursive filters, with both poles and zeros, provide better performance than nonrecursive, or all-zero filters for a given filter complexity, where complexity can be measured as the total number of feedforward and feedback coefficients. However, a number of problems arise with recursive adaptive filters. First is the problem of filter stability. Although the adaptation process for nonrecursive filters can be unstable, instability is seldom a problem since it can be avoided with small adaptation gain. Instability of the filter itself is impossible. With recursive filters, there is a potential for instability in both the adaptation process and the filter. Secondly, the error surface for the recursive filter exhibits local minima, so that convergence of the filter coefficients to attain the global minimum of the MSE is in general not assured. Thirdly, the adaptation process for recursive filters is more complicated, for a given complexity, than for nonrecursive filters.

In the late 1970's, several papers[2,3,4,5] appeared describing the so-called hyperstable adaptive recursive filter (HARF). This technique was developed in the context

of identifying the pole-zero coefficients of an unknown discrete-time plant. However, by recasting the problem, HARF can be applied in equalization or interference reduction applications. The HARF algorithm solves the first two problems described above, making it an attractive alternative to the nonrecursive adaptive scheme. A significant reduction in complexity was proposed[4,5] as the simplified HARF, or SHARF. The cost of this reduced complexity is that the SHARF cannot be shown to be stable.

In addition to the above mentioned shortcomings of HARF and SHARF, both algorithms share a second serious drawback. If the unknown plant has transfer function  $B(z)/A(z)$ , then a smoothing filter  $C(z)$  must be employed in the HARF adaptation process, where the transfer function  $C(z)/A(z)$  has phase between  $-90^\circ$  and  $90^\circ$  for all values of  $z$  on the unit circle. Thus, the proper choice for  $C(z)$  requires some knowledge of  $A(z)$ , which is often unavailable.

As part of this project, a CT HARF algorithm has been developed. This algorithm shows great promise, since it naturally has the reduced complexity of the DT SHARF technique. More importantly, stability is not sacrificed with the CT HARF filter; a proof demonstrating convergence has been developed. A limited number of simulations have been conducted.

Unfortunately, the CT HARF shares with the DT algorithms the drawback of requiring a smoothing filter  $C(s)$  for which the phase of  $C(s)/A(s)$  must lie between  $-90^\circ$  and  $90^\circ$  for all  $s$  on the  $j\omega$  axis. Consequently, modified HARF algorithms have been developed, for both CT and DT applications, which obviate the need for knowledge of  $A(z)$  or  $A(s)$ . Both adaptation algorithms have been shown to be stable, meaning that the error between

the desired signal and the adaptive filter output approaches zero as time progresses. However, because the filter output is not computed in a truly recursive manner in the modified algorithms, it is not for certain that the filter which results from the adaptation is stable. Thus, further analysis and simulation will be conducted to evaluate these algorithms.

Another approach, derived from the CHARF[6] algorithm, has been investigated to a small extent. It appears that with this approach the smoothing filter  $C(s)$  can either be obtained adaptively or eliminated altogether. Further analyses and simulations are planned to determine the effectiveness of this algorithm.

If these efforts toward an effective continuous-time recursive adaptive filter prove successful, it is felt that the resultant algorithms will constitute a significant contribution to the field of adaptive filtering.

3) Unification of the theory. As can be seen from the above discussions, every effort has been made in this project to carry forward the treatment of both analog and digital implementations of adaptive filters in parallel. The result of such a treatment is a body of knowledge relating to the actual problem of adaptive filtering, without predisposition toward the form of implementation.

#### References

- [1] Cornett, F., and D. K. Reynolds, "Continuous-Time Adaptive Signal Processing," Proc. IEEE Southeastcon '90, April, 1990.
- [2] Larimore, M. G., "Hyperstability and Adaptive Filtering," Proc. 13th Asilomar Conf. Circ., Sys. and Computers, pp. 412-15, Nov. 1979.
- [3] Johnson, C. R., Jr., "A Convergence Proof for a Hyperstable Adaptive Recursive Filter," IEEE Trans. Info. Thry., vol. IT-25, pp. 745-49, Nov. 1979.

- [4] Larimore, M. G., J. R. Treichler, and C. R. Johnson, Jr., "SHARF: An Algorithm for Adapting IIR Digital Filters," IEEE Trans. Acoust., Speech, Sig. Proc., pp. 428-40, August, 1980.
- [5] Johnson, C. R., Jr., M. G. Larimore, J. R. Treichler, and B. D. O. Anderson, "SHARF Convergence Properties," IEEE Trans. Acoust., Speech, Sig. Proc., pp. 659-70, June, 1981.
- [6] Johnson, C. R., Jr., and T. Taylor, "CHARF Convergence Studies," Thirteenth Asilomar Conf. Circ., Sys., and Comp., 1979, pp. 403-407.

RI-B-90-22

**A Distributed Algorithm for Fault Simulation of Digital  
Designs Based on Circuit Partitioning**

Professor Sumit Ghosh  
Division of Engineering  
Brown University



## NODIFS: A Novel, Distributed Circuit-Partitioning Based Algorithm for Fault Simulation of Combinational and Sequential Digital Designs on Loosely-Coupled Parallel Processors

Sumit Ghosh  
LEMS, Division of Engineering  
Brown University, Providence, RI 02912.  
sg@lems.brown.edu

### Abstract

Fault simulation constitutes an indispensable tool in ensuring the correctness and quality of manufactured digital designs. Traditional uniprocessor based algorithms for fault simulation have been observed to be agonizingly slow for today's large and complex digital designs. More recently, the literature presents an approach, introduced by a few researchers, wherein the fault set was partitioned and the digital design fault simulated for each of the fault subset on separate processors of a parallel processor system. This approach is limited in that it continues to utilize the traditional uniprocessor-based algorithm and the results indicate that the performance results are not encouraging. This paper introduces, perhaps for the first time, a novel, distributed, circuit-partitioning based algorithm for fault simulation of both combinational and sequential digital designs. In this approach, referred to as NODIFS in this paper, every component in the circuit is modeled as an asynchronous, concurrent, entity that is fault simulated as soon as appropriate signal transitions and fault lists are asserted at its input ports. The circuit is partitioned such that components of every partition are allocated to a unique processor of the parallel processor system. Consequently, a number of components may be concurrently fault simulated on multiple processors in NODIFS implying significant increase in throughput. The advantages of this approach are - (i) potentially very high throughput in contrast to the traditional approach, (ii) the algorithm is novel in that the overall task of decision-making i.e., fault simulation of the circuit, is distributed into a number of natural, independent, and concurrent entities that execute asynchronously to utilize maximal parallelism, and (iii) the algorithm is scalable. The notion of performance scalability implies that where the problem size i.e., the size of the circuit being fault simulated, is doubled, and the number of processors of the parallel processor system is simultaneously increased by a factor of 2, the increase in the required CPU time is not appreciable. Equivalently, the level of performance is held at a uniform value of less than 2.0. For a given circuit size,  $S$ , number of processors,  $P$ , and speedup factor  $f_1$ , the performance level is defined in this paper as the ratio of the speedup factor  $f_2$  to  $f_1$ , where  $f_2$  corresponds to the circuit size and number of processors doubled to  $2 \times S$  and  $2 \times P$  respectively. The speedup factor is defined as the ratio of the CPU times required for fault simulation in the uniprocessor to that for the distributed approach. Given that the ratio of the problem size to the number of computational engines may be effectively maintained at a uniform value for any arbitrary yet pragmatic problem size, the possibility of continued increase in the overall performance of the fault simulation algorithm, as opposed to a uniprocessor, is implied. Additionally, the NODIFS algorithm is a natural choice for fault simulation of behavior-level circuits - an eventual reality, wherein the ratio of the computational to communication load for the behavior models may approach a significantly large value. This paper also reports on an implementation of NODIFS on both the ARMSTRONG parallel processor system at Brown University and the performance results indicate significant increase in the speedup for a few representative example digital designs.

RI-B-90-22  
Report on final phase



## BROWN UNIVERSITY

Division of Engineering, Box D, Providence, Rhode Island 02912, U.S.A.

Telephone 401-863-1430, Fax 401-863-1157, Email: sg@lems.brown.edu

---

Prof. Sumit Ghosh

July 8, 1992

Dr. Charles Fröman  
Engineering Foundation  
Suite 303  
345 East 47<sup>th</sup> Street  
New York, NY 10017

Dear Dr. Fröman,

Please find enclosed a report that details the results of the second and last phase of the research conducted under the grant EF-RI-B-90-22. Thus, I have completed the goals as stated in my letter to you dated October 1, 1992. I am very grateful to the Engineering Foundation for permitting me the no-cost extension to the original research proposal for 1991-1992. I believe that this second phase of the research will be extremely valuable to the industry since most businesses lack specialized parallel processors but possess large numbers of workstations. I am already in the process of using the contents of the enclosed draft to prepare a journal quality paper for possible publication in the IEEE Computer. I hope to finish writing the paper by August 1992 and will be delighted to acknowledge the support of this grant. I will also mail you a copy of the final paper at that time. I will continue to pursue the spirit of this research, i.e. fault simulate even larger circuits. The first paper from this grant is still under review by the International Journal of Electronic Testing (JETTA) and a conference version of the paper has been published in the proceedings of the IEEE Systems, Man, and Cybernetics Conference, October 1991.

Thank you very much,

Sincerely,

*Sumit Ghosh*

# Software Engineering Techniques for Modeling Complex Asynchronous, Distributed, Algorithms on a Network of Sun Workstations Configured as a Loosely-Coupled Parallel Processor System

Kenneth S. Lyons

Sumit Ghosh

sg@lems.brown.edu

Division of Engineering  
Brown University, Providence  
Rhode Island 02912

The ARMSTRONG system is known as a loosely-coupled parallel processor, each node having its own memory (local memory) and a means of communication with other nodes. In the ARMSTRONG case, each node is physically connected to up to eight other nodes, but can communicate to any node through message routing. The physical connections between the ARMSTRONG nodes are designed as patchcords that can be configured by hand to the desired network topology. This is a great asset in optimizing the network. It is easy to see the similarities between the ARMSTRONG parallel processor and a network of computers—in our case a network of Sun workstations. Each workstation has its own memory and can communicate with any other workstation. One extremely big advantage is the fact that each Sun workstation is far more powerful than an ARMSTRONG node. It is difficult to say exactly how much more powerful, but it should be noted that the Suns are running a 68030 or 68040 at xxMHz with true coprocessor interface, while an A

In practice only small simulations could be run on the ARMSTRONG, as the nodes quickly ran out of memory. At this point it became necessary to lay down the foundations for using Sun workstations as a loosely-coupled network of parallel processors. The project began with modifying existing ARMSTRONG simulations so they could be run on the Suns. This was fairly easy as the inter-process communications on the ARMSTRONG system strongly resemble internet sockets.

The code was written as separate functions that emulate ARMSTRONG built-in functions. We began with the ARMSTRONG `ns_bind` call, syntax: `ns_bind(process_name)`. This is called by all processes to assign a symbolic name to themselves. The nodes cannot receive specific communications without first assigning themselves a name, but they can receive datagrams. To emulate this function on the Suns, it is necessary to save the pertinent information about the calling process in a file. The file is called "boundnames" and consists of a line for each process that has called `ns_bind`. On this line is the name of the calling process (the argument of the `ns_bind` call), followed by the name of the Sun workstation it is running on, followed by the internet address of the workstation, followed by a unique 32 bit number that identifies the workstation's CPU, followed by the local process number of the calling process. Not all of this information is necessary for full compatibility, but is provided for future flexibility

```
/* Function ns_bind(process_name) */
/* assigns symbolic name process_name to calling process */
/* called by: anyone */
```

```

/* calls      : establish_connection() to create a socket to listen on      */
/*            (various system calls)                                       */
/* files      : boundnames                                                 */

int ns_bind(char name[MAXNAME])
{
    struct hostent *hp;
    char hostname[MAXNAME];
    int hn,nlen=sizeof(hostname);
    char hostaddress[20];
    long hostid;
    int process;
    FILE *fp;

    if ((hn=gethostname(hostname,nlen)) <0) { /* get name of workstation */
perror("Couldn't find host name!");
        return(hn);
    }

    hp=gethostbyname(hostname); /* get internet address */
    if (hp==NULL) {
        return(-1);
    }

    hostid=gethostid(); /* get unique 32 bit CPU number */
    process=getpid(); /* get local process number */
    bcopy (hp->h_addr,hostaddress,hp->h_length);

    while ((fp=fopen("boundnames","a")) ==NULL);
    /*keep trying file in case someone else is accessing it at the time */

    fprintf(fp,"%s %s %s %u %u\n",name,hostname,inet_ntoa(hostaddress),hostid,process);
    fclose(fp);

    establish_connection(); /* create a socket to listen on */
    return(0);
}

```

Note that this function makes a call to establish\_connection, which has no counterpart on the ARMSTRONG system. This function is necessary to create a socket on the Suns, and is designed to return the socket identifier in the global variable globalsocket. It is necessary to use a global variable for this purpose. as the ARMSTRONG ipc\_accept call does not take an argument for the socket to accept on (since the

ARMSTRONG does not need sockets). The code for establish\_connection is as follows:

```
/* Function establish_connection() */
/* creates a socket to listen for connect requests */
/* called by: ns_bind */
/* calls : (various system calls) */

int establish_connection(void)
{
    struct sockaddr_in name;

    /* create a stream socket (reliable communication) of type internet */
    if ((globalsocket=socket(AF_INET,SOCK_STREAM,0))<0) {
        perror("---> Error creating socket");
        exit(1); /* could not open socket, no point to continue execution */
    }

    /* initialize address structure */

    name.sin_family=AF_INET;
    name.sin_addr.s_addr=INADDR_ANY; /* wildcard address */
    name.sin_port=htons(PORT); /* PORT should be defined earlier as an */
                                /* unused port */

    /* bind address to socket */
    if (bind(globalsocket,(struct sockaddr *)&name,sizeof name) <0) {
        perror("---> Error binding socket");
        exit(2); /* could not bind address, no point to continue execution */
    }

    listen(globalsocket,5); /* queue up to five connect requests */
    return(0); /* exit ok */
}
```

Now that we have shown how to bind a name to a process and create a socket to receive connections, we need to add functions to perform the accept, connect, send and receive routines. The ipc\_connect call is fairly straightforward on the ARMSTRONG, taking the name of the process to connect to as its first argument and returning the connection identifier in its second argument. In the socket analogy, the connect call requires the internet address to connect to and returns the connection identifier. The connect request must also be given a socket descriptor to perform the connection on. This is done by creating a new

socket each time the `ipc_connect` function is called. The simplest form of this function would access the "boundnames" file to find the name of the Sun workstation that corresponds to the process name given in the `ipc_connect` call, then make a connection to that workstation. The code to do this is:

```

/* Function ipc_connect(process_name,connection_id)                */
/* connects to process with process_name and returns connection identifier */
/* called by: anyone                                              */
/* calls      : (various system calls)                            */
/* files      : boundnames                                         */

int ipc_connect(char name[MAXNAME],int *cid)
{
    char processname[MAXNAME];
    char hostname[MAXNAME];
    char hostaddress[20];
    char hostid[20];
    char process[10];
    char c;
    struct sockaddr_in sockname;
    struct hostent *hp;
    int i;
    FILE *fp;

    while ((fp=fopen("boundnames","r")) ==NULL) /* keep trying to open file */
        /* in case someone else is using it */

    while (1) {
        fscanf(fp,"%s %s %s %s %s",processname,hostname,hostaddress,hostid,process); /* read
        if (!strcmp(processname,name)) { /* do we have a match? */
            fclose(fp); /* Yes, close file */
            sockname.sin_family=AF_INET; /* initialize address structure */
            sockname.sin_port=htons(PORT);
            hp = gethostbyname(hostname); /* get internet address of host */
            bcopy (hp->h_addr, &(sockname.sin_addr.s_addr), hp->h_length);

            /* create a socket to make this connection on */

            if ((sock=socket(AF_INET,SOCK_STREAM,0))<0) {
                perror("----> Error creating socket");
                exit(1); /* no point in continuing */
            }

```

```

    /* make the connection */

    if (connect(sock,&sockname,sizeof(sockname)) < 0)
        {
            close(sock);
            return(-1); /* no good, had an error */
        }

    *cid=sock;
return(0); /* everything's fine */
}
/* check for end of file */
c=getc(fp); /* should be newline char */
c=getc(fp);
if (c==EOF) {
    fclose(fp);
    return(-1); /* process not found, return with error */
}
ungetc(c,fp); /* not end of file so put back good char */
}
}
}

```

The `ipc_send` and `ipc_rcv` calls are a little more difficult, as they can handle a variable length argument list, terminated by the flag `EOA`. The best way to handle these routines is to write several of them, each one specifically for sending or receiving a certain number of arguments which are of a particular type. Of course this could grow to be quite a nuisance, but to date most of the ARMSTRONG simulations involve only one or two different send and receive calls. In the future when programs are written directly on the Suns this will not be a problem; it is only a problem when converting ARMSTRONG simulations to run on the Suns. The following example is very specific. It shows how the code would be written to send and receive two integers at a time. The ARMSTRONG calls would be:

```
ipc_send(cid,INT(x),INT(y),EOA)
```

Where `cid` is the connection identifier to send on, `INT` is a macro that specifies `x` and `y` as integers, and `EOA` is the 'end-of-list' flag. The receive call would be:

```
ipc_rcv(cid,RINT(x),RINT(y),EOA)
```

With similar parameters except the macro `RINT` which tells the computer that it is receiving an integer. To implement these routines on the Sun, we would need the following two functions designed to handle two and only two integers:

```

#define INT(x) x      /* 'dummy' macros to make functions compatible */
#define RINT(x) &x

```

```

/* Function ipc_send(cid,INT(x),INT(y),EOA)                                */
/* sends two integers on connection cid                                   */

int ipc_send(int protocol_id,int x1,int x2,int dummy)
{
    int a;

    a=send(protocol_id,&x1,sizeof(x1),0);
    if (a<0)
        return(a); /* error */

    a=send(protocol_id,&x2,sizeof(x2),0);
    if (a<0)
return(a); /* error */
        return(0); /* good */
}

/* Function ipc_rcv(cid,RINT(x),RINT(y),EOA)                                */
/* receives two integers from connection cid                                   */

int ipc_rcv(int protocol_id,int *x1,int *x2,int dummy)
{
    int a;

    a=recv(protocol_id,x1,sizeof(int),0);
    if (a<0)
        return(a); /* error */

    a=recv(protocol_id,x2,sizeof(int),0);
    if (a<0)
return(a); /* error */
        return(0); /* good */
}

```

These function have been expanded to include network debugging and are joined by the functions `n_s_unlookup`, `ipc_select`, and `ipc_accept` in the file `Armstrong_to_Sun.c` which can be inserted into any ARM-STRONG simulation to make it run on the Suns (after modifying the `ipc_send` and `ipc_rcv` calls of course). This code is included in Appendix A.

As mentioned earlier, the Sun workstations communicate over ethernet in a ring network through message routing. It is possible that this network could become quite congested by running large simulations, especially



if the network is being shared with other users. The ARMSTRONG computer allows you to physically construct the desired network as a tree, hypercube, or other structure, but the Suns are basically limited to the ring structure. To determine the feasibility of using the Suns for parallel simulation, a benchmark program was written to send packets to all other nodes running the benchmark program. The code for the program and the results of the simulation are found in Appendix B.

#### Appendix A: Armstrong\_to\_Sun.c

```
/* This is a file of simple routines that can be added to any Armstrong
 * program to make it run on the Suns, with little or no modification.
 * Note that the functions are designed to mimic ipc calls on the Armstrong
 * by using sockets on the Suns. All of the code is modular, so it should
 * be easy to upgrade it to STREAMS or other forms of communication.
 * Note that the function establish_connection does not have a counterpart
 * on the Armstrong system. It is necessary to initialize a socket on which
 * to listen for connect requests, and that is accomplished by this function.
 * It needs to be called only once before any ipc_accept calls are made, and
 * is called automatically inside of an ns_bind call or an ipc_accept call
 * if it has not been called already. This allows you to accept connections
 * even if you have not assigned yourself a name; even though this would be a
 * paradox on the Armstrong system, it is possible on the Suns.
 *
 * Most Armstrong calls return a zero if successful, or an error number if
 * unsuccessful. These routines have been designed to do the same, although
 * this limits the power that Sun socket calls usually possess.
 *
 * The ipc_send and ipc_recv routines are very program specific, as on the
 * Armstrong it is possible to send any number of any type of arguments
 * delimited by an EOA, ex:
 *
 * ipc_send(pid,INT(x),STRUCT(y),CHAR(a),STRING(b),DOUBLE(z),EOA);
 * ipc_recv(pid,RINT(x),RSTRUCT(y),RCHAR(a),RSTRING(b),RDOUBLE(z),EOA);
 *
 * The corresponding calls on the Suns do not allow this kind of flexibility,
 * so you may have to write your own routines, one for each different type
 * of send and receive.
 *
 * Example calls:
 *
 * establish_connection() returns a zero if successful
 * ns_bind(pname) assign symbolic name, returns zero if successful
 * ns_lookup(pname,&pid) finds global id for process with symbolic name 'pname'
```

```

*      and returns information in pid (structure gpid), returns zero if
*      successful
* ns_unlookup(&pid,pname) finds name for process with global id contained in
*      pid and returns name in pname, returns zero if successful
* ipc_accept(&cid) accepts a connection, puts descriptor in cid, returns
*      a zero if successful
* ipc_connect(name,&cid) connects to process with symbolic name 'name', puts
*      descriptor in cid, returns a zero if successful
* ipc_select(num_cids,cid_list,&timo,&idx) checks num_cids descriptors
*      in cid_list within time specified by timo for data to be read.
*      returns index into cid_list in idx, and returns a zero if
*      successful
* ipc_send(cid,INT(x),INT(y),EOA) send two integers on cid, returns
*      a zero if successful
* ipc_recv(cid,RINT(x),RINT(y),EOA) receive two integer from cid, returns
*      a zero if successful
*
*
*
*/

```

### Implementation and Performance

The distributed fault simulation algorithm, NODIFS, has been implemented on a network of 22 SUN sparc 1+, sparc 2, and 3/60 workstations, utilizing the techniques outlined in this paper. The nature of performance of NODIFS, i.e. the nature of the graphs for the different representative examples, is observed to be similar to those obtained for Armstrong. The primary strengths of the new approach include the significant ease of debugging and the ability to simulate large: circuits while its only limitation is the slower communication speed arising from the use of ethernet and TCP/IP. As an extension to the original grant, in the past year, we have successfully proved our original hypothesis, namely the use of the network of SUN workstation as a large loosely-coupled parallel processor. We could not, however, fault simulate larger circuits because we ran out of financial resources for student support.

RI-B-90-23

**Parallel Processing for Computer Vision Systems**

Professor Alok N. Choudhary  
Department of Electrical and Computer Engineering  
Syracuse University

## **Parallel Implementation and Evaluation of a Motion Estimation System**

**Prof. Alok N. Choudhary**  
**Department of Electrical and Computer Engineering**  
**121 Link Hall, Syracuse University**  
**Syracuse, NY 13244.**  
email : choudhar@cat.syr.edu  
Phone : (315) 443-4280

### **Abstract**

Computer vision systems employ a sequence of algorithms that exhibit different computational characteristics. These algorithms require different data decomposition and load balancing techniques for efficient parallel implementations. This paper presents several techniques to perform static and dynamic data decomposition for common computer vision algorithms. They exploit the distribution of features as a measure of load for data decomposition. In these techniques, the distribution of features computed during the parallel execution of the current algorithm allows an informed partitioning for the next algorithm in the pipeline, keeping overhead involved in estimating the load small. Performance results obtained from a shared memory multiprocessor implementation using these techniques are presented. Furthermore, a classification of common vision algorithms is given based on their suitability for one or more data decomposition techniques. Improvements of up to 4 times over the performance of uniform block oriented partitioning were obtained.

RI-B-90-24

**Critical Analysis of Partially Open Cylindrical Reflector Antennas**

Professor Atef Elsherbeni  
Department of Electrical Engineering  
University of Mississippi

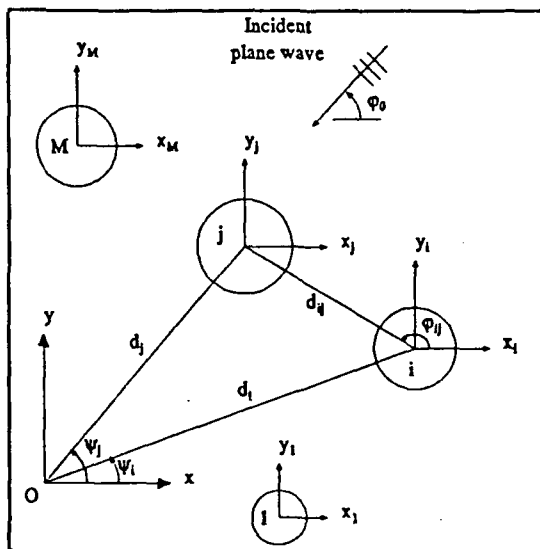
# RADAR CROSS-SECTION OF PARALLEL CIRCULAR CYLINDERS: A COMPARATIVE STUDY OF DIFFERENT TECHNIQUES

Atef Z. Elsherbeni

Electrical Engineering Department  
University of Mississippi  
University, MS 38677

## ABSTRACT

Numerous applications require accurate analysis for predicting the radar cross-section of parallel cylinders. Among these applications is the modelling of reflecting and absorbing surfaces by an array of circular cylinders. The problem of the scattering by many cylinders has been under investigation for decades using different techniques. In this paper, the analysis of selected techniques will be outlined along with numerical comparisons for the far and near fields for an array of circular cylinders. These techniques include an asymptotic high frequency method, a boundary value approach, an iterative scattering method, and a hybrid method combining an eigenfunction expansion method with the method of moments. The parallel cylinders are arbitrarily located as shown in the figure and are made of conducting, dielectric materials or combinations of both. The validity and accuracy of each technique are demonstrated by illustrative examples. The limitations of the associated computer codes when using a personal IBM-PC or compatible computer are also outlined. The effects of various parameters (cylinder to cylinder coupling, angle of incidence of the electromagnetic wave, shadowing effects, spacing between the cylinders and the physical parameters of each cylinder) on the radar cross-section of the array of cylinders are also investigated.



This work was supported by the Air Force-Engineering Foundation Grant number RI-B-90-24.

# ELECTROMAGNETIC SCATTERING FROM AN ECCENTRIC MULTI-LAYERED CIRCULAR CYLINDER

Ahmed A. Kishk, Rajan P. Parrikar, and Atef Z. Elsherbeni

Department of Electrical Engineering

University of Mississippi

University, Mississippi 38677 U.S.A.

## ABSTRACT

The electromagnetic scattering from an eccentric multi-layered, homogeneous, circular cylinder is derived rigorously by using a boundary value mode matching approach. The layers are assumed to be infinite in length and their axes are parallel to each other but their centers may have arbitrary coordinates. The composite arrangement is illuminated by a cylindrical wave from a line source of infinite extent in a direction parallel to the cylinder axis. The problem is two dimensional and the solution to both types of polarization is presented. The effects of various geometrical and electrical parameters on the near and far field patterns are examined.

---

This work was partially supported by the National Science Foundation, Grant No. ECS-8906807, and the Air Force Engineering Foundation, Grant RI-B-90-24.

# SCATTERING OF A GAUSSIAN BEAM BY AN ARRAY OF CIRCULAR CONDUCTING AND DIELECTRIC CYLINDERS

A. Z. Elsherbeni\*, G. Tian\* and M. Hamid\*\*

\*Department of Electrical Engineering  
University of Mississippi  
University, MS 38677

\*\*Department of Electrical Engineering  
University of South Alabama  
Mobile, AL 36688

## ABSTRACT

In this paper, attention is focused on the problem of scattering of a Gaussian beam from an array of parallel circular cylinders. The cylinders are made of homogeneous, isotropic dielectric material, perfectly conducting material, or combination. An iterative scattering technique is developed to evaluate both the near and far field components. The iterative technique starts with exact series representation of the initial scattered fields from each cylinder due to the incident Gaussian beam. Then, the sum of the initial scattered fields from all cylinders is considered to be an incident wave on each individual cylinder. Additional scattered field contribution is then obtained and successive scattering can take place until the boundary conditions on the surface of every cylinder are satisfied. Transverse electric (TE) and transverse magnetic (TM) polarized waves are considered and the effects of the incident beam parameters on the far scattered field pattern are investigated.



RI-B-90-25

**Search-Free Acquisition of Pseudonoise Codes**

Professor Kurt Kosbar  
Department of Electrical Engineering  
University of Missouri-Rolla

## **2. Summary of Research**

### **2.1 Plan of Research**

As described in the original proposal: The research can be divided into the following six tasks:

1. Develop new, closed loop, acquisition architecture
2. Determine performance of new architecture
3. Investigate feasibility of implementing the new architecture
4. Extend theory to the non-coherent case
5. Repeat performance and implementation studies for the non-coherent case
6. Extend analysis to higher order loops

These tasks will be executed sequentially with the amount of effort, risk, and potential benefits increasing with each task. It is reasonable to expect that items 1 through 3 can be accomplished in the first year of research. Tasks 4 and 5 represent another major step in the development and will be initiated, but may not reach fruition in the first year. The extension to higher order loops will be considered, but it is difficult to be optimistic about developing meaningful results in a short period of time. The analysis of other types of second, and higher, order loops has proven to be a formidable challenge.

### **2.2 Project Status:**

Tasks 1 and 3 have been completed, as planned. The new architecture has been developed, and the feasibility of implementation investigated. Substantial progress has also been made on Task 2, and work is continuing in this area, further details are contained in Section 4 of this report. As anticipated in the original proposal, Tasks 4 through 6 were initiated, but have not yielded any significant results to date. Work will also continue on these tasks.